REAL TIME POSE CONTROL OF PARALLEL ROBOT

SAHAR ALINIA

A THESIS

IN

THE DEPARTMENT

OF

MECHANICAL AND INDUSTRIAL ENGINEERING

PRESENTED IN PARTIAL FULFILLMENT OF THE REQUIREMENTS

FOR THE DEGREE OF MASTER OF APPLIED SCIENCE OF MECHANICAL ENGINEERING

CONCORDIA UNIVERSITY

MONTRÉAL, QUÉBEC, CANADA

APRIL 2016

CONCORDIA UNIVERSITY
School of Graduate Studies

This is to certify that the thesis prepared

By: Sahar Alinia

Entitled: Real Time Pose Control of Parallel Robot

and submitted in partial fulfillment of the requirements for the degree of

Master of Applied Science of Mechanical Engineering

complies with the regulations of the University and meets the accepted standards with respect to originality and quality.

Signed by the final examining committee:

Dr. Onur Kuzgunkaya Chair

Professor Amir G. Aghdam Examiner

Professor Brandon Gordon Examiner

Professor Wen-Fang Xie Supervisor

Approved by _____
Chair of Department or Graduate Program Director

_____
Dean of Faculty

Date April 13, 2016

Abstract

Real Time Pose Control of Parallel Robot

Sahar Alinia

Parallel robot is a kind of robot that uses several computer-controlled serial chains to support a single platform, or end-effector (EE). It has been widely used in the various applications such as aircraft simulator, high precision machining and aerospace manufacturing, etc. However, achieving high precision pose control of 6-DOF parallel robot makes a challenge for robotic researchers due to the lack of dynamic modeling of robot and accurate measurement of pose. The present research study aims at controlling the pose of end-effector (EE) of 6-RSS parallel platform in real time.

In this thesis, the kinematics of the robot including the inverse and forward kinematics are presented. The numerical solution of forward kinematics model is provided and the forward kinematic model is implemented in the Simulink to serve as the parallel robot for the pose control design. A Simulink model is built in order to simulate and implement the pose controller for the parallel robot.

The parallel robot consists of six Brush-Less DC (BLDC) actuators. Both linear and nonlinear dynamic models of the DC motors are derived. The parameters of linear dynamic models are identified using Genetic Algorithm (GA). Also, the parameters of nonlinear actuators' dynamic model are identified using the multi-objective optimization method. Then a proportional-integral-derivative (PID) controller is used to control the EE and track the desired trajectory. The simulation results demonstrate an outstanding tracking performance for the designed PID controller.

To further validate the designed pose controller in the real time experiment, we use the photogrammetry sensor–C-track from Creaform Inc. to obtain the pose of EE. By comparing the desired pose with the current measured pose by C-track, the inverse kinematic model of the parallel robot is validated and the experimental results demonstrate that the inverse kinematic model is accurate enough for the subsequent real time pose control.

In order to control the pose of the parallel robot, the pose measured by C-track is used to implement the real time pose feedback control system. Since the C-track is connected to one computer and the parallel robot is connected to a different computer, it is necessary to transfer the obtained pose data by C-track from one PC to the other one that controls the actuators of the parallel robot. A serial port has been used for the real time data transferring. A lot of effort has been dedicated to the retrial of the pose data in the real time pose control Simulink blocks. Finally, six PID controllers are applied to track the pose of the EE. The experimental results show an acceptable pose tracking control of the system.

Acknowledgments

My greatest thanks are to my special advisor Prof. Wen-Fang Xie, who helped me during these years and with the challenges I have faced. She made me feel supported all the time and she helped me in all areas of my graduate life gently. I strongly believe that working under her supervision is one of the very rare chances that a graduate student can be given and for this I am grateful.

I am deeply thankful to all the FQRNT group for creating a stimulating environment for discussion. In particular, I thank Prof. Hoa for his openness to sharing his ideas.

I am specially grateful to Rui and Xiaoming for helping me in our group.

Special thanks also goes to Masoud Hemmatian, Amir Gahroosi and Amir Hajiloo for their help and prompt feedback. Furthermore, my heartfelt thanks goes to my dear friend Morteza Rezanejad for helping me a lot with his insightful comments, and support.

I would like to thank all of my friends in Montreal city who have been supporting me on a daily basis: Matin Komeili, Omid Rezania and MohammadHadi Farzaneh Kaloorazi. You have made me feel at home!

Also, I would like to thank my friends in Iran who have never forgotten me even though I am far away from them and they always give me motivation and enthusiasm for my future career: Iman Kermani, Majid beygi, Hosein Sadri Majd, Farzaneh Mohammadi and Zoha Ghasemi.

Last, but not least, my deepest gratitude goes to my family for their unflagging love and support throughout my life; this dissertation would not be possible without them. Thank you Maman, Baba, Daee Masoud and my grandma.

Contents

List of Figures

List of Tables

Chapter 1

Introduction

1.1 Overview

The goal of this project is to control the pose of 6-RSS parallel robot in real time in order to help the Automated Fiber Placement (AFP) machines produce composite structures with complex shapes. AFP machines are commonly used in industrial companies to produce simple composite shapes, however, they are not able to make complex shapes. As a result, a 6-RSS parallel robot is added to the current AFP machine to give it more dexterity. In this regard, finding the kinematics and dynamic model of 6-RSS parallel platform, such as deriving the forward and inverse kinematic equations of 6-RSS robot, modeling its actuators, obtaining the exact pose of end-effector, and achieving accurate pose control are the main challenges in this research study. Although many researchers have done several research works regarding the control of the pose of parallel robots, most of the research works has been done for the robots having simpler structure in comparison with the 6-DOF parallel robot or they are not implemented in real time.

This chapter first introduces the difficulty of producing the complex composite shapes by AFP and gives a solution to overcome this difficulty. Some related topics and previous works on parallel robots and its structure are given. The following section is dedicated to problem statement of using AFP machines for producing complex composite structures. The objectives of this work is explained in Section 1.3. In Section 1.4, the summary of the work is done in this research study is outlined. In Section 1.5, the literature survey on the kinematics of parallel robots, the identification of DC motors and controlling the pose of parallel robots are given. Finally, Section 1.6 gives the

organization of this thesis and Section 1.7 gives the summary of this chapter.

1.2 Problem Statement

Recently, the increasing usage of composite structures, especially in aerospace industry, motivated researchers to improve the flexibility and manufacturability of the Automated Fiber Placement (AFP) machines. Before using AFP machines, the well-known method of manufacturing is handy-lay-up which has serious disadvantages; the process is time consuming and the substantial amount of materials waste. AFP machines have improved the methods of manufacture of composites in terms of speed, repeatability, good compact and reduction of waste. However, the current AFP machines are mainly designed for the manufacture of components having the shape of shallow plates, shells and tubes with different cross sections such as circular and elliptical. Hence these AFP machines need some modifications by adding more degree of freedom, because it is difficult for AFP machines to produce complex shapes such as tubes with double curvature or with T-shapes or Y shapes, tube with flanges and closed loop bicycle frames (see Fig.1.1 and Fig.1.2).

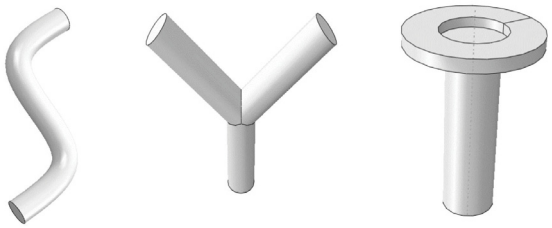

Figure 1.1: Frame with complex structure

Figure 1.2: Impossible for AFP to manufacture bicycle frame

Two possible solutions are considered: One possible solution is to add a serial chain manipulator to handle such complex structures. Unfortunately, serial robots incline to bend under heavy loads and high speed which means that they could not carry heavy loads.

Another solution is to add 6-DOF parallel robots to the current AFP machines. Since 6-DOF parallel robot provides high stiffness for a given structural mass, high accuracy and capability of carrying heavy loads [4], it is an ideal mandrel holder for AFP to increase the flexibility of composite manufacturing.

(a) Adding Serial Manipulator for Collaboration (b) Adding Hexapod for Collaboration

Figure 1.3: Two possible solutions to improve AFP Machines

To achieve this, a 6-RSS parallel robot, also called Stewart platform which is available in Concordia University, has been added to the current AFP machine, in order to improve the performance of the AFP machine to manufacturing of composite components.

1.3 The Objective of Research Work

The aim of this work is to add 6-RSS parallel robot to AFP machines in order to increase the flexibility in manufacturing of composites. Therefore, obtaining the exact pose of the 6-DOF parallel robot is necessary. To achieve this, the actuators' model and the inverse kinematic model of the parallel robot need to be built and identified. Then, C-track is applied to track the exact pose of EE in real time. The pose obtained by C-track can be used to validate the derived inverse kinematic model of the parallel robot.

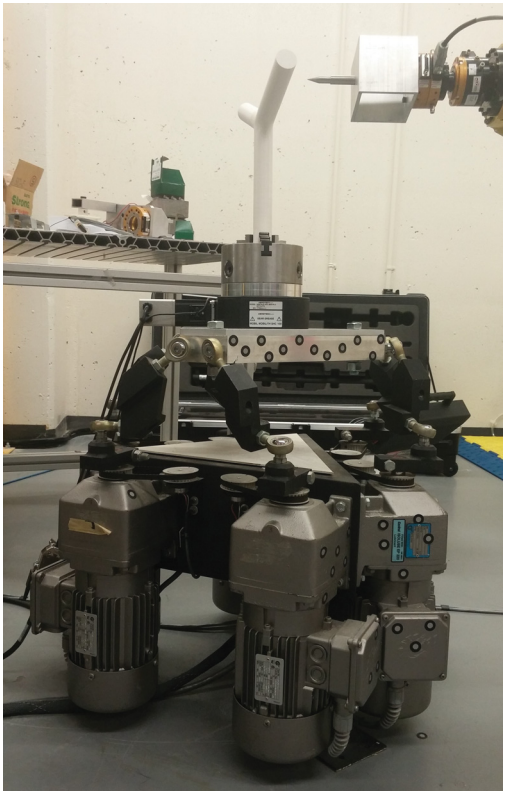

Figure 1.4: Parallel robot available in Concordia

Figure 1.5: AFP available in Concordia

1.4 Contributions of the Thesis

The main contributions of the thesis are listed as follows

1. Both Inverse Kinematic (IK) and Forward Kinematic (FK) of 6-RSS parallel robot are analyzed. The IK model is derived using intractable problem between ball and circle, which is required to control the parallel robot both in simulation and experiments. Since solving the FK problem of 6-RSS parallel robot is complicated and produce multiple solutions, a simple numerical method is used to solve the FK problem which gives us an unique answer. A FK block is build in Simulink block diagram and it is used instead of real robot to gives us a pose of the end-effector (EE). This FK block is used to control the pose of EE in simulations.

2. Both linear and nonlinear dynamic models of each actuator are derived through optimization methods. First, the effect of friction is neglected and the parameters of the linear brushless DC motor model are identified using Genetic Algorithm (GA). Then, the effect of friction is considered and multi-objective optimization method is used to identify the parameters of nonlinear brushless DC motor model.

3. Designing PID controller for the pose control of a 6-RSS parallel robot in simulation. In order to control the pose of EE in simulation, both IK and FK blocks are used. The simulation results indicated that the optimized PID controller tracks the pose of EE well.

4. Using C-track, the pose of EE is obtained in experimental works. Then the inverse kinematics of 6-RSS parallel robot is validated. In order to validate the inverse kinematic block, the length of each link of parallel robot is calibrated. C-track is used for this calibration and the links' lengths are measured and substituted for links' lengths measuring by ruler.

5. Two different PCs are used in the lab. One PC is connected to C-track and stores the measured data from C-track. The other PC is connected to parallel robot and through two Quanser cards we can control the robot. We succeed in transferring the data from the first PC to the second one and running two Simulink models at the same time. This robot enables us to have the feedback for pose control of the system.

6. Six different PI controllers are designed to control the pose of EE in real time. Also, six low pass filters are used to reduce the effect of noise. The experimental results show that these PI controllers can track the desired pose at a satisfactory accuracy.

   Also, the following lists are our publications during these two years:

   - Alinia, S., Hemmatian, M., Xie, W.F. and Zeng, R., 2015, May. Posture control of 3-DOF parallel manipulator using feedback linearization and model reference adaptive control. InElectrical and Computer Engineering (CCECE), 2015 IEEE 28th Canadian Conference on(pp. 1145-1150). IEEE.
   - Sahar Alinia, Amir Hajiloo, Wen-Fang Xie, Suong Hoa, 2015, Identification of the dynamic model of 6 RSS parallel robots actuators. Poster IROS. IEEE
   - Sahar Alinia, Wen-Fang Xie, Xiao-Ming Zhang. 2016, Modeling and pose control of a 6-RSS parallel robot using multi-objective optimization, CSME accepted

1.5 Literature Review

1.5.1 Inverse and Forward Kinematics

The analytical study of the robot's motion without considering the forces is called kinematics analysis which is classified into two parts [5]:

1. Inverse Kinematic (IK): Inverse kinematics problem is expressed as determining the joint variables of manipulator with respect to the given position and orientation of the EE.

2. Forward Kinematic (FK): Forward kinematics problem is defined as determining the pose of EE with respect to base frame using given joint displacements.

In order to obtain the pose of parallel robot, analyzing the kinematics of robot is necessary. To obtain the IK and FK of robots, two main challenges are considered:

- Number of degree of freedom (DOF): As the number of DOF is increased, deriving the kinematic equations becomes more complicated.

- Types of robot: There are two types of robot, serial and parallel robots. In serial robots, several series links connect the EE to the base. In contrast, the parallel robot is a robot in which the base is connected to EE by several parallel links.

  Depending on which kind of robot is studied, the complexity of obtaining the kinematics of robot differs. For example, deriving the inverse kinematic equations of parallel robot is much easier in comparison with that of serial robots. Whereas, deriving the forward kinematic equations of parallel robot becomes very complicated. There is no unique solution when we try to solve the FK equations of parallel robot. The more degree of freedom the robot has, the more answers that the FK problem has.

There are two main methods to solve the FK problem, i.e., analytical and numerical methods. The analytical method involves a lot of mathematic derivation and cannot give unique solution while the second one calculates the pose of EE based on numerical techniques. Many studies have been contributed to derive both inverse and forward kinematics of parallel robots.

1.5.1.1 Analytical Examples

In 1992, Shi et al.[6] presented a method to solve forward kinematic problem of 6-DOF Stewart platform. This method was based on three point velocities of the end-effector. In this method, six linear equations were solved. This method is easy to implement for the robot with six prismatic joints.

Tsai et al.[7] solved the forward kinematics of 3 DOF parallel platform using Bezouts elimination method in 2003. This method gave 64 possible solutions for FK problem. By applying some physical limits, the sought solution could be obtained. Also, they proposed one optimization method in order to find the pose of end-effector. This approach consumed less analysing time in comparison with Bezouts elimination approach, because there was no need to calculate all possible solutions. Also, Bezouts elimination approach might not be employed in real time applications due to the optimization process and it was developed for 3 DOF Stewart robots.

Three years later, in 2007, Huang et al.[8] presented a novel method to solve the forward kinematics of 6-DOF Stewart robot. This method is called Algebraic Elimination which is convenient for real time applications. In this algebraic method, they obtained the determinant of the 15x15 Sylvesters matrix in which 20th degree univariate polynomials were obtained. The proposed algorithm could compute the forward kinematics in a short time and gave all the solutions briefly but comprehensively. The obtained results by algebraic elimination method were confirmed by numerical method. This method is used for general 6-DOF robots which consist of prismatic joints.

1.5.1.2 Numerical Examples

In 1991, Geng et al.[9] proposed the extended cascaded Cerebella Model Arithmetic Computer (CMAC) structure based on the Neural Networks (NNs), in order to find the Forward Kinematic (FK) of a Stewart platform. This extended CMAC network structure in comparison with a standard single CMAC which had coarse and veneer nets. These coarse and veneer nets had different ranges of input and output sensors which increased the faster learning ability of the complicated nonlinear mappings. This means that the proposed method needed less time to be trained and could solve the problem much faster than traditional FK solving methods. Also, they applied back propagation algorithm to train NN in order to solve the FK problem. The comparison between Cascaded CMAC and back propagation trained NNs, showed that the performance of the proposed method was more ideal than the second one. This method was used in 1991 while other researchers proposed simple numerical methods during last decade.

In 1993, Cleary et al.[10] used a numerical solution in order to solve the FK problem for 6-DOF parallel platform. This method could be used in real time applications because of its high speed of analysis. This method was used to solve a novel 6-DOF robot which is completely different from

6-RSS robot.

At the same time, Liu et al.[11] presented a simple method in order solve the FK problem of 6-DOF general Stewart platform. Despite of many other algorithms which provided at least 30 equations, this method just gave three equations which should be solved at the same time. They used Newton-Raphson method to solve these three equations. This method is used for the Stewart platform having prismatic joints.

Three years later, McAree et al.[12] proposed an approach to solve the forward kinematic equations of Stewart platform. This method was based on Newton-Raphson scheme, which was very robust and reliable in finding the FK solution. Also, this striking approach required short computational time and the performance was trustworthy, even though it faced with singularities. While this methods is fast enough to solve the FK problem, Wang[13] proposed a numerical method later which is simpler.

In 1997, Yee et al.[14] presented a novel neural network (NN) method in order to find the forward kinematics (FK) solution of parallel manipulator (PM). Using inverse kinematic (IK) solution, NN finds the solution by solving a series of nonlinear equations. A type of NN which was used to solve FK equations is called feed-forward network. This proposed method was more precise than traditional NN ones. Although it took less time rather than the other NN methods, it is still time consuming.

In 2002, Mu et al.[15] presented a numerical method based on polynomial continuation to solve the FK problem for most Stewart platforms. They simplified a geometry of a real Stewart platform to platform which was the start system. Instead of using pure mathematical equations, they used start platform based on physical design. 18 second-order polynomial equations were developed based on the distances between limbs connection points and limbs lengths. A homotopy was created between the equations of real Stewart platform and start one. The parameters of start system were changed into real ones using the created homotopy. With this homotopy, every obtained solution for start system was tracked through a path in real space that led to find a complete set of 40 solutions for real platform. This method was verified through a numerical experiment and it is used for general 6-DOF robots which consist of prismatic joints.

In 2006, Wang [13] presented a simple numerical method to solve FK problem of 6-DOF parallel manipulators. This numerical method was based on trivial nature of inverse kinematics of

parallel platforms. Small changing in leg lengths led to small motion for robot. Using this, a linear relationship between this two changes was derived. Then, a unique solution for FK problem was obtained using a series of small leg lengths changes. This method was verified through numerical examples.

In 2009, Parikh et al.[16] proposed an artificial neural network (ANN) method based on iterative strategy to solve the FK problem. This method was useful in real time applications and gave precise solutions. The comparison between the proposed method and single-layer ANN showed that the more accurate solution could be obtained. Using the proposed method, the number of iterations was less than five with acceptable error in terms of Stewart platform's pose. Although this method has accurate solution for FK problem it takes too much computational time.

In 2013, Morell et al.[17] proposed a spatial decomposition method to solve forward kinematics of 6-DOF Stewart platform. This method did not depend on geometry of the Stewart platform. In order to model the behavior of the platform in a given region of pose space, a famous machine learning method was applied. This machine learning method is called the Support vector machines (SVMs) which is used as a regression model in FK problem which is difficult to be implemented.

Solving the FK through numerical method is much faster. For our project, a simple numerical method [13] is used to save the time and gives an accurate solution.

1.5.2 Identification of DC Motor

The basic structure of 6-RSS parallel robot, available in lab, includes 6 DC actuators serving as actuators. Having the enough knowledge of these actuators is a crucial step towards analyzing the behavior of the system.

The dynamic model of the actuators is usually classified into two categories:

- Linear model: This type of model only considers the force and motion in a straight line which cause low frictional loss [18]. As a result, the dynamic equations of this motor could be derived without considering the effect of friction.

- Nonlinear model: Mostly, the effect of friction is substantial in the motor, so friction force must be considered when the dynamic model is derived. This type of model which considers the friction force, is called nonlinear actuator's model.

In order to operate, design and implement the motion control system for the actuator, both static and dynamic mathematical models are required. These basic static and dynamic behaviors are described by theoretical or physical modeling principles. Sometimes, the values of the required parameters for modeling are not known. As a result, system identification is required to estimate the parameters of the model. The identification of system dynamic model has been studied since 1960s [19].

In this thesis, in addition to the geometrical parameters of the robot, having the precise values of the parameters of DC motor in order to control the system is required. The main challenge is to consider the effect of friction. Considering the friction force in dynamic equation during the identification, increases the processing time and makes system complicated. In this research, a nonlinear DC motor model is identified using multi-objective optimization method to increase the accuracy of identification.

Many researchers have carried out research in identifying both linear and nonlinear DC motors' models and many papers have been published in this regard:

In 2004, Kara et al.[20] identified linear and nonlinear DC motor models. In order to identify the nonlinear system model, a nonlinear Hammerstein structured was used. A discrete time ARX model was used to identify the linear part. For nonlinear part, the Recursive Least Squares (RLS) method was implemented. Although Hammerstein method was not able to be employed to control the online DC motor, it could identify the dead-zone features well. The experimental results showed that the nonlinear model performed better than linear one for low speed process.

In 2005, Krneta et al.[21] identified parameters of DC motor using Recursive Least Squares (RLS) method. In order to validate the experimental results, they used optical encoder to measure the angles of motor. Comparing the speed of motor measured by optical encoder with the speed of identified system, the identified parameters were matched with the real ones. They simulated the identified model in computer and compared the real motor's speed with the speed of identified one in a Z and S domain. The simulations and experimental results showed a satisfactory identified DC motor model. Two year later, Nasri et al. [22] presented a Particle Swarm Optimization (PSO) method to identify the motor model and PID controller for a linear brushless DC motor. The simulation results from PSO with GA and Linear Quadratic Regulator (LQR) method, shows the better performance of optimized PID controller. The rise time, steady-state error, settling time and

maximum overshoot are reduced in this method in comparison to LQR and GA in addition to the improved computational efficiency and easier implementation.

In 2007, Mamani et al.[23] presented an on-line, non-asymptotic, algebraic identification method to identify the parameters of DC servo motor model. This method just depended on the input voltage and angular position of the motor so it does not need initial conditions. This method could give the estimations in a short period of time. Also, the Coulombs friction coefficient of servo motor was identified. Both high frequency noises and Coulomb friction torque were applied to the system. The experimental results showed a good robustness of system in presence of noise and friction.

In 2011, Peng et al.[24] identified a nonlinear DC motor system with dead-zone characteristics. They modeled the DC motor using Wiener-type Neural Network (WNN). In order to control the DC motor, PID-type Neural Network (PIDNN) was designed. Then, an adaptive PID-type neural network control is proposed based on WNN. The designed controller is reported to have a satisfactory performance.

At the same time, Bhushan et al.[25] identified and controlled the DC servo motor speed to track the trajectory using Bacterial Forging Algorithm (BFA). The simulation results showed that the designed adaptive controller tracked the desired trajectory very well. The estimated angular speed of DC servo motor can approximate within a reasonable error. Also, they used GA based on adaptive control to track the speed trajectory. Although the simulation results showed the speed trajectorys error was less than that in BFA adaptive control, BFA adaptive controller needed less computational time and works more efficiently.

At the same time, Wu [26] presented an identification method based on Tylor series expansion of the motor speed response under a constant voltage input. This method could identify the parameters of DC motor such as, torque constant, electrical time constant, mechanical time constant and friction. This approach was applied to modeling a Mabuchi RK370CA and Mabuchi FC130 motors. The systems were assessed under two conditions; with disturbance-torque and without disturbance-torque. Then a model of motor has identified and verified bt the experimental results.

In 2014, Farid et al.[27] employed Particle Swarm Optimization (PSO) method to identify nonlinear DC motor model. Also, a controller was designed based on adaptive neuro-fuzzy inference system. The control algorithm was implemented using Atmega32 microcontrollers. This method

decreased computational cost considerably. Also, the cheap microcontroller were used to realize. The simulation results showed the satisfactory control.

Although many DC motor models have been identified so far using different methods, most of them are based on simulation results. In this research both linear and nonlinear DC motor models are identified using GA and multi objective optimization, respectively and are validated by experimental results.

1.5.3 Pose Control of Parallel Robots

In addition to establishing kinematics models of the robot and identifying the parameters of robot's actuators, obtaining the exact pose of end-effector (EE) is necessary. Since the mandrel for fiber layup is located on the EE of the parallel robot, the exact pose of EE must be determined for the fiber placement. When the parallel robot is moving to the desired pose, it usually has some errors which will affect the accuracy of fiber placement. To reduce this error, a controller should be used. In this thesis, a set of PID controllers is used to control the pose of parallel robot in real time. There are several papers are published regarding linear and nonlinear pose control of parallel robots. The main challenge lies in controlling the pose of 6-RSS parallel robot simultaneously in real time. Six controllers should be tuned to deliver a satisfactory pose tracking performance. The second challenge is that we have to apply these controllers in experiments which is a very demanding and needs excessive effort.

Some researches have been reported in the literature regarding the pose control of parallel robot:

In 2004, Huang et al.[28] presented a sliding mode control method to control the motion of 6-DOF Stewart platform with some parametric uncertainties. The only measurable parameters were the positions and velocities of the links. These types of controller were model-based and require the dynamic model of Stewart platform. They derived important dynamic properties of the system. The experimental results indicated an outstanding performance for the designed controller.

In 2005, Huang and Fu [29] controlled the motion of Stewart platform using a smooth sliding mode control method. The only measurable parameters were the positions and velocities of the links while other parameters are subjected to uncertainties. These types of controller are model-based and require the dynamic model of Stewart platform. They derived the important dynamic

properties of the system. They analyzed the stability of system using Lyapunov theory and showed that the controller was stable.

In 2006, Sun et al.[30] proposed a cross-coupled control approach for synchronous control of 3-DOF Stewart platform. Comparing with most of the synchronous controller, this controller was easy to implement because the explicit knowledge of dynamic model of the system was not required. In this paper, this synchronous control was compared with two other controllers, i.e., conventional PID and adaptive controllers. The experimental results showed that the proposed controller had smaller position error of EE and the smaller position errors of the three prismatic joints.

Zhu et al.[31] presented a discontinuous projection-based adaptive robust control strategy for a 3-DOF parallel manipulator driven by pneumatic muscles. The time-varying friction forces and the static force dynamic modeling errors of pneumatic muscles caused harsh parametric uncertainties and uncertain nonlinearities for the system. The proposed controller was used to reduce these nonlinearities and uncertainties. Both simulation and experimental results showed the proposed adaptive controller tracked the desired pose accurately. Also, they presented an adaptive robust control (ARC) to control the pose of a parallel manipulator driven by pneumatic muscles (PMDPM) with a redundant DOF. The experimental results showed a precise pose tracking control for the system.

In the same year, Zhao et al.[32] developed a fully adaptive feedforward feedback synchronized tracking controller for a 6-DOF Stewart platform. There had been an error between the obtained feedforward control gains and real parameters. The error effects were compensated using the saturated controller. They compared the proposed controller with two other controllers, i.e., PID controller and synchronized controller (A-S) control. The simulation results showed that the proposed controller and A-S control tracked the desired pose well and has less error than PID controller. The dynamic structure of Stewart platform is very complicated. The advantage of proposed controller is that could be implemented without any knowledge of the dynamic structure of Stewart platform while A-S controller was model-based controller. As a result, this proposed controller was easier to be implemented and more applicable in practice rather than A-S one.

In 2011, Bo et al.[33] presented a control algorithm based on fuzzy logic and PID control algorithms. The designed controller is tested on experimental setup. Both simulation and experimental

results showed that the designed controller tracked the pose of Stewart platform precisely.

Also, Jian et al.[34] proposed a control method which is based on Narendras model reference adaptive control method. The simulation and experimental results showed a satisfactory performance of the proposed controller.

In 2012, Srikanth et al.[35] presented a mathematical model of a three-phase BLDC motor. Then, two PID controllers were designed using GA and Ziegler Nichols method (ZN). Although ZN was effectively used to estimate the initial values of PID gains in GA, the simulation results showed the better performance of the controller tuned by GA. The performance index, such as the rise time, settling time, overshoot of the controller tuned by GA were reduced in comparison with that of the tuned controller by ZN.

In 2015, Alinia et al.[36] designed two model-based controllers (i.e. feedback linearizion and model reference adaptive controls (MRAC)) for a 3-DOF parallel manipulator driven by pneumatic muscles (PMDPM). Two controllers were developed to control the pose of moving platform by changing the pressure inside the pneumatic muscles. The simulation results showed the satisfactory tracking performance of the designed controllers under sudden disturbances and their robustness against the noise. The MRAC exhibited better control performance compared with feedback linearizion controller.

Above literature survey shows that a lot of research in the pose control of the parallel platforms. However, most of the controllers are not implemented in real time. Also, many of the controlled robots have less than 6 DOFs. This project aims at controlling the pose of 6-RSS parallel robot in real time. To do so, some experiments have been done which is very time consuming and challenging. The results show the satisfactory pose tracking of the EE's pose.

1.6 Dissertations Organization

This work has been organized as follows: In the following chapter, the definition of the 6-RSS parallel robot, R stands for revolute joint and S for spherical joint, which is available in Concordia University, is presented. Then, the inverse kinematic equations of the 6-RSS parallel robot, is obtained. Moreover, based on the inverse kinematic model, an appropriate direct kinematic solution is required to obtain the EE's pose of the parallel robot, theoretically.

In order to simulate with the parallel robot for pose controller design, in Chapter 3, the linear brushless DC actuators' models are identified. Also, the nonlinear brushless DC motor model and corresponding dynamic equations are given. Then, GA is used to identify the parameters of nonlinear brushless DC motor model. Moreover, the multi-objective optimization method using GA is selected to identify the parameters of nonlinear DC actuator model considering the friction. Then, a PID controller is used to control the actuators and the gains of the PID controller are tuned by using GA.

In Chapter 4, a C-track is used to obtain the pose of EE. The parallel robot is modeled in VX-elements provided by C-track, and the inverse kinematic model is verified. Then, the data obtained by the C-track is transfered from one PC to another one by using the serial port. In order to control the pose of EE, the obtained pose by C-track is compared with the desired pose and the pose error is input to the controller. Finally, the thesis is concluded and future work is provided in Chapter 5.

1.7 Summary

In this chapter, a brief introduction of basic concepts of the current research has been presented. A literature review on the existing works on the kinematics analysis of model identification of DC motor and pose control of parallel robots has been given. The information on research objectives and the thesis organization are also given in this chapter.

Chapter 2

Kinematic Analysis of Parallel Robot

To design the pose controller for the parallel robot in simulation, it is necessary to conduct the kinematic analysis of the robot for simulating the robot. Both inverse and forward kinematic equations are required for pose control in the simulations. The forward kinematic model will be combined with the dynamic model of the actuators to mimic the parallel robot behavior and the pose information output of the parallel robot can be obtained from this model to serve as the feedback signal for closed-loop pose control system. While the inverse kinematic model can be used to generate the command to the actuators in the simulation. The main objective of this chapter is to derive the kinematics of 6-RSS parallel robot in order to control the pose of EE. The accuracy of these equation are validated experimentally in the following chapters.

This chapter is organized as follows: In Section 2.1, the parallel robots are introduced and a brief history of parallel robots is given. In Section 2.2, 6-RSS-DOF parallel robot, which is available in Concordia university, is described. Then, the inverse and forward kinematics of 6-RSS parallel robot are obtained and modeled in Simulink block diagram.

2.1 Introduction of Parallel Stewart Robot

Nowadays, robot manipulators are commonly used in manufacturing industry to fulfill different tasks, such as spray painting, spot welding, lifting different parts with different mass, assembling, etc[37]. There are two types of robots which are widely used in industrial applications. The first one is called parallel robot and the second one is known as a serial robot.

Parallel robot is a kind of robot built with closed-loop chains. Using at least two kinematic chains, the base is connected to EE. A kinematic chain consists of several links which are linked by joints. In overall, parallel robot is defined as a mechanism in which the base is connected to EE through several chains. A serial manipulator is a robot built with an open-loop chain structure, which means that only one path connects each link to other link.

The main difference between serial robots and parallel manipulators is their structure. In serial robots the base is connected to EE through several series links, while in parallel robots the base and EE are linked by a number of parallel linkages.

The origin of Stewart parallel platform dates back to 1920s, when French and English mathematicians were interested in polyhedral. The first parallel robot was invented by James Gwinnet in 1928. He invented a 3-RRR parallel robot as an entertainment device for movie theater (see Fig.2.1) [1].

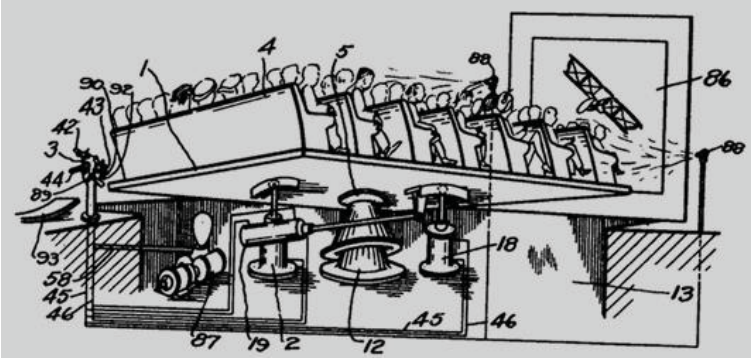

Figure 2.1: Entertainment device for movie theater [1].

As it is shown in Fig.2.2 (a), Willard L.V.Pollard invented a parallel robot for spray painting and controls the position of a spray gun, in 1940 and 1942 respectively [38], [39]. A 6-DOF parallel robot is designed by Eric Gough in 1947 where the industry is hit by such invention [40] (see Fig.2.2 (b)). This well-known robot is called universal machine and is used in tire inspection. In 1965, Stewart presented a 6-DOF parallel robot which was different from Goughs parallel platform. This robot is used as a flight simulator (see Fig.2.3) and made an evolution in both industry and academic research [2]. In 1967, Klaus Cappel, proposed a motion simulator hexapod which made him the third pioneer in the field of parallel robots.

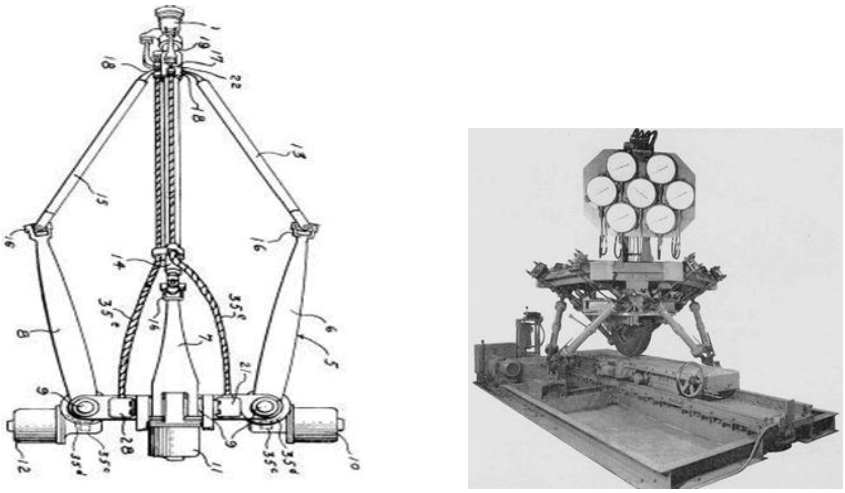

(a) Spray painting robot [38] and [39]. (b) Tire inspection robot [40].

Figure 2.2: Parallel robots

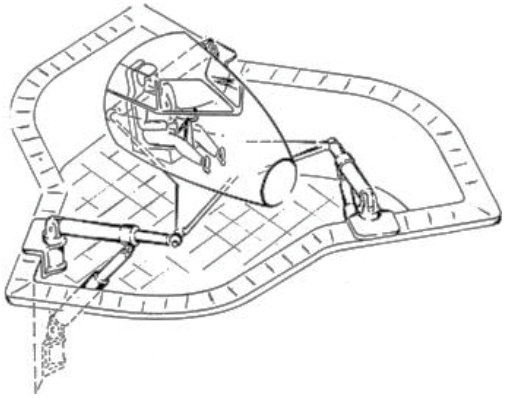

Figure 2.3: Flight simulator [2]

Due to the following features, parallel robots are widely used in industries application where the conventional serial robots have some limitations:

- Higher stiffness: They provide higher stiffness for a given structural mass in comparison with the serial manipulators [41].
- Strong load bearing: Parallel robots are able to carry heavy loads; therefore, they are used as flight simulator, automobile simulator, tank simulator, earthquake simulator and so on [4].
- Satisfying dynamic performance: They have high velocity and acceleration for pick-and-place concept, such as delta robots [42].

- Less accumulated errors of joints: In serial robots, the errors accumulate because the links are series, while in parallel robot the errors of parallel links are averaged [43]. It is used as micro-manipulators or manipulator for ophthalmic surgery operation where the high accurate positioning is required [4], [43].

- Simpler inverse kinematics. The inverse kinematic equations of parallel robots are much easier than serial robots which makes them more suitable for real time application [1].

- They are used in many other applications such as, Neuro-surgical robot [44], optical fiber alignment [45], and so on.

However, there are some drawbacks in the parallel robot, such as;

- Small workspace: The work space of parallel robot is much less than that of serial robots. Finding the work space of parallel robots, also, is more difficult than that of serial ones [1].

- Complex dynamic model: It is difficult to find the dynamic equation for parallel robots [40].

- Complex forward kinematic model: It is very complicated to find the unique solution to forward kinematic equations of parallel robot. So, many researchers tried to find the unique solution to the FK equations by using numerical methods [40].

2.2 6-RSS Parallel Robot

As it mentioned in Chapter 1, the aim of using 6-RSS parallel robot is to add more dexterity to the current AFP machines. Therefore, obtaining the exact pose of the parallels EE is necessary. The current 6-RSS robot, available in Concordia University, and its features are given in this section.

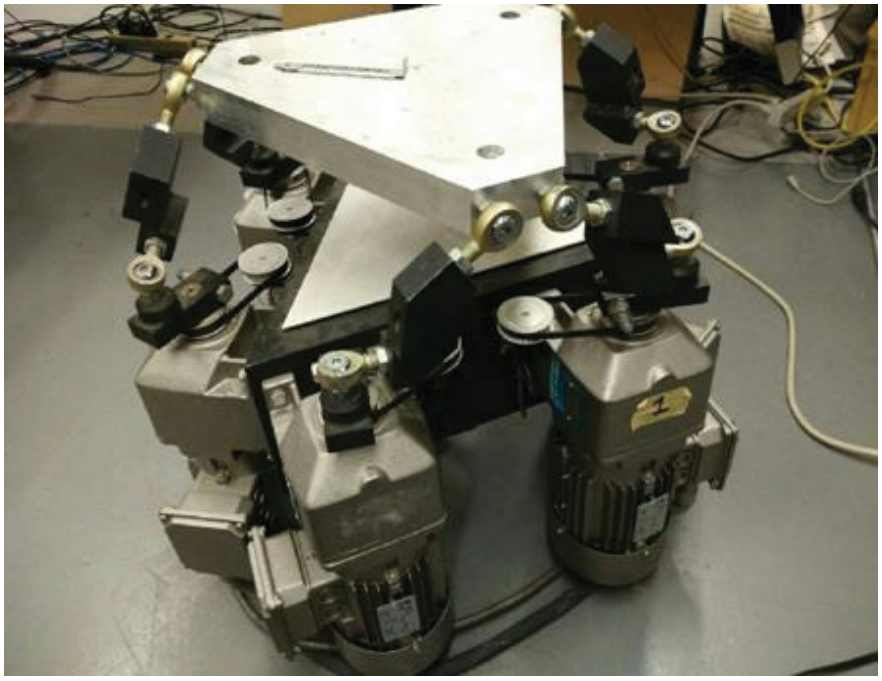

Figure 2.4: 6-RSS parallel robot

Fig.2.4 shows the parallel robot, available in Concordia University.

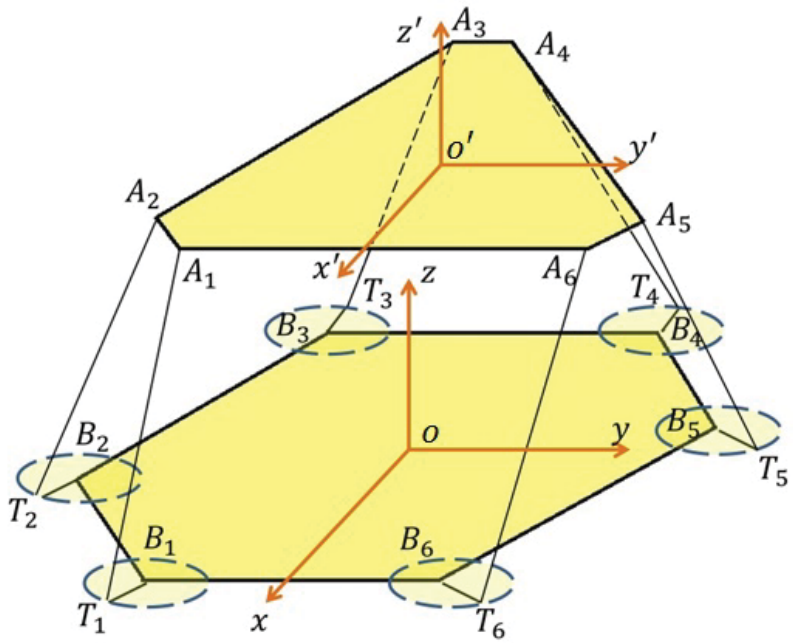

Figure 2.5: Geometrical parallel robot

Fig.2.5 shows the geometric structure of the 6-RSS parallel robot. The singularity and workspace

analysis have been given in [46]. This robot consists of the following parts:

- A moving platform which has translations of motion along x-y-z axes and three rotations around all axes.
- A base platform which is fixed.
- 6 rotary actuators which are DC brushless motors.
- 6 links (AT_i) and 6 links $(BT_i), (i = 1, 2...6)$.

As it is shown in the figure, two frames ($Oxyz$ and $O'x'y'z'$) are considered in which the frame $Oxyz$ is fixed to base platform and used as the reference frame, and the frame $O'x'y'z'$ is attached to the moving platform. The posture of the EE is defined as the rotating angles around x by role angle (α), y axis by pitch angle (β), z axis by yaw angle (γ), respectively. Also, there are translations along x, y and z directions. B_i is a revolute joint and the location of actuators. BT_i linkages are located in x-y which rotates about B_i in z direction. A_i and T_i are spherical joints which let the moving platform has three rotations and translations along three axes.

2.2.1 Kinematics Modeling

Kinematics studies the motion of bodies without considering the forces or moment that causes the motion. In other word, the analytical study of the motion of robot represents robot kinematics. Formulating suitable kinematics modeling of the manipulator is very crucial for analyzing the behavior of industrial manipulators [5].

The robot kinematics includes forward kinematics and inverse kinematics.

1. Inverse Kinematics: Determination of joint variables in respect of end-effector position and orientation is called inverse kinematics. To control the end-effector to reach a pose, the inverse kinematic must be built.
2. Forward Kinematics: Calculating the position and orientation of the end-effector according to the joint variables is called forward kinematics. To simulate the parallel robot for pose control design purpose, the forward kinematics model must be built as well.

Solving inverse kinematic equation of parallel manipulators is straightforward while for serial manipulators is very complex and time taking. In contrast, forward kinematics problem of serial manipulators is easy to be solved whereas for parallel manipulator, solving forward kinematics problem is very challenging. It is computationally expensive and requires a lot of mathematic derivations. Some difficulties should be considered while deriving forward kinematic equations especially when the structure of manipulator is complicated. The more degree of freedom the robot has, the more complex manipulator's structure becomes. This complexity causes multiple solutions and singularities.

The relationship between forward and inverse kinematics is illustrated in Fig.2.6.

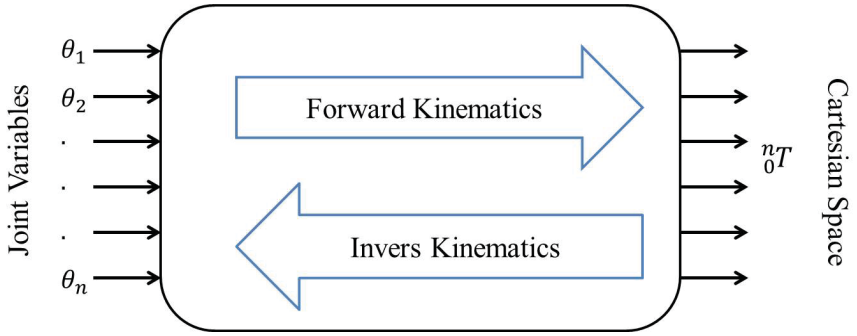

Figure 2.6: The schematic representation of forward and inverse kinematics.

There are two main methods to solve forward kinematics, analytical and numerical methods. In the first method, a lot of mathematics derivations are required. In the second one, calculating the position and orientation of the end-effector are obtained based on the numerical techniques. Compared with the analytical method, the numerical method is faster and accurate enough when the structure of robot is complex, i.e., the robot has 6 DOFs [5].

2.2.1.1 Inverse Kinematic Modeling of 6-RSS Robot

The determination of joint variables from end-effector's position and orientation is called inverse kinematics. To control the end-effector to reach a desired pose, the inverse kinematic equations must be solved.

In this section, the inverse kinematics equation of 6 DOF-RSS parallel robot is presented.

The position of EE with respect to the coordinate of O' in xyz frame, is defined as follows:

$$EE = (x, y, z, \alpha, \beta, \gamma) \tag{2.1}$$

Also, the rotation matrix of $x'y'z'$ frame respect with xyz frame is obtained as,

$$R = \begin{bmatrix} cos(\gamma) & -sin(\gamma) & 0 \\ sin(\gamma) & cos(\gamma) & 0 \\ 0 & 0 & 1 \end{bmatrix} \begin{bmatrix} cos(\beta) & 0 & sin(\beta) \\ 0 & 1 & 0 \\ -sin(\beta) & 0 & cos(\beta) \end{bmatrix} \begin{bmatrix} 1 & 0 & 0 \\ 0 & cos(\alpha) & -sin(\alpha) \\ 0 & sin(\alpha) & cos(\alpha) \end{bmatrix} \tag{2.2}$$

where, α is rotation angle about x direction, β is rotation angle about y direction and γ is rotation angle about z direction.

For each link, there exists the relationship as follow,

$$OO' = OB_i + B_iT_i + T_iA_i + A_iO' \tag{2.3}$$

as we defined above, the coordinate of O' is:

$$O' = (x, y, z) \tag{2.4}$$

The coordinates of A_i and B_i are obtained as,

$$A_i = RA_{0,i} + O' = (x_{A_i}, y_{A_i}, z_{A_i}) \tag{2.5}$$

$$B_i = (x_{B_i}, y_{B_i}, z_{B_i}) \tag{2.6}$$

where the $A_{0,i}$ is the initial position of A_i.

Also, from the intractable problem between ball and circle, we have the following equations:

$$(x_{T_i} - x_{A_i})^2 + (y_{T_i} - y_{A_i})^2 + (z_{T_i} - z_{A_i})^2 = (L_{AT})^2 \tag{2.7}$$

$$(x_{T_i} - x_{B_i})^2 + (y_{T_i} - y_{B_i})^2 + (z_{T_i} - z_{B_i})^2 = (L_{BT})^2 \tag{2.8}$$

where, $z_t = a$ and $z_b = 0$. From equation(2.7) and (2.8):

$$\begin{aligned} &2x_{T_i}(x_{B_i} - x_{A_i}) + 2y_{T_i}(y_{B_i} - y_{A_i}) + z_{A_i}^2 - 2az_{A_i} \\ &+x_{A_i}^2 + y_{A_i}^2 - x_{B_i}^2 - y_{B_i}^2 = L_{AT}^2 - L_{BT}^2 \end{aligned} \tag{2.9}$$

Then one has:

$$x_{T_i} = \frac{N_1}{2(x_{A_i} - x_{B_i})} - \frac{y_{A_i} - y_{B_i}}{x_{A_i} - x_{B_i}} y_{T_i} \tag{2.10}$$

where N_1 is defined as follows:

$$\begin{aligned} N_1 &= -L_{AT}^2 + L_{BT}^2 + (x_{A_i}^2 + y_{A_i}^2) - (x_{B_i}^2 + y_{B_i}^2) \\ &+ z_{A_i}(z_{A_i} - 2a) \end{aligned} \tag{2.11}$$

Substituting x_{T_i} from equation (2.10), in equation (2.8) yields:

$$N_2 y_{T_i}^2 + 2N_3 y_{T_i} + N_4 = 0 \tag{2.12}$$

Therefore, y_{T_i} is obtained as follows:

$$y_{T_i} = \frac{-N_3 + \sqrt{N_3^2 - 4N_2N_4}}{2N_2} \tag{2.13}$$

or

$$y_{T_i} = \frac{-N_3 - \sqrt{N_3^2 - 4N_2N_4}}{2N_2} \tag{2.14}$$

where, N_2, N_3 and N_4 can be described as follows:

$$N_2 = \frac{(y_{A_i} - y_{B_i})^2}{(x_{A_i} - x_{B_i})^2} + 1 \tag{2.15}$$

$$N_3 = -2\frac{(y_{A_i} - y_{B_i})}{(x_{A_i} - x_{B_i})}[\frac{N_1}{2(x_{A_i} - x_{B_i})} - x_{B_i}] - 2y_{B_i} \tag{2.16}$$

$$N_4 = (\frac{N_1}{2(x_{A_i} - x_{B_i})} - x_{B_i})^2 - L_{BT}^2 + y_{B_i}^2 + z_{T_i}^2 \tag{2.17}$$

When $\sqrt{N_3^2 - 4N_2N_4} \geq 0$, the desired pose is available. Furthermore, when the range of θ is between $[-\pi, \pi]$, the solution for y_{T_i} is unique.

Furthermore, there is a relationship between the coordinate of T_i and the rotation angle of each actuator (θ_i) as follows:

$$\begin{bmatrix} x_{T_i} \\ y_{T_i} \\ z_{T_i} \end{bmatrix} = \begin{bmatrix} cos(\theta_i + \theta_{0,i}) & -sin(\theta_i + \theta_{0,i}) & 0 \\ sin(\theta_i + \theta_{0,i}) & cos(\theta_i + \theta_{0,i}) & 0 \\ 0 & 0 & 1 \end{bmatrix} \begin{bmatrix} L_{TB} \\ 0 \\ 0 \end{bmatrix} \tag{2.18}$$

By substituting x_{T_i}, y_{T_i} and z_{T_i} in equation (2.18), the angle of each actuator (θ_i) is obtained:

$$\theta_i = \arctan(\frac{y_{T_i}}{x_{T_i}}) - \theta_{0,i} \tag{2.19}$$

2.2.1.2 Forward Kinematic Modeling of 6-RSS Robot

Calculating the position and orientation of the EE from the joint variables is called forward kinematics.

Although solving the inverse kinematic equations of 6-DOF parallel robot is straightforward, deriving the forward kinematics is complicated. In general, solving the forward kinematics results in multiple solutions. Each solution should be checked to determine whether or not the EE has reached the desired pose.

In this section, in order to obtain the pose of EE, an algorithm is presented to obtain the forward kinematic solution. It is difficult to find an unique solution for direct kinematic calculation. Thus the numerical verification method is proposed to determine the unique solution for the pose of EE.

The angle for each actuator is used to calculate the position of point T_i. Then the position of A_i can be determined, using the pose of EE. Therefore, the quasi-Gough direct kinematic algorithm is presented as follows:

First the initial pose (P) for EE is chosen, and the length of $(AT)_i$ is obtained. Second, comparing the calculated L_{AT_i} with the actual one, the error is calculated. If the error is acceptable, then the current pose is sent out as a result, else δp is calculated and $p = p + \delta p$ is used as the new one in next iteration.

To validate the forward kinematic, a Simulink schematic block (Fig.2.7) is built. A desired trajectory is defined as follows:

$$x = 0.017sin(2t) \tag{2.20}$$

$$y = 0.017cos(2t) \tag{2.21}$$

$$z = 0.1185 + (0.2/250)t \tag{2.22}$$

$$\alpha = 0.02sin(2t) \tag{2.23}$$

$$\beta = 0.02sin(2t) \tag{2.24}$$

$$\gamma = 0.05sin(2t) \tag{2.25}$$

where, t is time (sec), x, y, z are the position of EE (m) and α, β and γ are rotations about x, y, z axises (rad), respectively.

In Fig.2.7, the desired trajectory is inputted to inverse kinematic block which gives us six angles. Then, these angles is fed to forward kinematic block to obtain the pose of EE. This pose are supposed to be as same as desired trajectory we give to inverse kinematic equations.

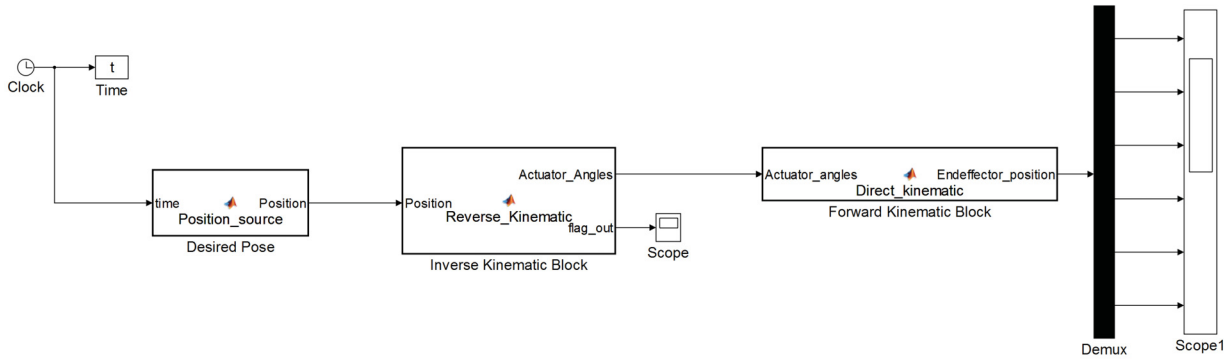

Figure 2.7: Kinematics model

Fig2.8-Fig2.13 show the desired trajectory and the calculated pose by forward kinematics. Comparing desired pose with the pose which is obtained by FK model, it proves that IK and FK model have an agreement with each other.

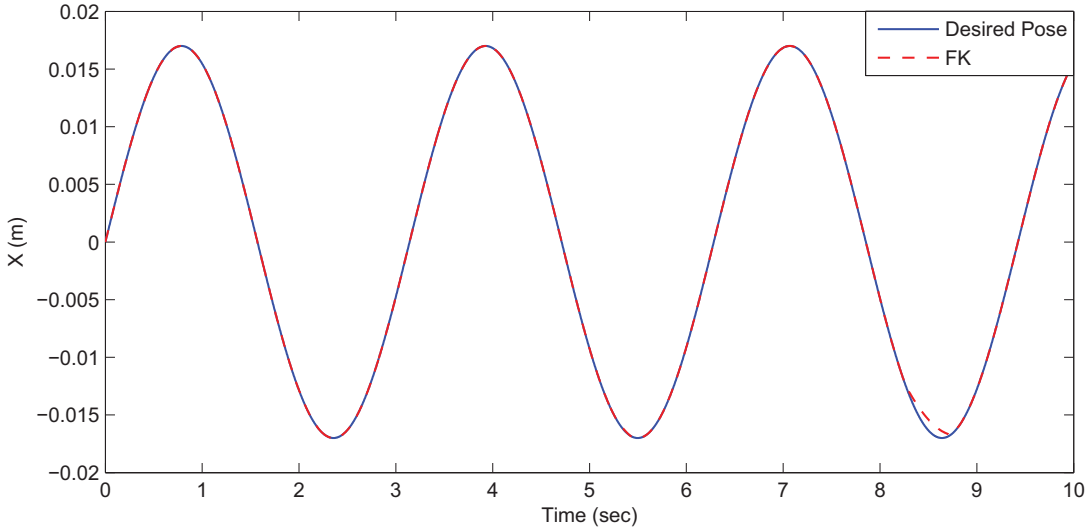

Figure 2.8: Sinusoidal Response for Pose of EE along X direction

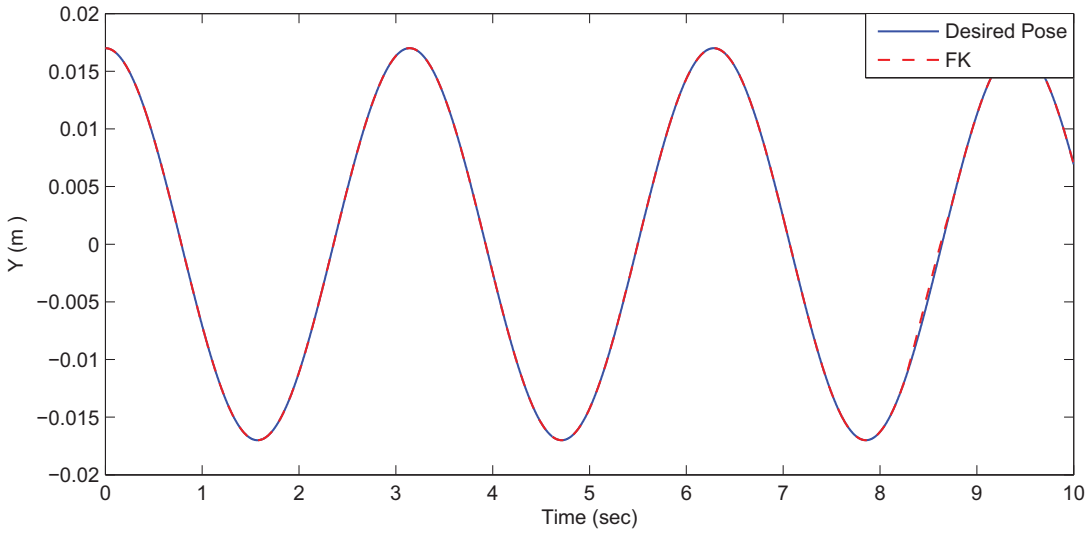

Figure 2.9: Cosinusoidal response for pose of EE along Y direction

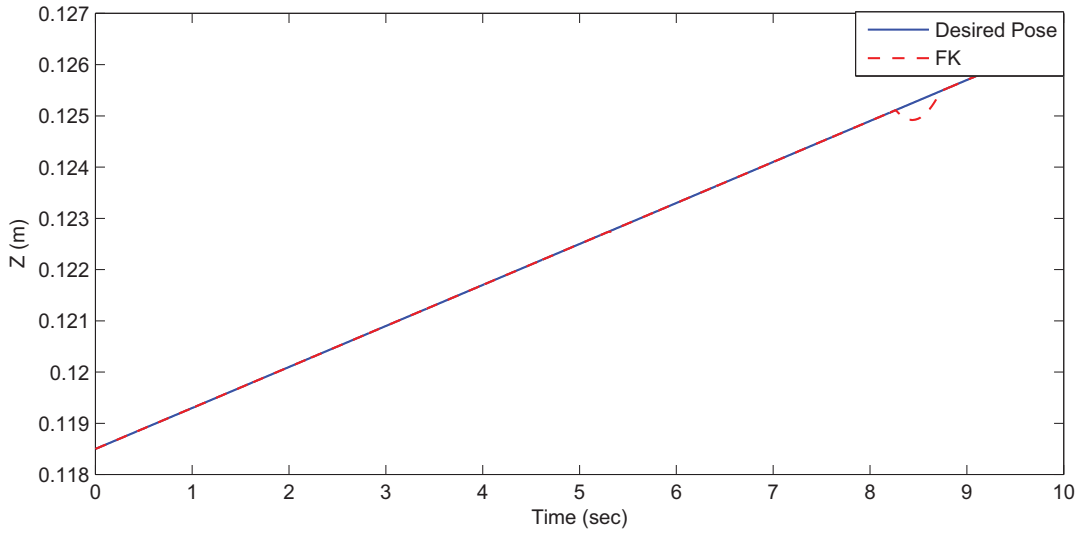

Figure 2.10: Ramp response for pose of EE along Z direction

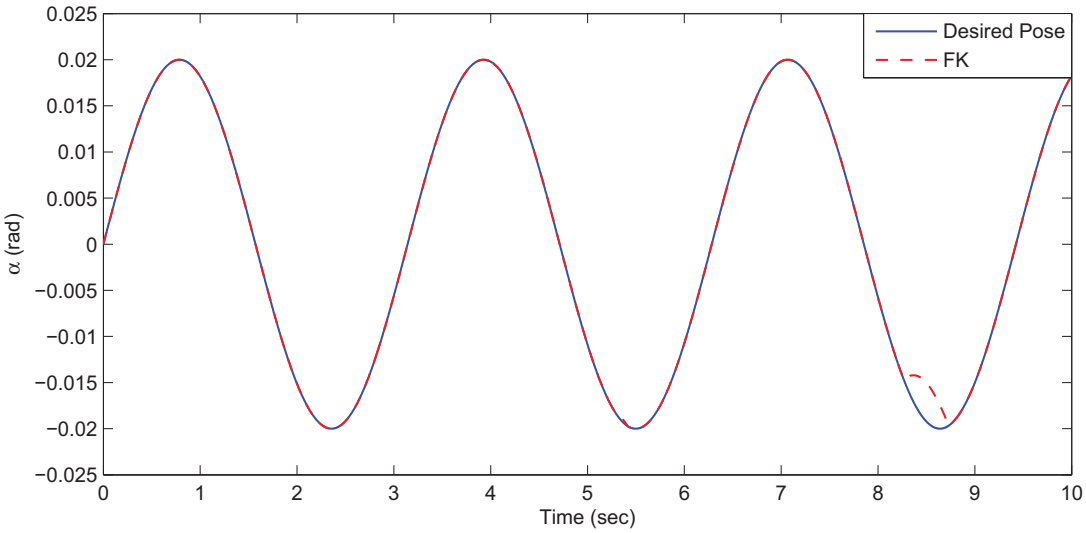

Figure 2.11: Sinusoidal response for pose of EE about X direction (α)

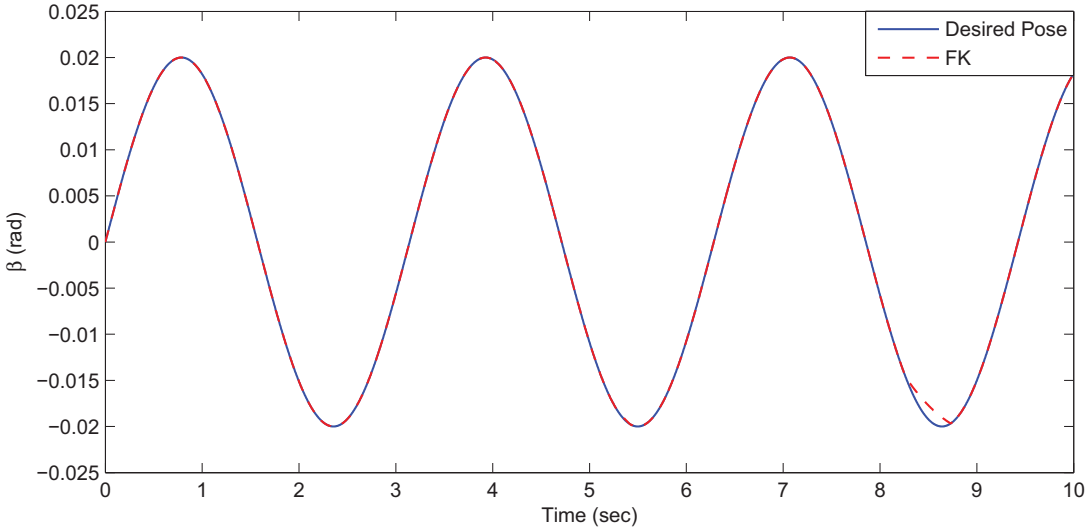

Figure 2.12: Sinusoidal response for pose of EE about Y direction (β)

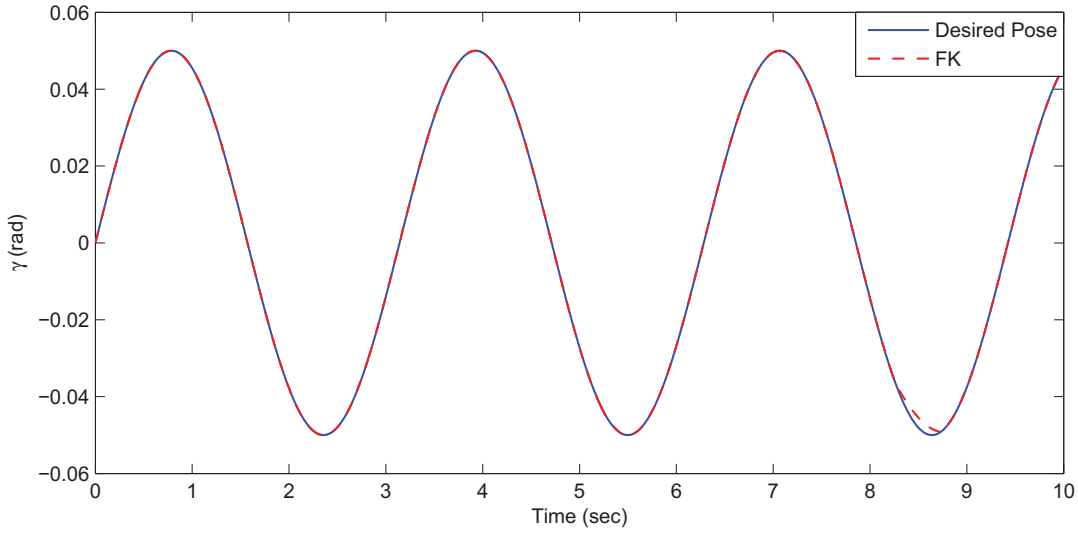

Figure 2.13: Sinusoidal response for pose of EE about Z direction (γ)

2.3 Summary

In this Chapter, a 6-RSS parallel robot has been introduced. At first, a review of all parallel robots has been presented. Then, 6-RSS parallel robot, available in lab, is mainly discussed and both the inverse and forward kinematics of robot have been derived and simulated. Simulation results show

that forward kinematics and inverse kinematic model are agreed with each other.

Chapter 3

Modeling of Actuators

Having acquiring the knowledge about the kinematics of 6-RSS parallel robot, we want to investigate the dynamic behavior of the actuators. Six actuators consist of six brush-less DC motors. Inverse kinematic block gives a desired set of angles ($\theta_1, \theta_2, ...\theta_6$) corresponding to a specific pose. These angles are input to the actuators ($Motor_1, Motor_2, ...Motor_6$). Then, the actuators are controlled to move to the desired angles and the current angle of each one of them (output of each motor) is obtained by potentiometer. A experimental setup is made to measure the output of actuators. These outputs are input to the forward kinematic block which mimic the motion of the parallel robot. To do so, in addition to the IK and FK models of the parallel robot, finding the parameters of each actuator's dynamic model is required. These actuators' model parameters are identified using optimization methods and the dynamic model of each actuator is built. For pose control design of the robot, the outputs of the actuators with the simulated dynamic models are compared and the identified model is validated.

The goal of this chapter is to identify the parameters of six actuators model. In this regards, a brief history of BLDC motor is discussed in Section 3.1. Then, in Section 3.2, both linear and nonlinear dynamic models of BLDC motor are represented. In Section 3.3, the experimental setup is described and the parameters of proposed linear model are identified using GA. Moreover, a nonlinear dynamic model of BLDC motor is proposed and identified using multi-objective optimization method. Finally, the identified dynamic models are verified in experiments.

3.1 History and Application of DC Motor

Generally, DC motors consist of an armature which rotates. The armature consists of three main parts: shaft, core and copper winding inserted in slots. These parts determine the main features of DC motor including bearing life, brush life, Electromagnetic Interference (EMI), and acoustical noise.

Due to the excellent speed control over acceleration and deceleration with effective and simple torque control (speed control over a wide range both above and below the rated speed), DC motor has been popularly used in industrial even though it has some crucial drawbacks as well [47]; for example:

- Replacing the brushes: Brushes should be replaced frequently because of sliding contact between commutator and brushes slides, since this contact causes wear problem.
- Producing electrical interference: Brushes and commutator have electrical contact which might cause electromagnetic interference[48]. This electrical interference makes noise. One solution is to use filter in order to remove the noise, however it cannot completely prevent to make the undesirable noise.
- Flashing: This electrical interference between commutator and brushes causes DC motor sparks which is dangerous in corrosive conditions.
- High initial cost: For better communication, the winding inductance is to be kept at a minimum. Increasing the number of armature coils is the solution to improve the communication for the conventional DC motors. Considering the cost, this solution is not a practical. Instead of this, the moving-coil version of the DC motor is the same as the toothless version of the brushless motor which has low inductance, low electrical time constant, and minimum magnetic drag.

In order to avoid these deficits, another type of DC motor has been invented which is called brushless DC motor (BLDC). The DC motor is replaced by BLDC motor which has the similar features in comparison with conventional DC motor, except it does not have brushes and commutator part. Because the brushes not only need regular maintenance, but also introduce wear problems

which impose sparking, undesirable noise and speed limitations.

The BLDC motor usually consist of a permanent magnet rotor which rotates about armatures, a number of fixed stator windings around the rotor, entire sensing system, and electronic switching circuits. This new structure increases the torque speed in comparison with conventional DC motor[49].

The field flux is supplied by the permanent magnets which are mounted on the rotor and are arranged in pole pairs. The stator is designed in such a way that if the current reaches the coils at a right time, the interaction with the field flux occurs and toque is produced. An absolute sensing system is required to locate magnets which is necessary for the coil to be switched in the correct sequence and at a correct time. The electronic commutator takes the information from the sensors and processes it to switch the currents in the stator coils.

Generally, it has many advantages such as simple maintenance, low price and reliability. Also, they are easy to be constructed [50]. BLDC motor provides variable speed operation. These motors are used in high performance motion control products, such as machine tools. These advantages make an increase in interest in the use of this kind of motor [51].

The DC motor has been widely used in industry because of the excellent speed control over acceleration and deceleration with effective and simple torque control (speed control over a wide range both above and below the rated speed) [52].

The classical model of DC motor is a linear second-order equation one which is discussed in following section.

3.2 Dynamic Modeling

As it is mentioned before, BLDC motors are usually utilized in industrial applications due to the stable and straight forward characteristics associated with them [53]. As a result, finding the dynamic model for DC motor has attracted many researchers' attention and methods have been proposed. In this section linear BLDC motor model is adopted and identified by using GA. The linear model neglects the effect of friction. As a result, a nonlinear BLDC motor model is presented and identified using multi-objective optimization method in Section 3.3.

3.2.1 Linear Model

In general, the torque generated by a DC motor is proportional to the armature current and the strength of magnetic field [54]. The magnetic field is assumed to be constant. Therefore, the motor torque is proportional to only the armature current i by a constant factor K_t as shown in the equation below,

$$T = K_t i \tag{3.1}$$

the back emf, e, is proportional to the angular velocity of the shaft by an electromotive force constant K_e.

$$e = K_e \dot{\theta} \tag{3.2}$$

In SI units, the motor torque and back emf constants are equal, therefore, $K_t = K_e = K$. Based on Newtons second law and Kirchhoff's voltage law, the following equations are derived,

$$J\ddot{\theta} + b\dot{\theta} = Ki \tag{3.3}$$

$$L_a \frac{di}{dt} + R_a i = V - K_e \dot{\theta} \tag{3.4}$$

where, J is the moment of inertia of the rotor ($Kg.m^2$), b is the motor viscous friction constant ($N.m.s$), L_a is electric inductance (H), R_a is the electric resistance (Ohm).

Applying the Laplace transform, the above modeling equations can be explained in terms of the Laplace variables.

$$J(s^2)\Theta + bs\Theta = KI \tag{3.5}$$

$$LsI + RI = V - Ks\Theta \tag{3.6}$$

$$I = \frac{(V - Ks\Theta)}{(Ls + R)} \tag{3.7}$$

$$\tag{3.8}$$

By eliminating I(s) between two above equations, the transfer function of DC motor is obtained as follows:

$$Js^2\Theta + bs\Theta = K\frac{V - Ks\Theta}{Ls + R} \tag{3.9}$$

$$\Theta(Js^2 + bs)(Ls + R) = KV - K^2 s\theta \tag{3.10}$$

$$KV = \Theta(JLs^3 + JRs^2 + bLs^2 + bRs) + K^2 s\Theta \tag{3.11}$$

So, the transfer function of DC motor obtained as follows:

$$\frac{\Theta}{V} = \frac{K}{JLs^3 + (JR + bL)s^2 + (bR + K^2)s} \tag{3.12}$$

where, $R = Ra$ is armature resistance, (Ω), $L = La$ is armature inductance, (H), v is Armature voltage, (V), $e(t)$ is back emf voltage, (V), Kb is back emf constant, ($V/(rad/sec)$), $K = K_t$ is torque constant, ($N.m/A$), T_m is torque developed by the motor, ($N.m$), $\Theta(t)$ is angular displacement of shaft, (rad), J is moment of inertia of motor and load, (Kg-m^2/rad), and b is motor viscous friction constant, (N.m.s).

The linear model neglects nonlinear friction which causes negative effects on the systems performance. The nonlinear friction models and their identification for DC motor will be built and identified in following section [20], [3], [55], [53].

3.2.2 Nonlinear Model

As it is mentioned, before the linear DC motor model neglects the dead zone of motor that has a great effect on the system of motor [3]. In order to improve the accuracy of the model, the effect of nonlinear friction is considered in DC modeling. Considering the nonlinear friction model, the friction torque applied to the system results in the DC motor model which becomes a second-order nonlinear model.

An equivalent electrical circuit of BLDC is represented in Fig.3.1.

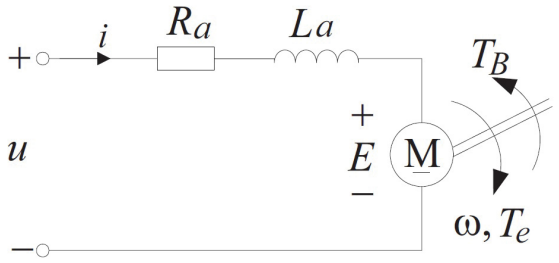

Figure 3.1: Equivalent electrical circuit of a DC brushless motor [3].

The torque balance equation of DC motor can be described as follows,

$$J\dot{\omega} + B\omega = K_t i \tag{3.13}$$

where, J is the inertia moment of the rotor ($kg.m^2$), K_t is the torque coefficient of DC motor ($N.m/A$), and B is viscous friction coefficient of DC motor ($N.m.s/rad$). The linear DC motor is given by,

$$J\dot{\omega} + B\omega = K_t i \tag{3.14}$$

$$L_a \mathrm{i} = V - K_e\omega - R_a \mathrm{i} \tag{3.15}$$

$$y = \omega \tag{3.16}$$

Consider the torque introduced by the friction,

$$B\omega + J\dot{\omega} + T_c sgn(\omega) = K_t i - f(\omega) \tag{3.17}$$

$$L_a \mathrm{i} = V - K_e\omega - R_a \mathrm{i} \tag{3.18}$$

$$y = \omega \tag{3.19}$$

where, $f(\omega)$ is friction and could be defined as,

$$f(\omega) = (T_s - T_c)exp(-\alpha.|\omega|)sign(\omega) \tag{3.20}$$

where, T_c is the Coulomb friction torque ($N.m$), T_s is static friction torque $(N.m)$, α is time constant, ω is the angular velocity of the actuator (rad/s).

By dividing both sides of the equation (3.17) by J, and also both sides of the Eq.(3.18) by L_a, Eqs. (3.21) and (3.22) could be rewritten as,

$$\begin{aligned}\dot{\omega} = -K_1\omega - K_2 sgn(\omega) - K_3 exp(-K_4|\omega|)sgn(\omega) \\ +K_5 i\end{aligned} \tag{3.21}$$

$$\mathrm{i} = K_6 V - K_7\omega - K_8 \mathrm{i} \tag{3.22}$$

$$y = \omega \tag{3.23}$$

where, $K_1 = B/J, K_2 = K_t/J, K_3 = R_a/L_a, K_4 = K_e/L_a, K_5 = 1/L_a, K_6 = T_c/J, K_7 = (T_s - T_c)/J, K_8 = \alpha$, $\vec{K} = [K_1, K_2, K_3, K_4, K_5, K_6, K_7, K_8]^T$ is the parameter vector that contains eight parameters. In next few sections, these parameters are identified by multi-objective optimization using GA.

In the following section, the identification of both linear and nonlinear DC motor models are discussed.

3.3 Parameters' Identification

In order to achieve the collaboration operation between parallel robot and AFP machines, obtaining the exact pose of 6-RSS parallel robot is necessary. To achieve this, a proper dynamic model of each actuator is required. There are plenty of identification methods to obtain the parameters of actuators. Among all of them, GA is employed in this work study to identify the DC motor model's parameters.

The aim of Section 3.3.1 is to identify the dynamic model of linear DC motor without considering effect of friction. First, an experimental setup is built to measure the output of each actuator. Then, GA is used to identify the parameters of linear DC motor model.

In the Section 3.3.2, to obtain the parameters of nonlinear DC motor, GA was applied first; but the result was not satisfactory. It was due to the nonlinear friction which is not considered in the linear model. Using only GA to optimize just one objective function for parameter identification, cannot find the nominal parameters. Usually, there is not one objective but there are several ones which should be optimized, i.e. costs, time, reliability and performance [56]. In fact, these objectives are sometimes even in conflict with each other. These problems can be considered as multi-objective problems (MOPs). Accordingly, multi-objective optimization method is used to find trade-offs among objectives [57]. GA is one of the most efficient means to solve MOPs, due to its unity and universal aspects. In order to solve this problem, multi-objective method is applied to optimize two objective functions for the nonlinear model identification at the same time.

3.3.1 Parameters' Identification Using Genetic Algorithm

The history of GA dates back to 1970s where John Holland introduced and developed the GA based evolutionary ideas of natural selection [58].

In this method, the population of the candidate solution is evolved towards a better solution. The procedure is listed as follows:

1. A random population of chromosomes is generated.
2. Then the fitness of each chromosome is evaluated.
3. New population is created based on selection, crossover and mutation.
4. Finally the old population is replaced by new generated population. The goodness of solution is typically defined with respect to the current population [59].

GA has its advantages, for example: Every optimization problem could be solved in which the chromosomes encoding can be described. Also the problem with multiple solutions could be solved by GA. Moreover, multidimensional, non-differential, non-continuous and even non-parametrical problems can be solved since this method is not dependent on the error surface [59].

Besides its advantages, there are several disadvantages as well [60]. There is no absolute insurance that the global optimum will be found. It happens very often when the populations have a lot of subjects. Like other artificial intelligence techniques, the genetic algorithm cannot assure the constant optimization response time. Due to this property, the usage of GA will be limited in real time application. In this section, GA is applied to find the optimized parameters of the dynamic model of the DC actuators. To collect the data for identification we have retrofitted the controller of the parallel robot with two Quanser Cards.

The identification procedure is shown as follows:

1. First, an experimental set up is built to measure the angles of the Stewart's (the robot) motors. Fig.3.2 is the set up for our experiment work:

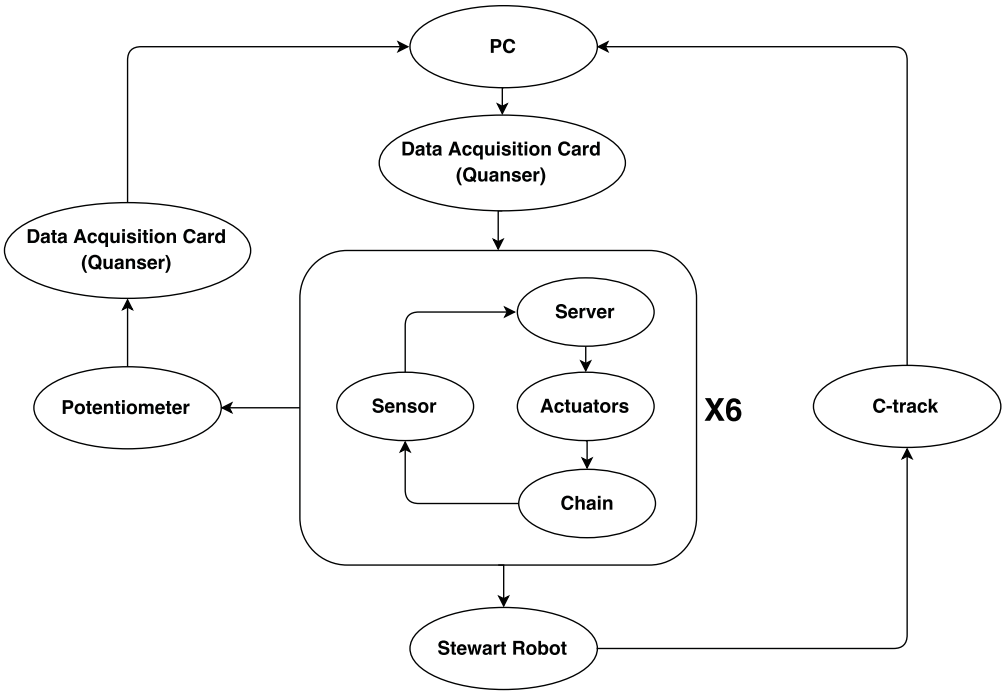

Figure 3.2: Experimental set up for parallel robot

As it is shown, there is a computer which is connected to the parallel robot. It uses two data acquisition cards (Quancer cards) to transfer the data. A Simulink file (Fig.3.3) in matlab has been made in which the voltage is given as an input and the angles of each actuator is received as an output. One of the Quanser card is used to send the voltage to the 6 actuators. Each time the program is running, the power is applied to the actuators and let both actuators and robot move. Then, a potentiometer is used to measure the angle of each actuator. Using the second Quanser card, the measured data from potentiometer is sent to computer.

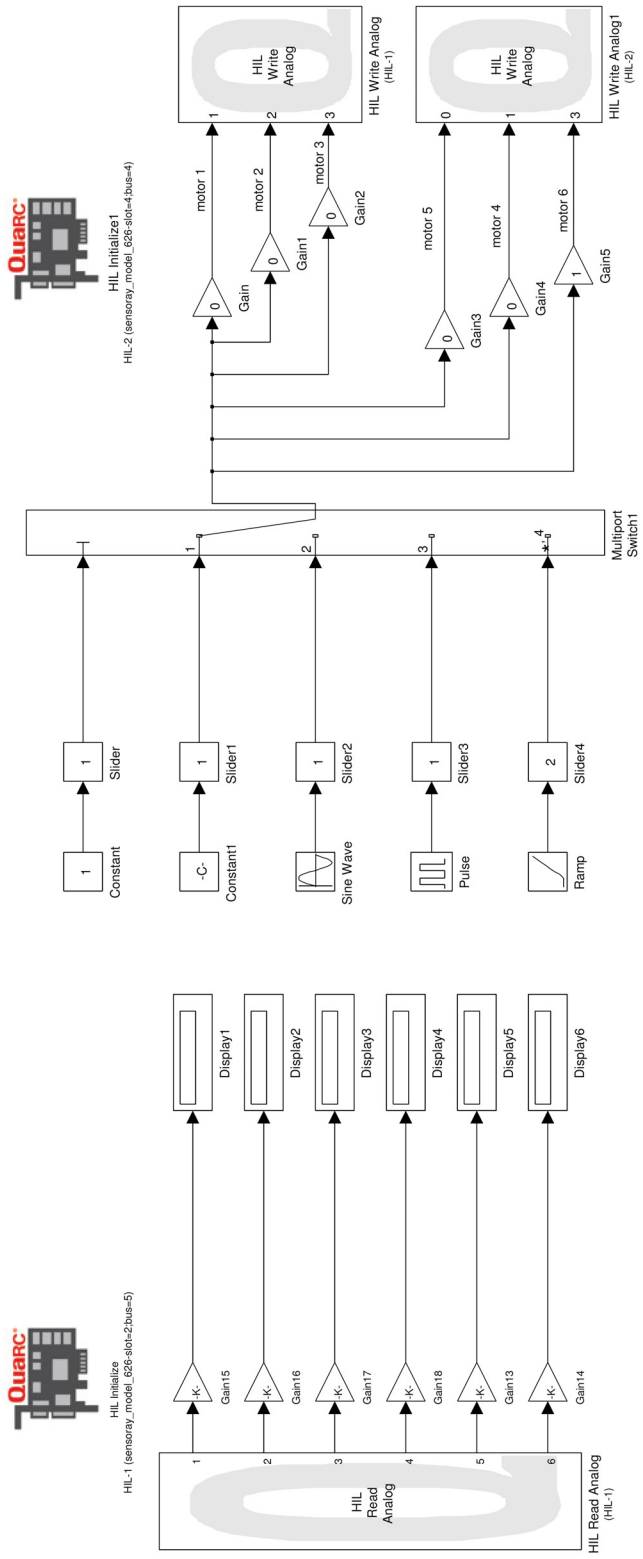

Figure 3.3: Using two Quanser cards to give the output and get the input

2. One input is given to actuator. Then the output of motor is measured. At the same time, a dynamic model of DC motor is modeled and simulated with initial hypothetical parameters, the same input is given to this dynamic model.

3. By comparing the output results with the simulated one, the error is obtained. The norm of error is known as a cost function which should be minimized. In other word, a cost function is defined based on the norm of error between the experimental output and one that is obtained from the dynamic model.

4. Using GA optimization method, this cost function is minimized and the parameters of DC motor are identified. The parameters of the built-in PD controller are optimized through an evolving process using the Genetic Algorithm simultaneously.

For identification purpose, we have chosen pulse input signals. It is observed that the output of identified dynamic model is in agreement with that of experimental set up in Fig.3.6-3.11. The experimental results show that the proposed method can find the fitting parameters of both the dynamics model of actuators.

The control signal of PD controller has the following form:

$$u(t) = K_p e(t) + K_d(d_e/d_t) \tag{3.24}$$

where u is the control signal, e(t) is tracking error, K_p and K_d are proportional and derivative gain, respectively.

The following objective function should be minimized:

$$J = ||\vec{e}||_2 = J_1 = ||\theta_r - \theta_a||_2 \tag{3.25}$$

where $\vec{e}$ is the error between experimental pulse response (θ_r) and simulated one (θ_a). Similarly, the other errors can be defined.

Using mutation with the value of 0.01, cross over with the value of 0.6 and initial population with the value of 200, the parameters is obtained. The GA has been carried out by $MATLAB$ optimization toolbox.

3.3.1.1 Linear Model Identification Results

Table.3.1shows the identified parameters using GA.

Table 3.1: Identified Parameters of Linear BLDC Motor Using GA

K_t	K_e	J	b	L_a	R_a	K_p	K_d
0.93930	0.93930	0.00619	0.15977	0.73001	0.00689	8.46373	0.86471

Then, transfer function of linear BLDC motor could be rewritten as follows,

$$\frac{\Theta}{v(s)} = \frac{0.9}{0.4s^3 + (0.0004 + 0.112)s^2 + (0.00112 + 0.9^2)s} \tag{3.26}$$

Due to similar behavior of between six actuators. The average of six outputs is calculated and the parameters are obtained based on this average. In Fig.3.4, the identified dynamic model is compared with the real one. As it is shown, the error between the desired pulse response and simulated one is given as an input to PD controller. Then, the required control signal is calculated by PD controller. Finally, the angle of motor shaft is obtained and compared with the real one.

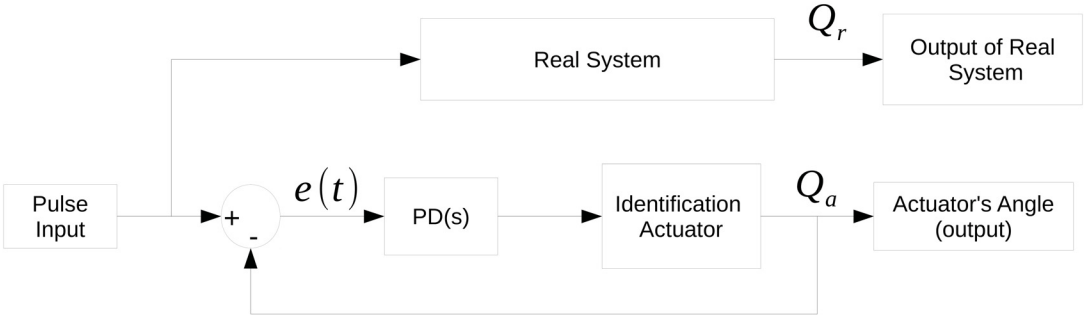

Figure 3.4: Comparing real motor model with the identified model using PD controller

Fig.3.5 shows the schematic of identified dynamic model of 6 motor controlled by PD controller.

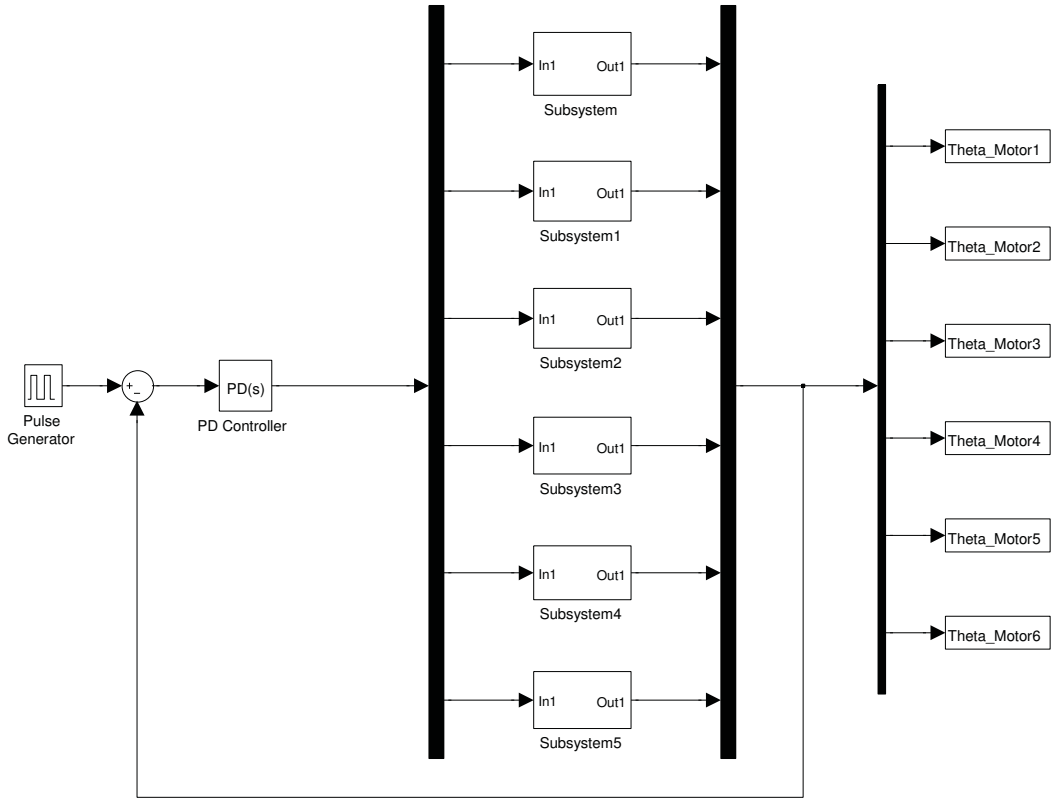

Figure 3.5: Simulink of identified motor with controller

In Figs.3.6-3.11, the output of six identified motors models are compared with those of real actuators. The maximum absolute errors are from the sixth and forth actuators, which are 6.82 and 6.52 degrees, respectively. In contrast, the minimum absolute error is from the first actuator at the value of 4.37 degree. Also, Table.3.2 shows the error between identified models and real ones. Both absolute error and Root Mean Square (RMS) error are used to calculate the error. The RMS is defined as,

$$RMS = \sqrt{\frac{\sum_1^N \epsilon^2}{N}} \tag{3.27}$$

where N is the number of data and ϵ is the discrepancy between the identified model and real one.

Overally, the identified parameters are suitable for all 6 actuators and designed PD controller has an outstanding performance for the system. As a result, identified parameters and PD controller tuned by GA method is proper for the system.

Table 3.2: Error of identified linear model

Error of Actuators (θ)	Pulse response(deg)	RMS(deg)
First Actuator	4.374	0.5389
Second Actuator	5.77	0.7834
Third Actuator	4.976	0.6865
Forth Actuator	6.52	0.9032
Fifth Actuator	5.7	0.8333
Sixth Actuator	6.82	0.9479

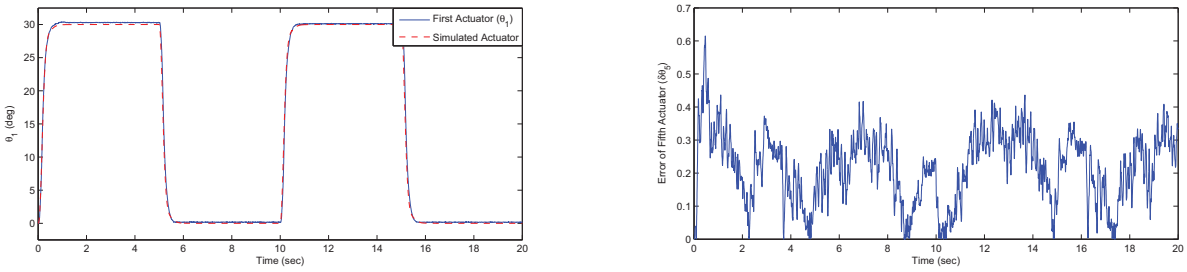

(a) Pulse response for first motor

(b) Absolute error of θ_1

Figure 3.6: Pulse response and absolute error for first motor

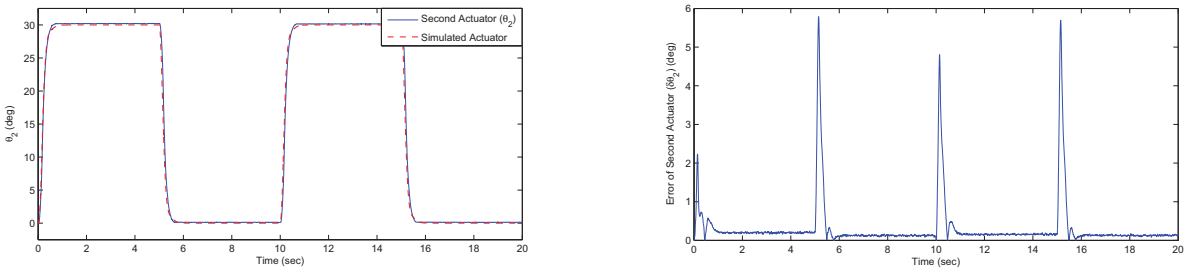

(a) Pulse response for second motor

(b) Absolute error of θ_2

Figure 3.7: Pulse response and absolute error for second motor

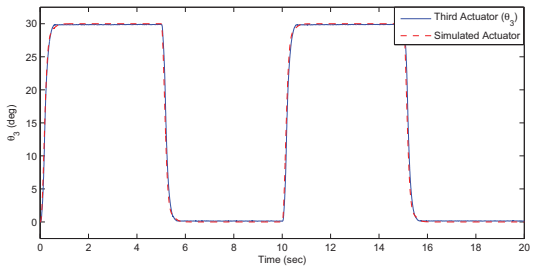

(a) Pulse response for third motor

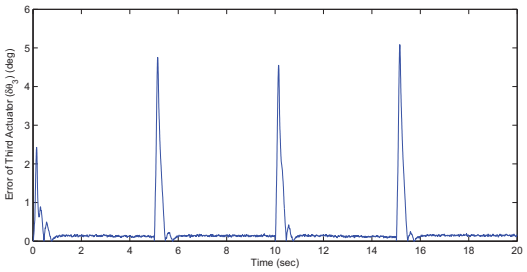

(b) Absolute error of θ_3

Figure 3.8: Pulse response and absolute error for third motor

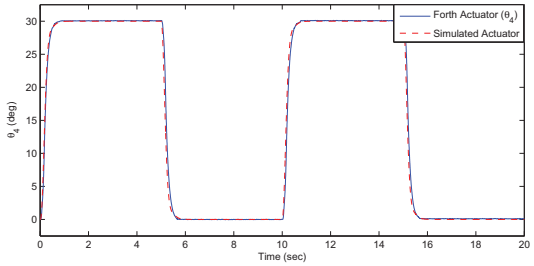

(a) Pulse response for forth motor

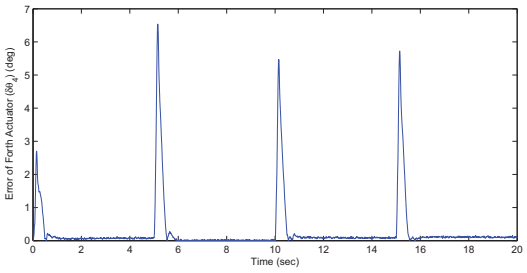

(b) Absolute error of θ_4

Figure 3.9: Pulse response and absolute error for forth motor

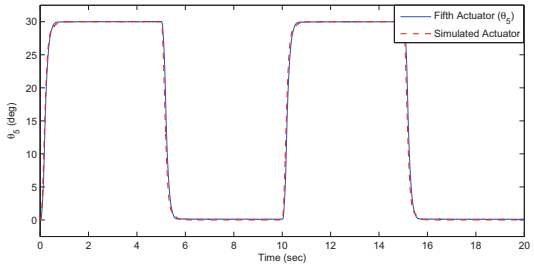

(a) Pulse response for fifth motor

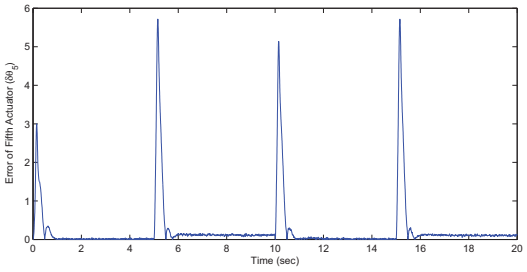

(b) Absolute error of θ_5

Figure 3.10: Pulse response and absolute error for fifth motor

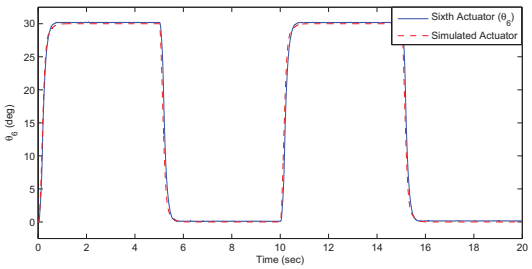

(a) Pulse response for sixth motor

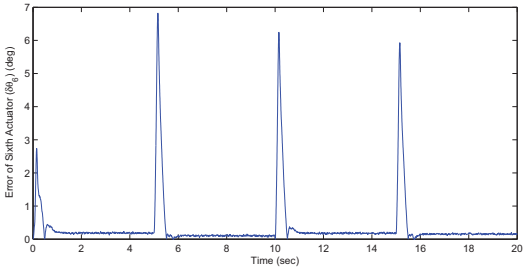

(b) Absolute error of θ_6

Figure 3.11: Pulse response and absolute error for sixth motor

3.3.2 Parameters' Identification Using Multi-objective

The purpose of this section is to identify dynamic model of DC motor considering friction effect for 6-RSS platform using multi-objective optimization.

Most of the engineering problems have more than one objective functions which should be optimized, i.e. minimizing the cost, maximizing the performance and reliability. Since, the objective functions often conflict with each other, and improving one of them may deteriorate the others[61]. A set of solutions, so called, Pareto fronts are obtained so that a reasonable set of solutions satisfying all objective functions at an acceptable level without being dominated by any other solution [62],[63].

Multi-objective optimization, also called multicriteria optimization or vector optimization has been defined as finding a vector of decision variables satisfying the constraints to give acceptable values to all objective functions[62]. In general, it can be defined as finding a set of values $[x_1^*, x_2^*, \ldots, x_n^*]$ to optimize k objectives or cost functions $[f_1(x), f_2(x), \ldots, f_k(x)]$ with giving $x = [x_1, x_2, \ldots, x_n]^T$, which is the n-dimensional decision variable vector in the solution space X.

Among many approaches, GA is the most popular one to optimize multi-objective problems [64]. GA is used to find a set of multiple non-dominated solutions in a single run. Searching different regions of solution space by GA at the same time, leads to finding various set of solutions for difficult problems with non-convex, discontinuous, and multi-modal solutions spaces.

In this work, multi-objective using GA is used to find the parameters of the model of the DC actuators. The identification procedure is shown as follows. The following two objective functions (3.27 and 3.28) are defined, which should be minimized. Two different input voltages are given to

Table 3.3: Three-objective optimization results

	K_1	K_2	K_3	K_4	K_5	K_6	K_7	K_8
A	0.998	0.350	0.030	0.741	18.827	5.547	4.933	12.447
B	0.986	0.3199	0.119	0.613	18.791	4.349	4.965	11.606
C	0.980	0.071	0.030	0.498	15.585	3.153	4.460	11.080

the DC motor. For each of them, the output of motor shaft are obtained. The obtained results are compared with the simulation ones. Using multi-objective optimization method, the error between experimental results and simulation results are minimized for input signals. Our results illustrate that the proposed method can find the proper parameters of actuator nonlinear model.

The objective functions are given as,

$$J_1 = ||\theta_e^P - \theta_s^P||_2 \tag{3.28}$$

$$J_2 = ||\theta_e^S - \theta_s^S||_2 \tag{3.29}$$

where J_1 is the norm of error between the pulse response and experimental one. Similarly, J_2 is the norm of error between the sine response and experimental one.

The evolutionary process of multi-objective optimization is performed with a population size of 250, crossover and mutation probability as 0.8 and 0.1, respectively. The multi-objective optimization has been carried out by $MATLAB$ optimization toolbox.

The Pareto fronts of J_1 and J_2 are shown in Fig.3.12 Also, the results for two-objective optimization process are shown in Table 2.

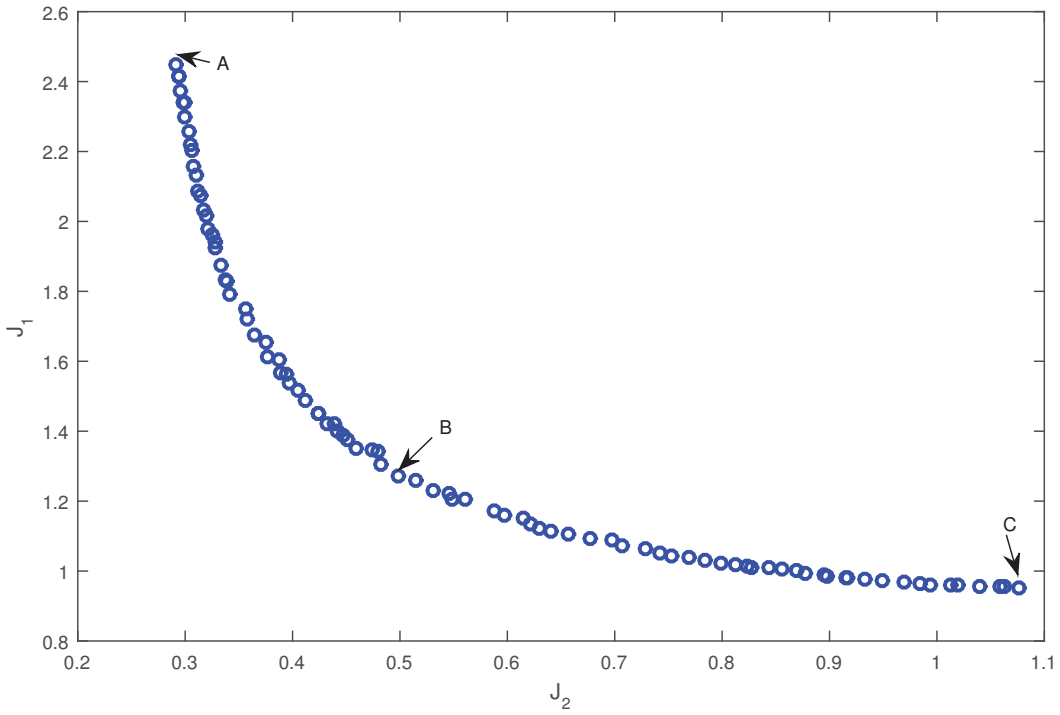

Figure 3.12: 2-norm Level diagram of Pareto front of objective functions, J_1 and J_2

Consider A, B , and C as three points on Pareto front, which have following features:

A is a point in which J_2 is minimum but J_1 has the worst value among the other values, which means that the norm of error for sinusoidal input has optimal value but for pulse input has the worst values.

At point C, although, the value of J_1 is optimal for pulse input, the norm of error for the sinusoidal input has the worst value. Therefore, C is not selected as the best point.

For point B, which is chosen as a trade off point, the values of both J_1 and J_2 are acceptable and give us a set of reasonable solutions.

As it is observed in Fig.3.12, point B is the optimal point in which the system with the $J_1 = 1.22$ can track the desired response with the small error. Furthermore, $J_2 = 0.54$ shows an excellent tracking performance and it can be considered as the best trade-off point.

Fig.3.14-3.18 show the sinusodial response of six actuators. Also, the absolute error between real motors models and identified ones are shown. The comparison between the response from the identified models and real actuator ones, shows that the maximum absolute error is from sixth

motor with the value of 0.74 degree while the minimum absolute error is from the first actuator actuator with 0.62 degree.

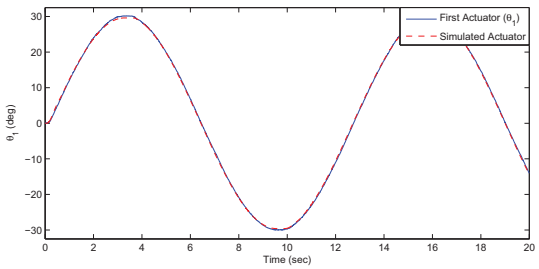

(a) Sinusoidal response

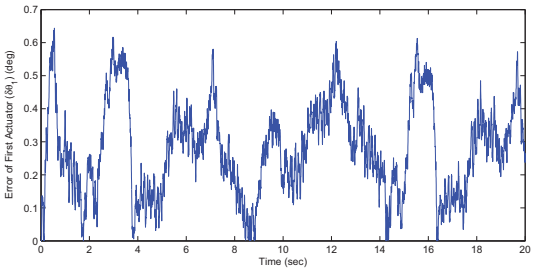

(b) Absolute error

Figure 3.13: Sinusoidal response and absolute error for first motor

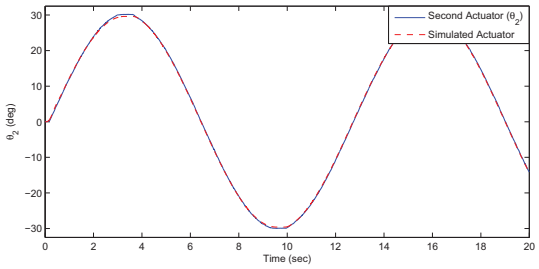

(a) Sinusoidal response

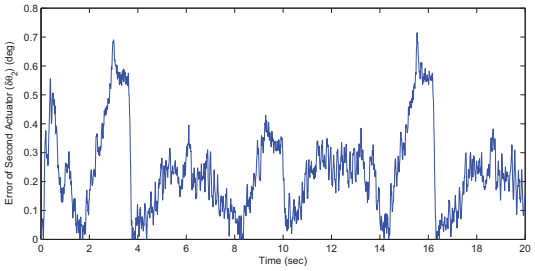

(b) Absolute error

Figure 3.14: Sinusoidal response and absolute error for second motor

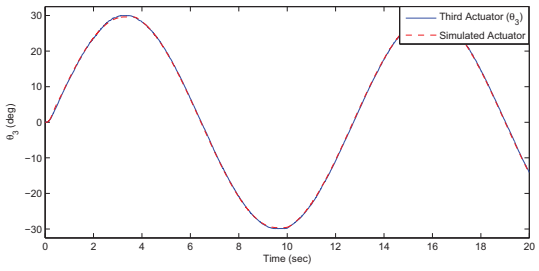

(a) Sinusoidal response

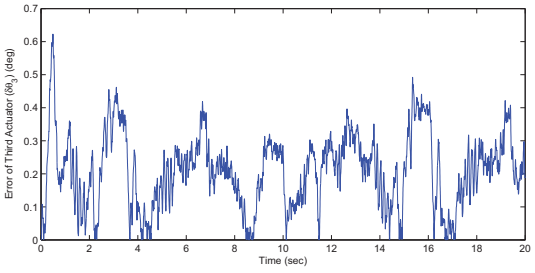

(b) Absolute error

Figure 3.15: Sinusoidal response and absolute error for third motor

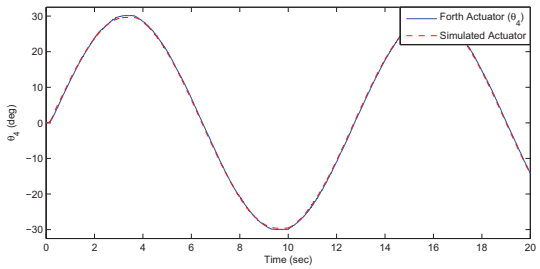

(a) Sinusoidal response

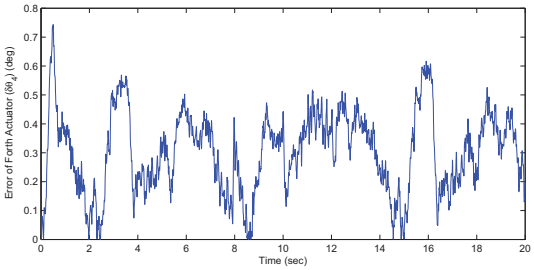

(b) Absolute error

Figure 3.16: Sinusoidal response and absolute error for forth motor

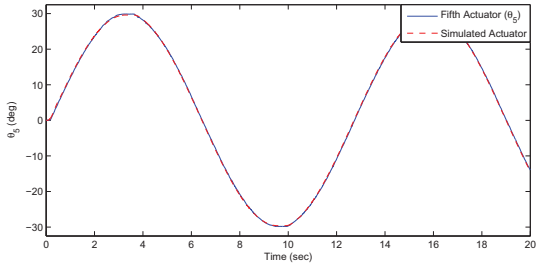

(a) Sinusoidal response

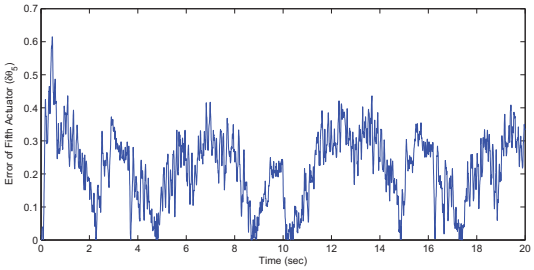

(b) Absolute error

Figure 3.17: Sinusoidal response and absolute error for fifth motor

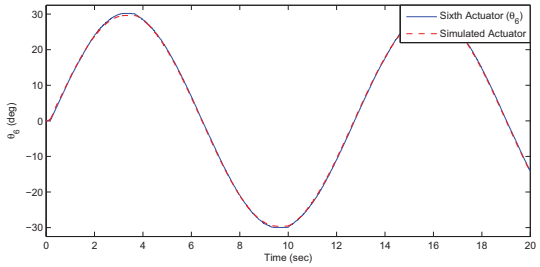

(a) Sinusoidal response

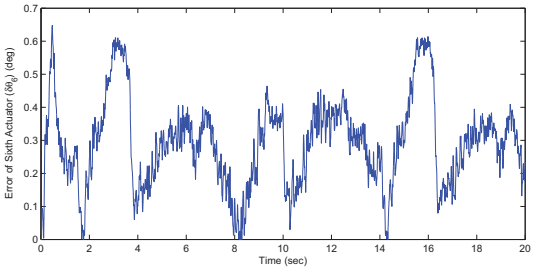

(b) Absolute error

Figure 3.18: Sinusoidal response and absolute error for sixth motor

Figs.3.19-3.24 show the pulse response of six actuators. Also, the absolute error between the response of real motors and identified ones are shown. The comparison between the responses shows that the maximum absolute error is from the sixth one with the value of 4.34 degree while the minimum absolute error is from the first actuator with 2.30 degree.

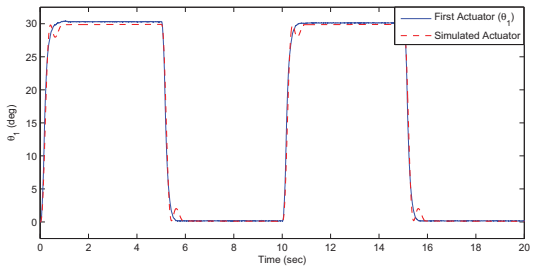

(a) Pulse response

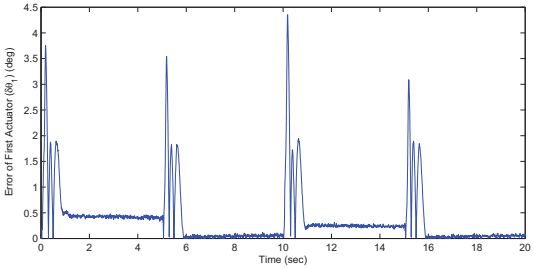

(b) Absolute error

Figure 3.19: Pulse response and absolute error for first motor

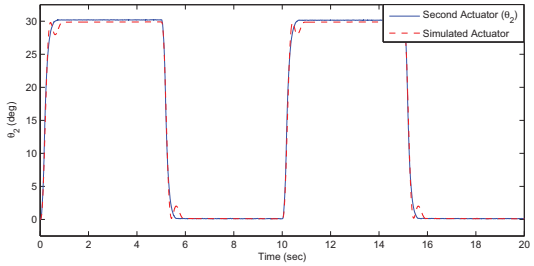

(a) Pulse response

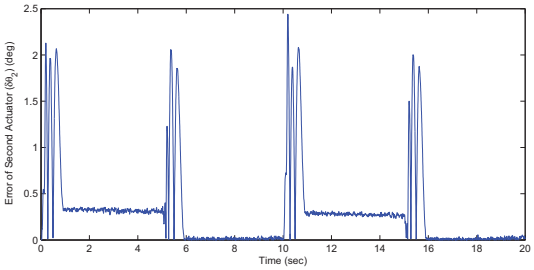

(b) Absolute error

Figure 3.20: Pulse response and absolute error for second motor

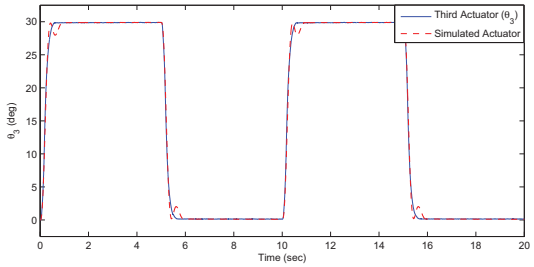

(a) Pulse response

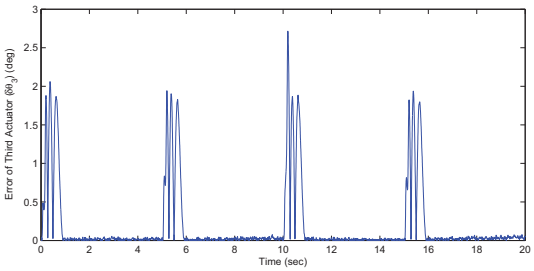

(b) Absolute error

Figure 3.21: Pulse response and absolute error for third motor

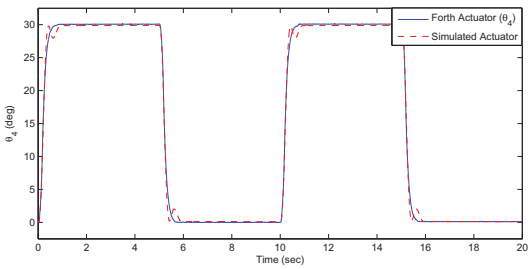

(a) Pulse response

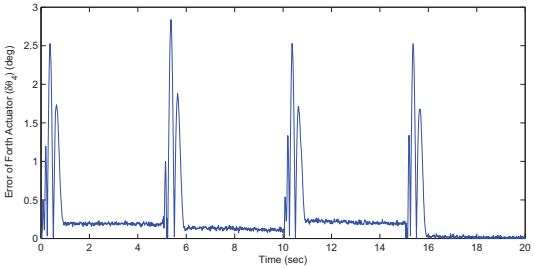

(b) Absolute error

Figure 3.22: Pulse response and absolute error for forth motor

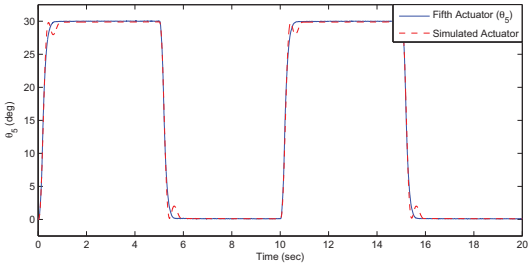

(a) Pulse response

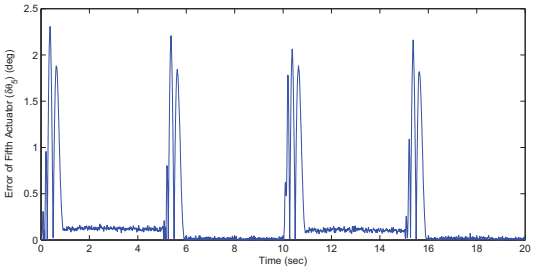

(b) Absolute error

Figure 3.23: Pulse response and absolute error for fifth motor

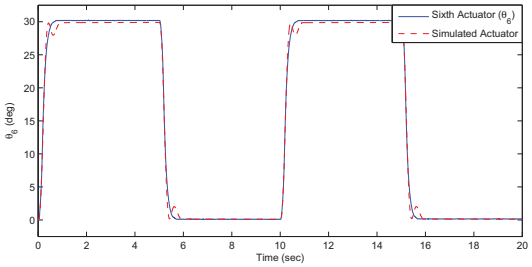

(a) Pulse response

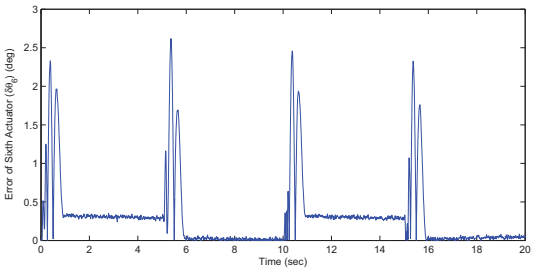

(b) Absolute error

Figure 3.24: Pulse response and absolute error for sixth motor

Table.3.4 and Table.3.5 show the error of each actuator for both pulse response and sinusoidal responses:

Overall, the identified model are accurate to represent the dynamic behavior of all 6 actuators and the designed PD controller can match the built-in controller in the six actuators' model. As a

Table 3.4: Absolute error of identified nonlinear model

	Pulse response(deg)	Sinusoidal response (deg)
First actuator	2.3	0.62
Second actuator	2.415	0.70
Third actuator	2.7	0.63
Forth actuator	2.84	0.73
Fifth actuator	2.2	0.61
Sixth actuator	4.34	0.74

Table 3.5: RMS error of identified nonlinear model

	Pulse response(deg)	Sinusoidal response (deg)
First actuator	0.7005	0.3130
Second actuator	0.5608	0.2771
Third actuator	0.5149	0.2379
Forth actuator	0.5537	0.3340
Fifth actuator	0.4997	0.2426
Sixth actuator	0.5644	0.3208

result, the identified parameters of nonlinear model tuned by multi-objective optimization method is proper for simulating actuators for the pose controller design in the next chapter.

3.4 Summary

In this chapter a brief history of DC motor has been presented. An experimental set up for parallel robot and its actuators, has been presented. Both linear and nonlinear DC motors have been proposed and modeled. The parameters of linear DC motor model have been identified using GA method. The results of the obtained dynamic model have been compared with experimental ones and proved an accurate modeling for the linear DC motors. Considering the effect of friction, the parameters of nonlinear DC motor have been identified using multi-objective optimization. The accuracy of the identified dynamic model of each actuator is validated in experiment.

Chapter 4

Pose Control

This chapter is devoted to pose control of the 6-RSS parallel robot. After obtaining IK and FK of the parallel robot and the dynamic nonlinear model of the actuators, we can simulate the parallel robot and design a pose controller in the simulation. The IK can generate the desired angles for PID pose controller from the pose error and FK is used to simulate the parallel kinematic motion and generate the pose as the feedback for pose controller.

4.1 Controlling the Pose of EE in Presence of Linear BLDC Motor Model

This section, the control pose of EE is discussed. Fig.4.1 shows the schematic of the proposed controller. As it can be seen in this figure, the error between the desired pose and the simulated one is given as an input to the inverse block. Then, $\delta\theta$ goes to the controller to obtain the control signal which is required by the actuators. In this study, the forward kinematic model is used to get a feedback from EE.

In order to control the system, a PID controller is used in this study. The design of these controllers is based on three parameters: proportional gain, integral time constant and derivative time constant. The control signal of PID controller has the following form:

$$u(t) = K_p e(t) + K_i \int e(t)d_t + K_d d(e(t)/d_t) \tag{4.1}$$

Table 4.1: PID tuned by trial and error

K_p	K_i	K_d
12	100	0.2

where u is the control signal, e(t) is tracking error, K_p, K_i, and K_d are proportional, integral, and derivative gain, respectively.

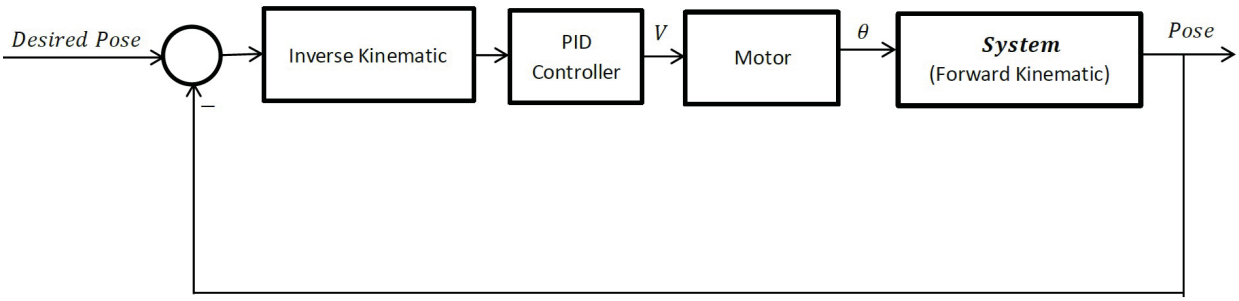

Figure 4.1: Schematic of proposed PID controller in simulation

Table.4.1 shows the gains of tuned PID controller by trial and error.

Also, the control of the pose of EE in presence of noise and disturbance are discussed. First, the open loop system is built in the Simulink block diagram in which the desired pose trajectory is given to inverse kinematics. Then, the obtained angles by the inverse kinematic model are fed to the motor model. Finally, the obtained angles from the motor are fed to the forward kinematic model and the results are compared to the desired ones (Fig.4.2).

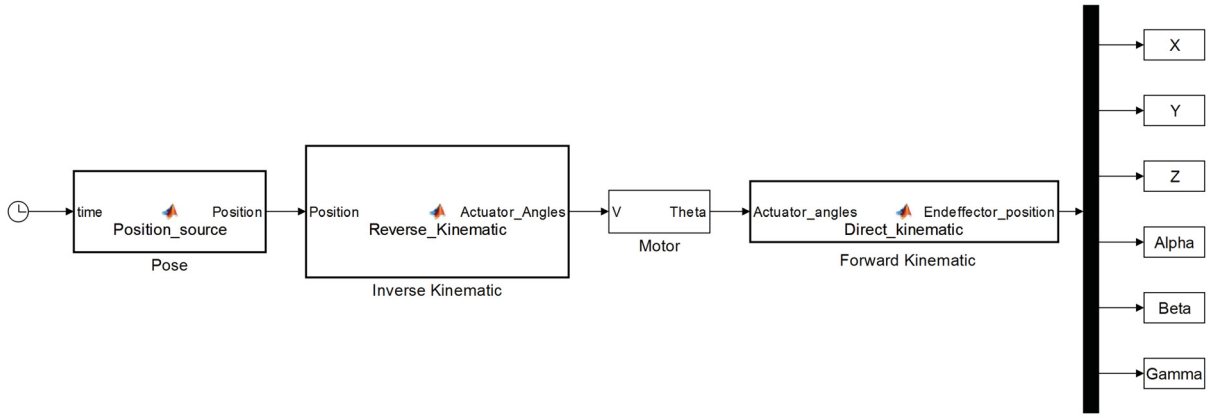

Figure 4.2: Open loop path tracking of parallel robot

In order to evaluate the performance of the controller, a desired trajectory is defined as follows:

$$x = 0.007sin(2t) \tag{4.2}$$

$$y = 0.007cos(2t) \tag{4.3}$$

$$z = 0.1185 + 0.2t/250 \tag{4.4}$$

$$\alpha = 0.02sin(2t) \tag{4.5}$$

$$\beta = 0.02sin(2t) \tag{4.6}$$

$$\gamma = 0.05sin(2t) \tag{4.7}$$

where, t is time (sec), x, y, z are the position of EE (mm) and α, β and γ are rotations about x, y, z axises (rad), respectively.

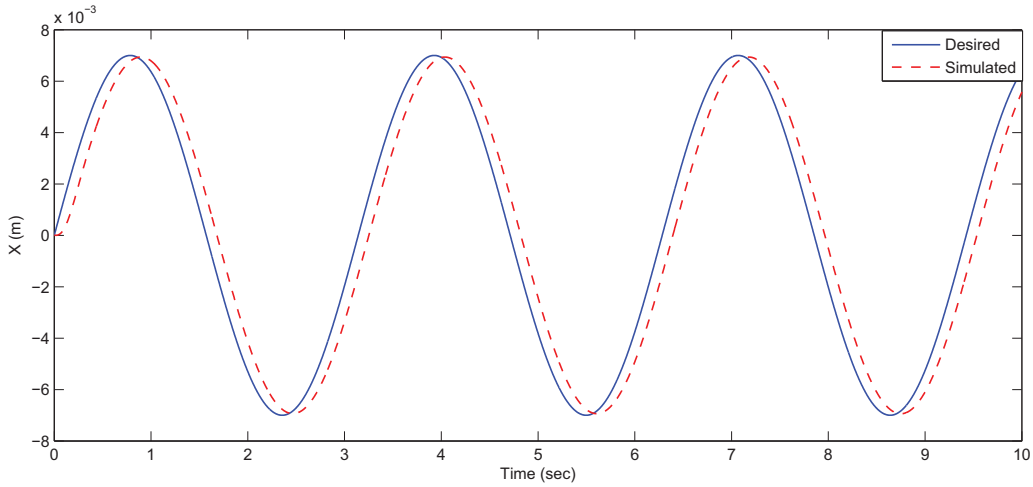

Figure 4.3: Sinusoidal response for pose of EE along X direction

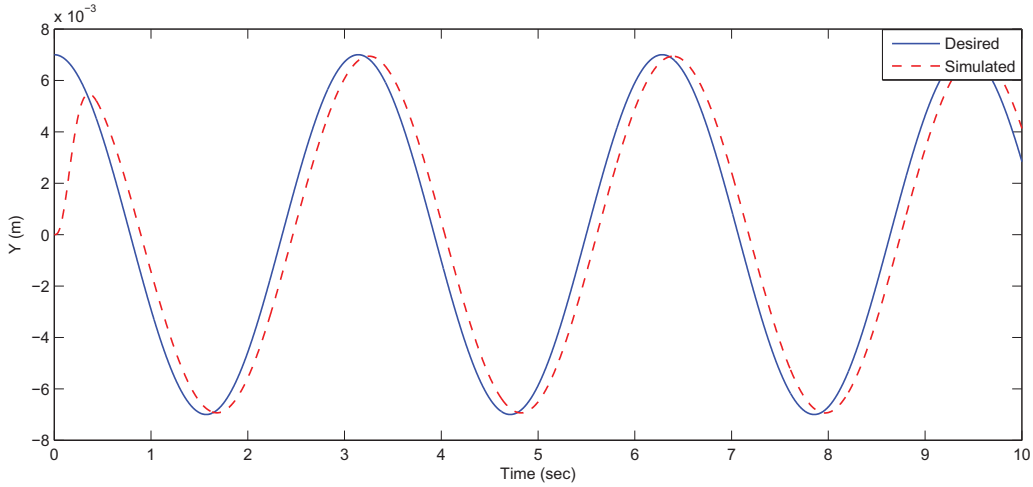

Figure 4.4: Cosinusoidal response for pose of EE along Y direction

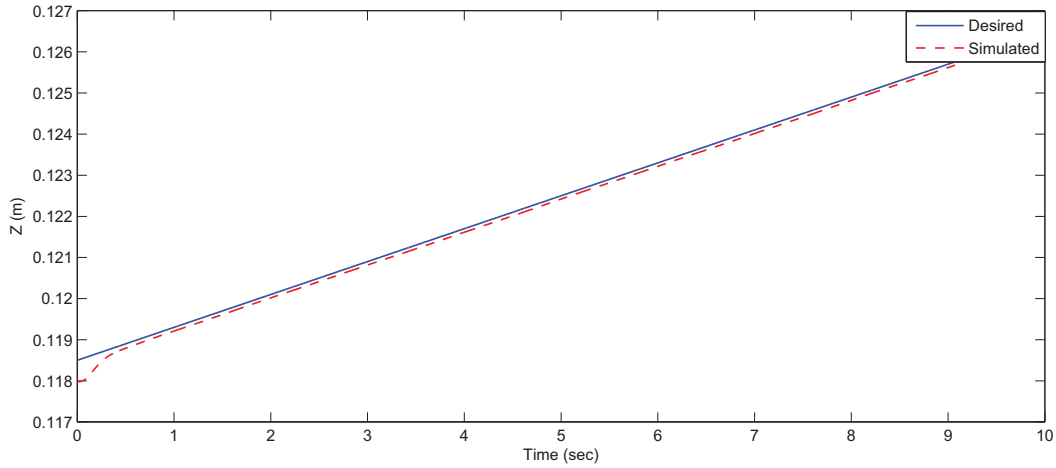

Figure 4.5: Ramp response for pose of EE along Z direction

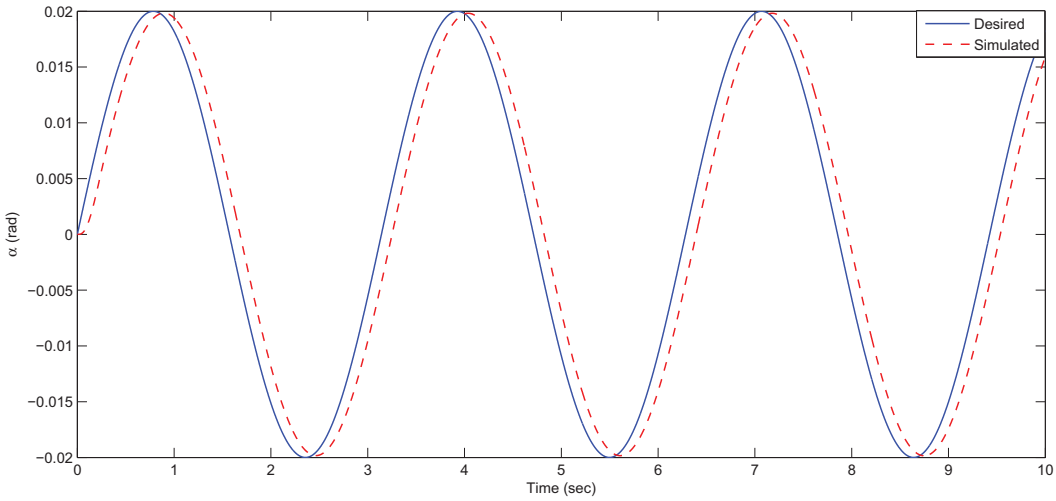

Figure 4.6: Sinusoidal response for pose of EE about X direction (α)

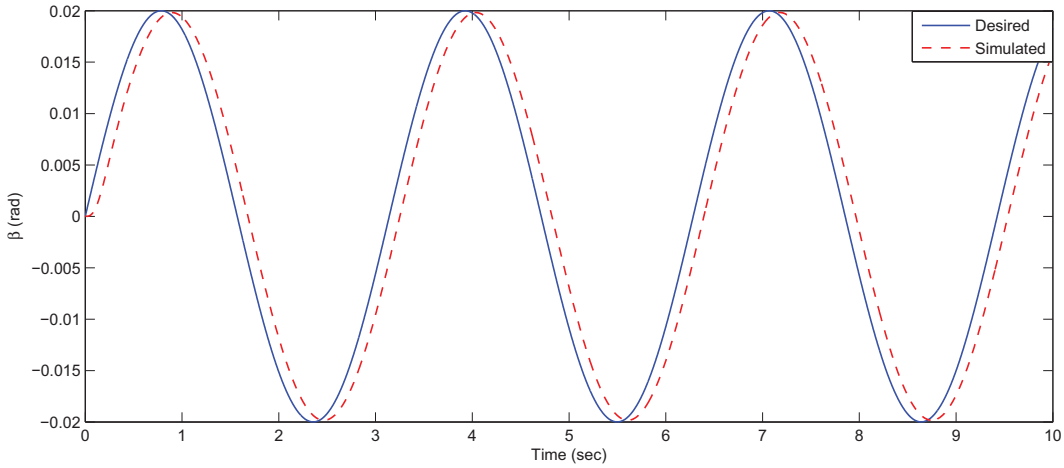

Figure 4.7: Sinusoidal response for pose of EE about Y direction (β)

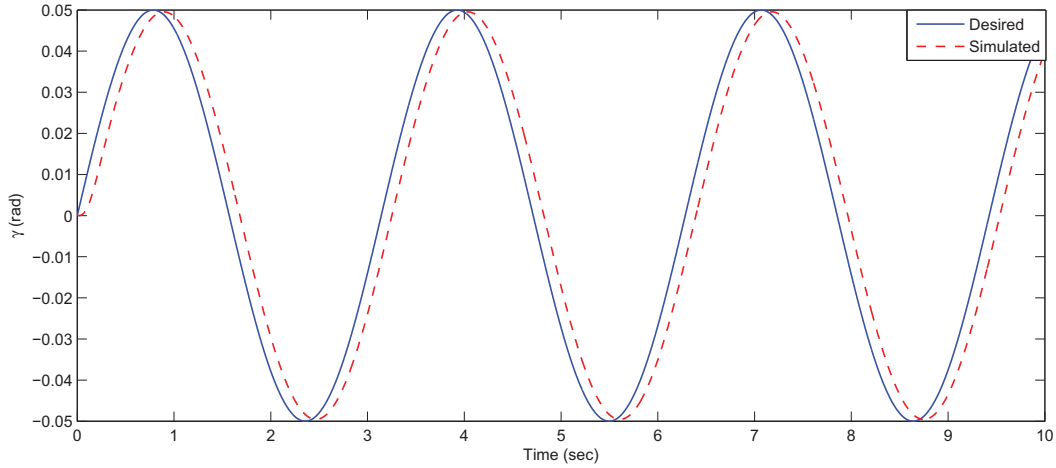

Figure 4.8: Sinusoidal response for pose of EE about Z direction (γ)

Figs.4.3-4.8 show the open loop path tracking results of the system. As it is shown in Fig.4.3 there is a time delay of 0.11sec. Although the maximum error is in z-direction with the value of 0.1 mm, the errors in x and y-directions reach to 0.5 and 0.6 mm, respectively. There are steady states errors with the value of 0.1782 radian for both α and β. Also, for γ this error reaches 0.0411 radian.

In order to reduce the error, PID controller is applied to system.

The design of these controllers is based on three parameters: proportional gain, integral time

constant and derivative time constant. The control signal of PID controller has the following form:

$$u(t) = K_p e(t) + K_i \int e(t)d_t + K_d d(e(t)/d_t) \tag{4.8}$$

where u is the control signal, e(t) is tracking error, K_p, K_i, and K_d are proportional, integral, and derivative gain, respectively.

The following Simulink block diagram shows how PID controller works. The desired path is fed to the inverse kinematic model, and then the obtained angle is subtracted from the calculated angle by Forward kinematic model. This error is input to PID controller and become regulated.

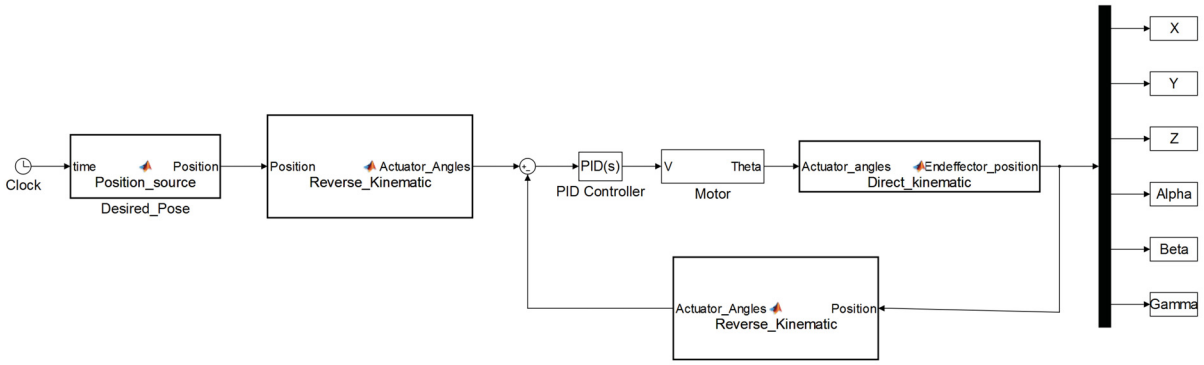

Figure 4.9: Schematic of proposed PID controller

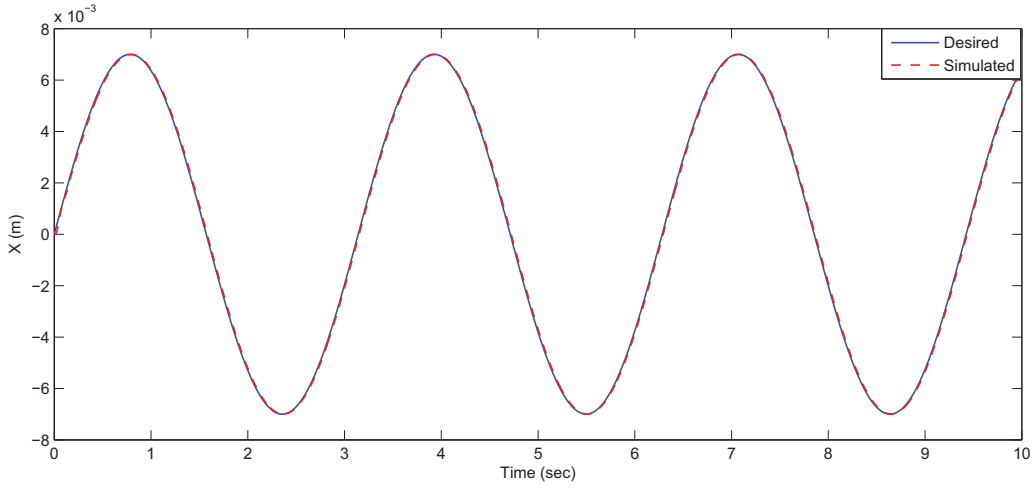

Figure 4.10: Sinusoidal response for pose of EE along X direction

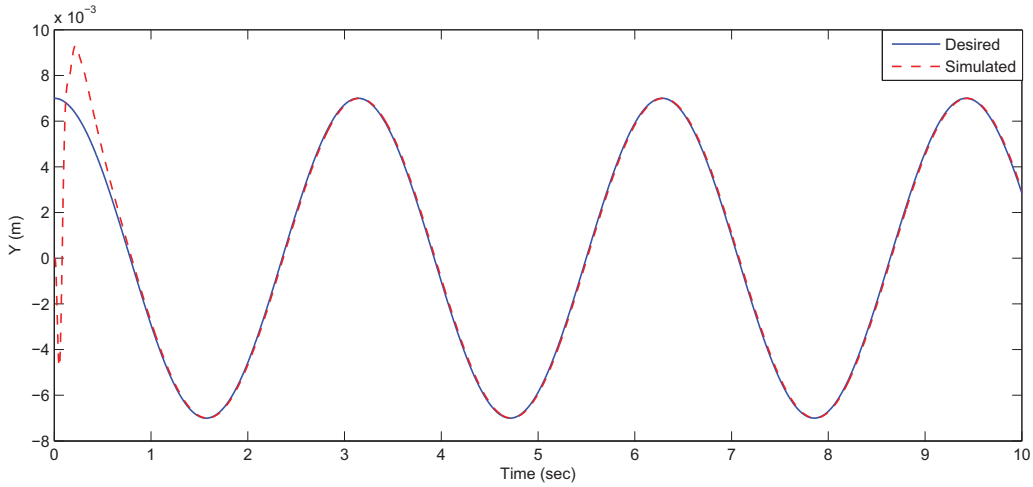

Figure 4.11: Cosinusoidal response for pose of EE along Y direction

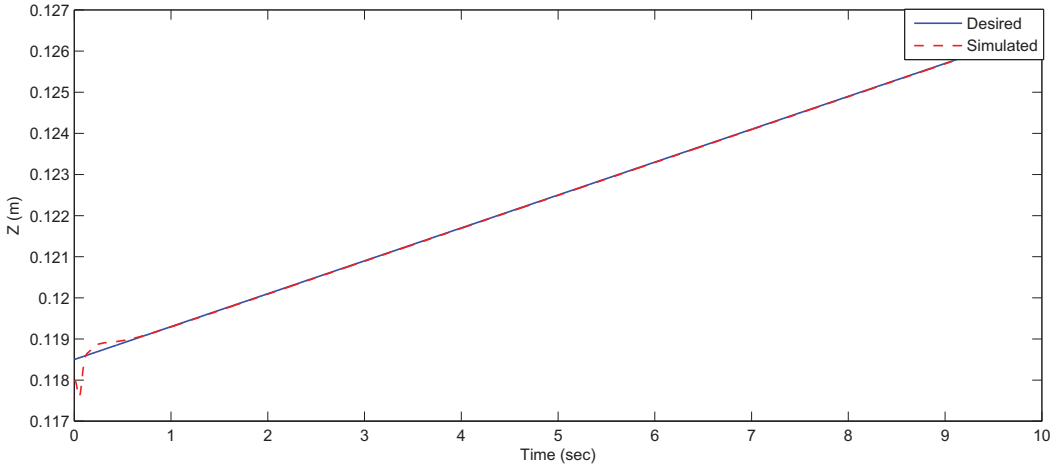

Figure 4.12: Ramp response for pose of EE along Z direction

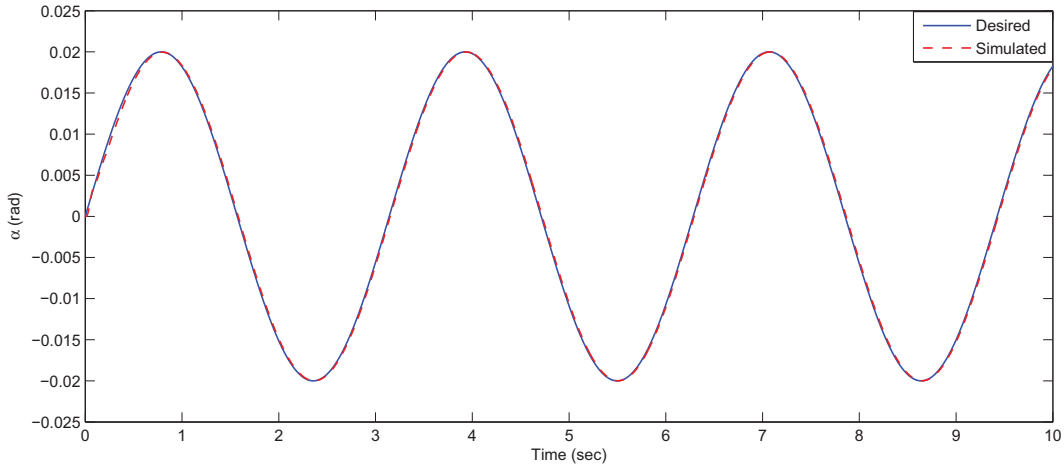

Figure 4.13: Sinusoidal response for pose of EE about X direction (α)

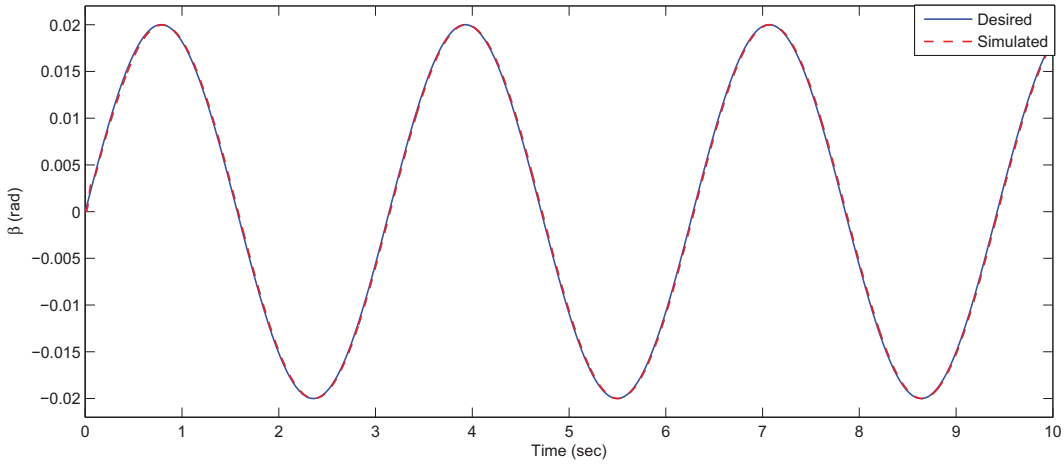

Figure 4.14: Sinusoidal response for pose of EE about Y direction (β)

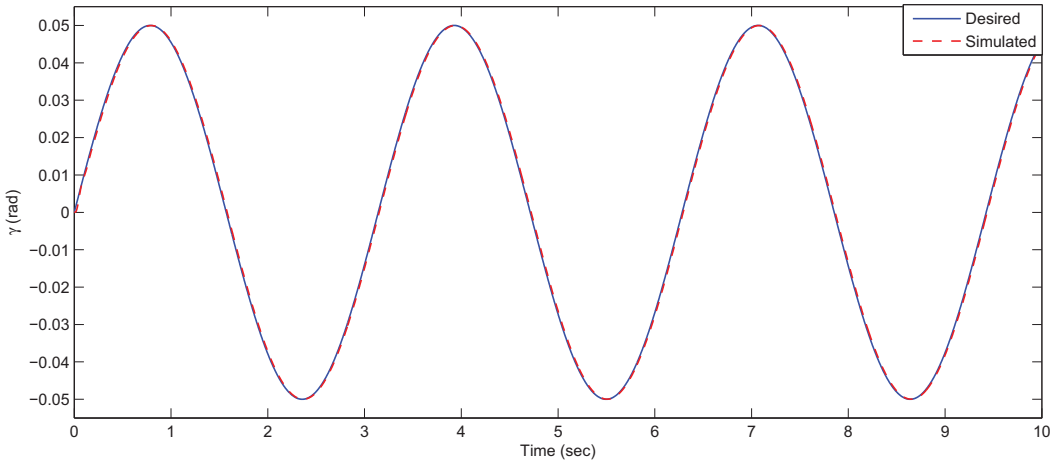

Figure 4.15: Sinusoidal response for pose of EE about Z direction (γ)

As it can be seen in Figs.4.10-4.15, the error in X and Y direction is reduced from 0.5 and 0.6 mm to 0.32. The value of error in z-direction is incredibly diminished to zero. Also, for α, β and γ, the controller has a satisfactory path tracking.

In order to see the performance of the controller in presence of noise, a random noise with the variance value of 0.5 is applied to 3-translation axis and 3-rotations axis. Fig. 4.16 shows the Simulink block digram is made in order to track the path in presence of the noise.

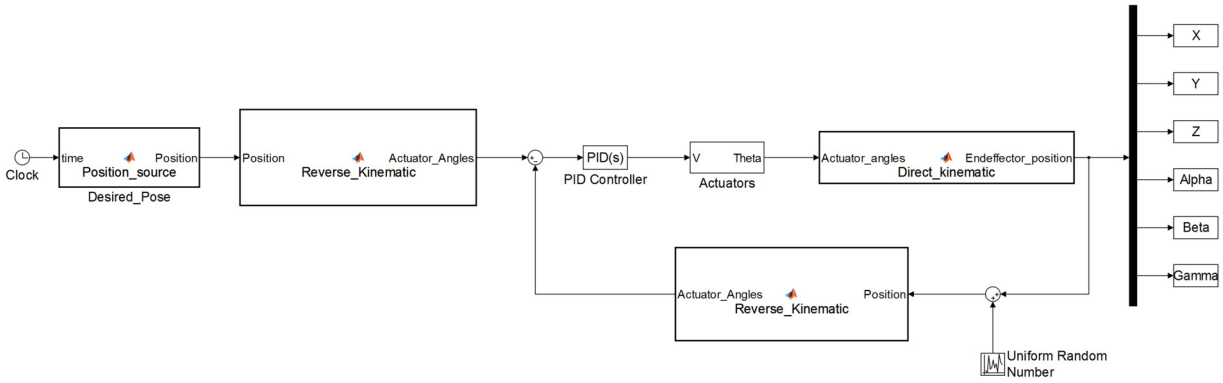

Figure 4.16: Schematic of proposed controller in the presence of the noise

Figs.4.17 -4.22 indicate the behavior of the system in presence of the noise.

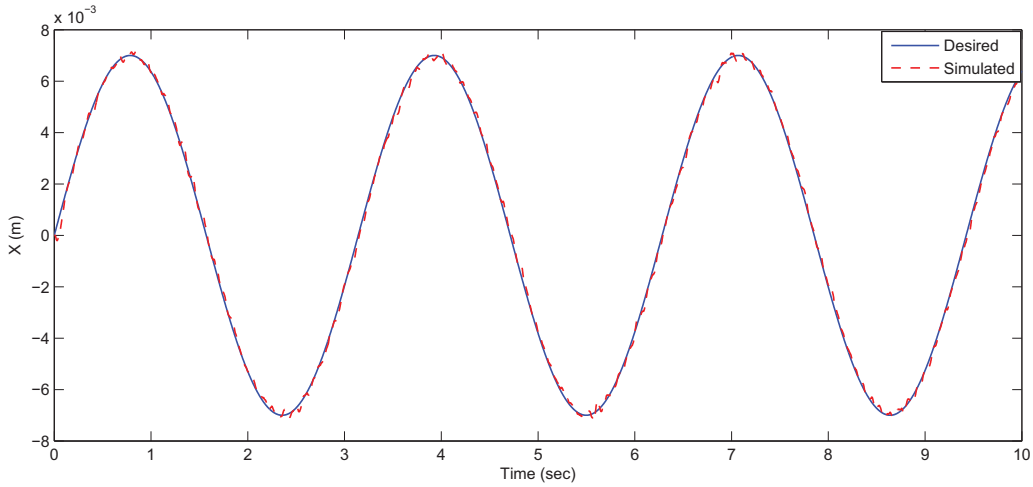

Figure 4.17: Sinusoidal response for pose of EE along X direction in presence of the noise

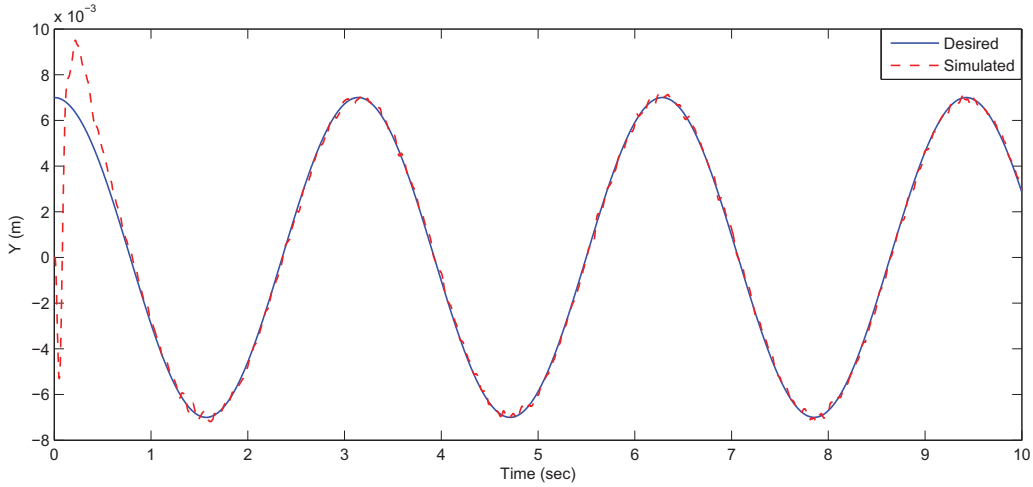

Figure 4.18: Cosinusoidal response for pose of EE along Y direction in presence of the noise

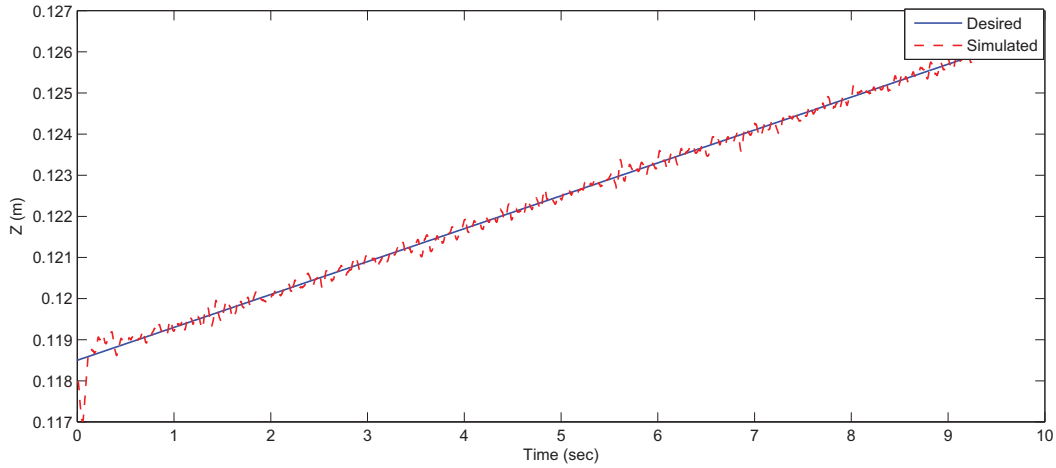

Figure 4.19: Ramp response for pose of EE along Z direction

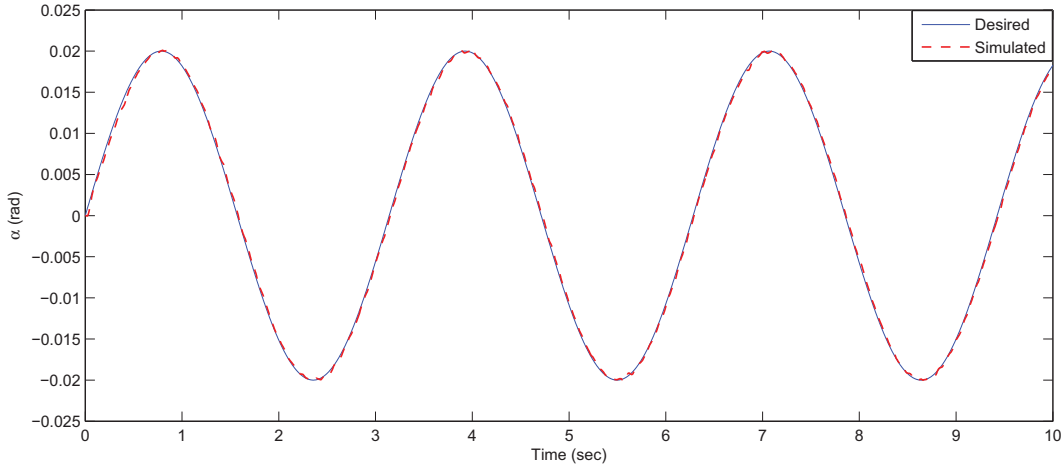

Figure 4.20: Sinusoidal response for pose of EE about X direction (α) in presence of noise

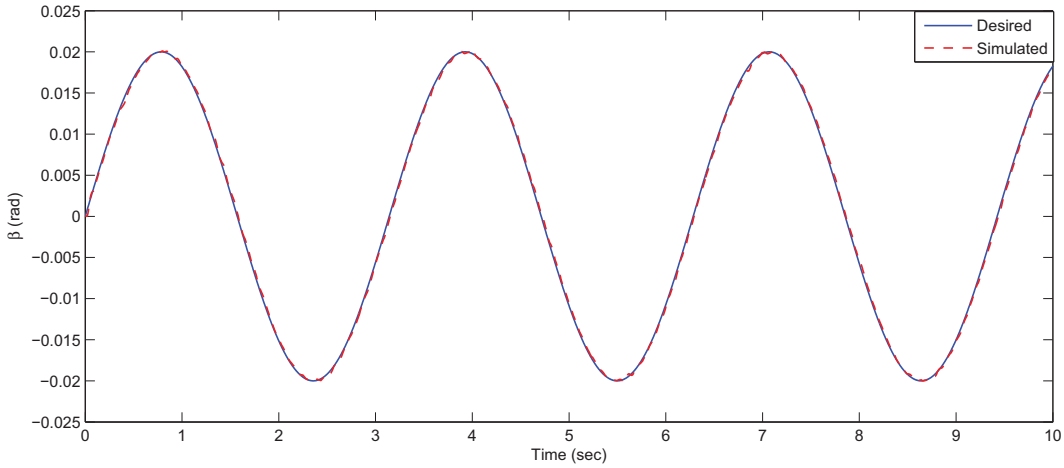

Figure 4.21: Sinusoidal response for pose of EE about Y direction (β) in presence of noise

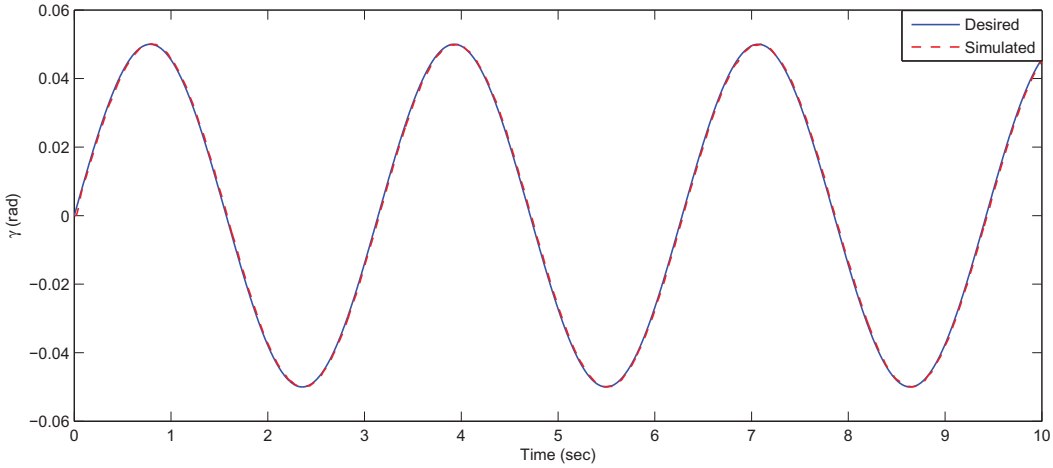

Figure 4.22: Sinusoidal response for pose of EE about Z direction (γ) in presence of noise

Figs.4.17- 4.22 show the performance of the PID controller in presence of the noise. as it can be seen, designed controller is proper for the system when a random noise with a variance value of 0.5 is applied to system.

To see the performance of the controller, a noise is added to the system. Also, to make sure that the designed controller enables to reject the pose disturbance introduced by the fiber placement head, a step pose disturbance with value of 2 mm is applied to the pose of EE in sixth and eighth seconds as follows,

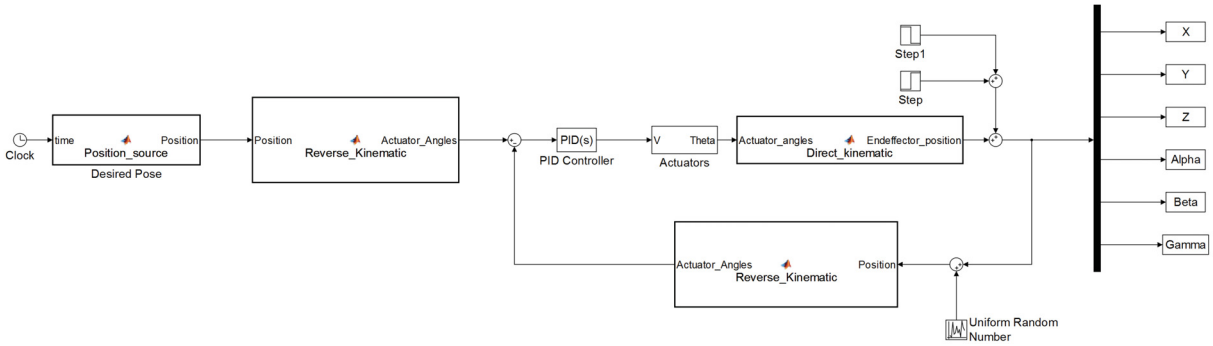

Figure 4.23: Schematic of proposed PID controller in the presence of disturbance and noise

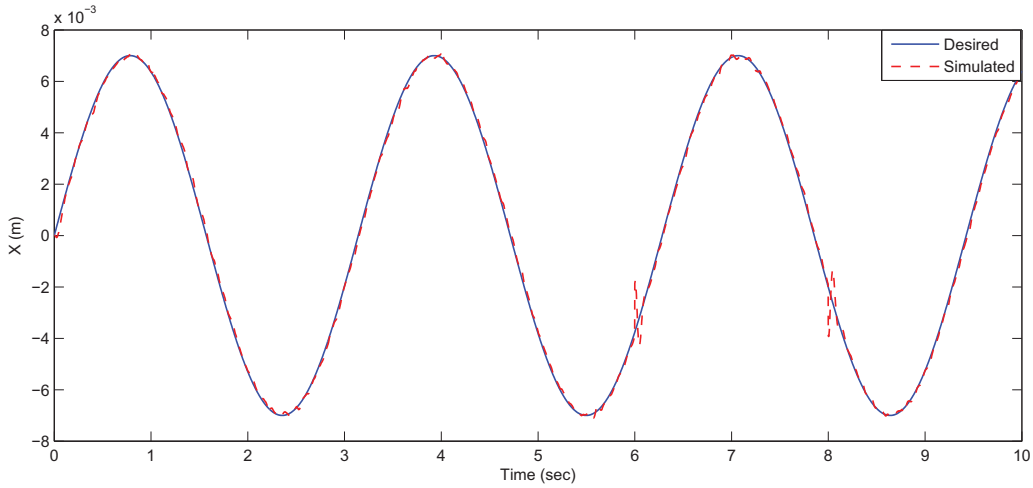

Figure 4.24: Sinusoidal response for pose of EE along X direction in the presence of disturbance and noise

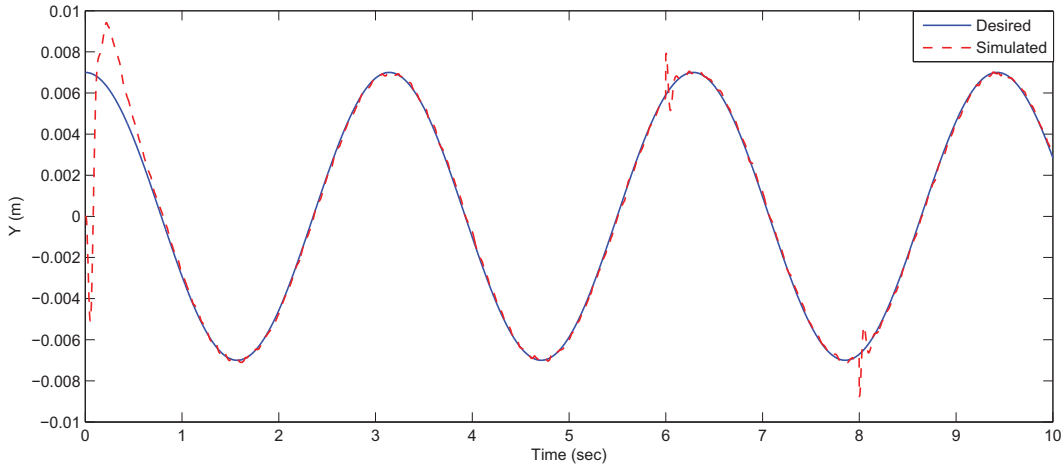

Figure 4.25: Cosinusoidal response for pose of EE along Y direction in the presence of disturbance and noise

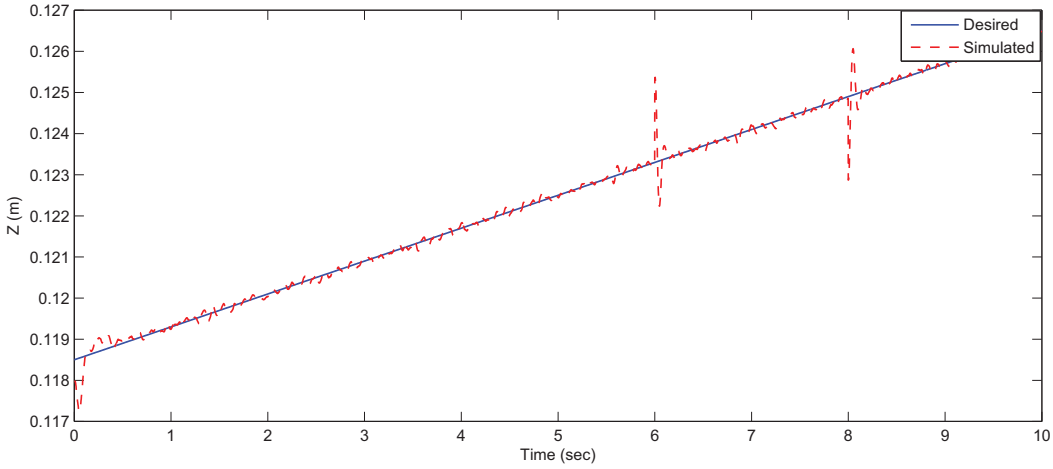

Figure 4.26: Ramp response for pose of EE along Z direction in the presence of disturbance and noise

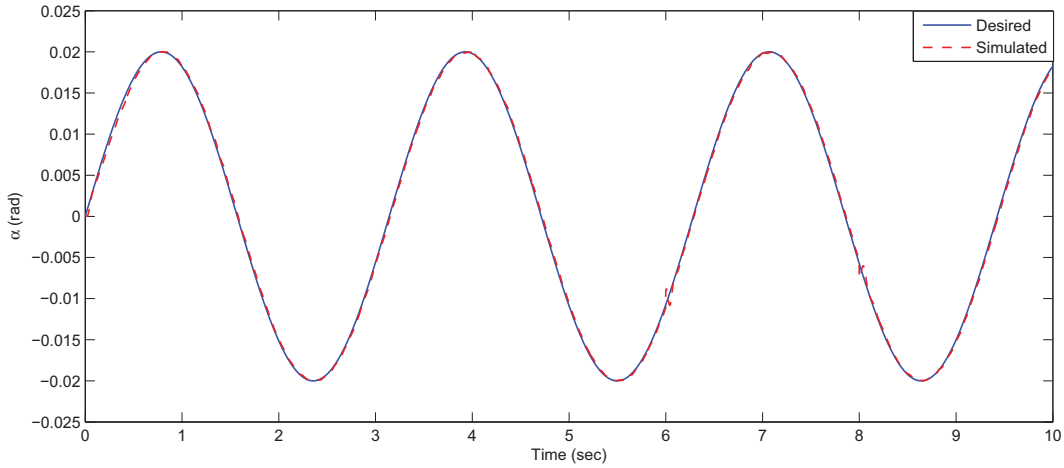

Figure 4.27: Sinusoidal response for pose of EE about X direction (α) in the presence of disturbance and noise

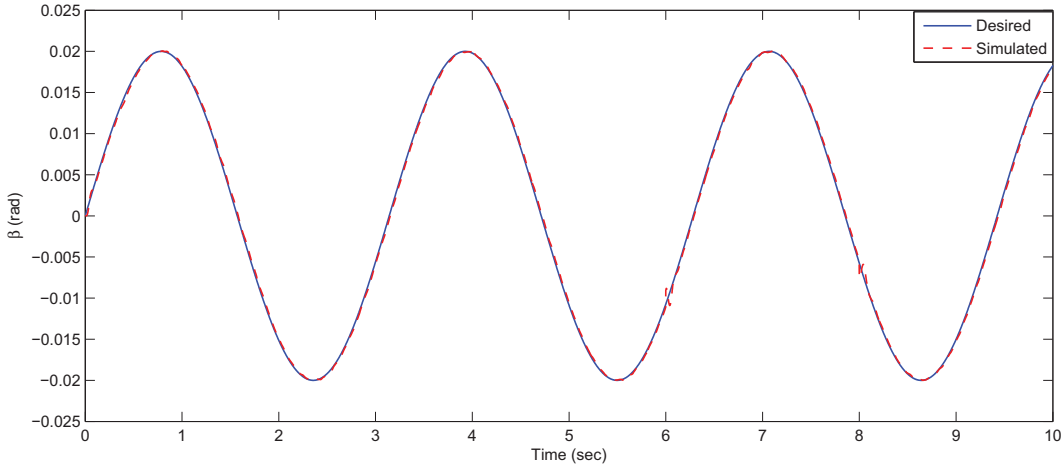

Figure 4.28: Sinusoidal response for pose of EE about Y direction (β) in the presence of disturbance and noise

Table 4.2: Comparing the pose' steady state error with and without PID controllers

	$X\ (mm)$	$Y\ (mm)$	$Z\ (mm)$
Without controller	0.5	0.6	0.1
With controller	0.032	0.032	0
With controller, with noise	0.102	0.149	0.2
With controller, with disturbance and noise	0.071	0.0012	0.2

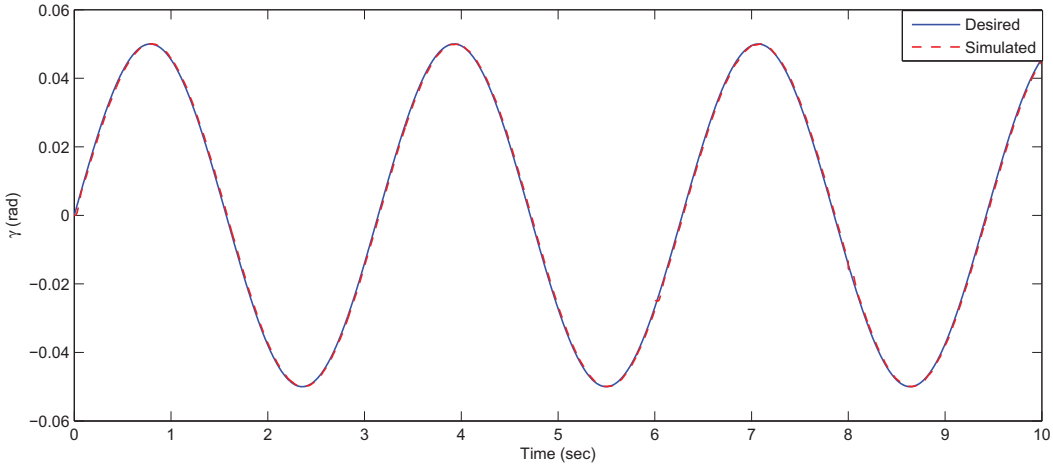

Figure 4.29: Sinusoidal response for pose of EE about Z direction (γ) in the presence of disturbance and noise

Figs.4.24- 4.29 show the behavior of the closed-loop system in presence of the random noise (0.3) and step pose disturbance introduced by the fiber placement head (2mm), respectively.

In order to calculate the error we used both steady state error and Integral Time-weighted Absolute Error (ITAE) between the desired pose and the simulated pose. The Integral Time-weighted Absolute Error (ITAE) is defined as,

$$ITAE = \int t|\epsilon|dt \tag{4.9}$$

where t is time (sec) and ϵ is the discrepancy of the desired pose with the simulated one (mm).

Table.4.2 and 4.3 show the pose'error of the EE's pose with and without Controller. Using PID controller, As it is shown, the desired path is tracked very well. Therefore, the applied controller is proper for the system.

Table 4.3: Comparing the pose' ITAE with and without PID controllers

	$X\ (mm.s^2)$	$Y\ (mm.s^2)$	$Z\ (mm.s^2)$
Without controller	50.2995	47.5572	4.3611
With controller	4.5251	4.6365	0.4032
With controller, with noise	5.9644	5.6992	4.0743
With controller, with disturbance and noise	5.9882	5.9934	3.5813

4.2 Controlling the Pose of EE in Presence of Nonlinear BLDC Motor Model

In order to evaluate the performance of the controller, a desired trajectory is defined as follows:

$$x = 17sin(2t) \tag{4.10}$$

$$y = 17cos(2t) \tag{4.11}$$

$$z = 118.5 + (0.2/250)t \tag{4.12}$$

$$\alpha = 0.02sin(2t) \tag{4.13}$$

$$\beta = 0.02sin(2t) \tag{4.14}$$

$$\gamma = 0.05sin(2t) \tag{4.15}$$

where, t is time (sec), x, y, z are the position of EE (mm) and α, β and γ are rotations about x, y, z axises (rad), respectively.

4.2.1 Tuning PID controller Using GA

In this work, GA is used to find the parameters of PID controller. The following objective function is defined which is the norm of error between the desired pose and actual pose. Using GA, this objective function should be minimized:

$$J = ||\vec{e}||_2 \tag{4.16}$$

where $\vec{e} = [e_x, e_y, e_z, e_\alpha, e_\beta, e_\gamma]^T$. For example e_x is the error between desired the x position and actual one. Similarly the other errors can be defined.

Table 4.4: PID tuned by GA

K_p	K_d	K_i
7.627	2.561	7.692

Table 4.5: The pose'error of each axis in presence of tuned PID controller

X axis (mm)	0.6
Y axis (mm)	0.4
Z axis (mm)	0.2
α axis (deg)	0.112
β axis (deg)	0.089
γ axis (deg)	0.196

Using a population with the size of 50, crossover of 0.8 and the mutation probability of 0.1, after 150 iteration, the optimized gains are obtained. The GA has been carried out by $MATLAB$, optimization toolbox. The parameters of PID controller are shown in Table 4.4.

4.2.2 Simulation Results

Figs.4.30 - 4.35 show the response for EE's pose along x, y, z axises. Moreover, Table.4.5 shows the error of the pose of six axes in presence of tuned PID controller. In overall, although there are some overshoots at the beginning, the tuned PID controller follows the desired pose and provides a satisfactory performance for the system.

Therefore, the designed PID controller tuned by GA method is proper for the system.

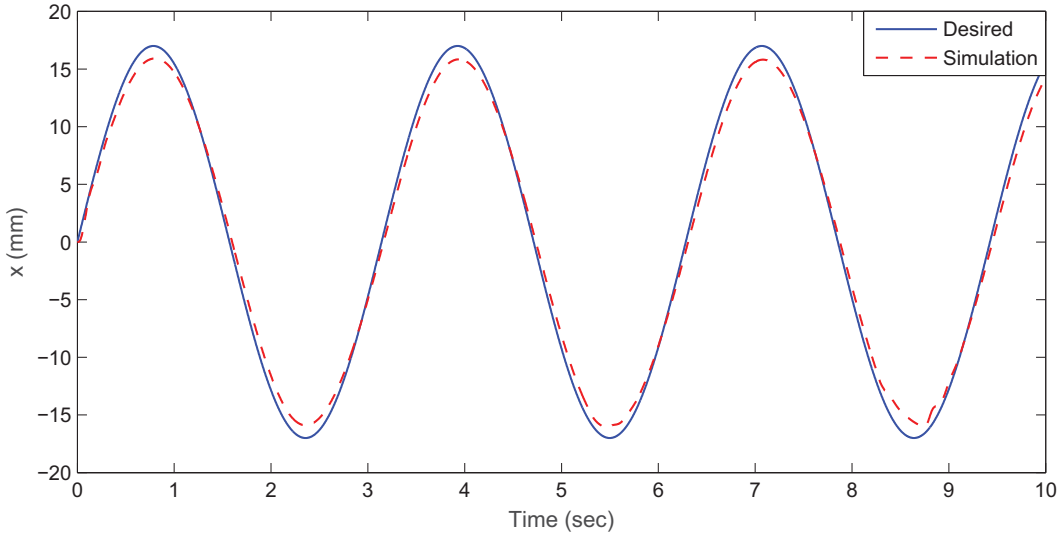

Figure 4.30: Sinusoidal response for pose of EE along x axis

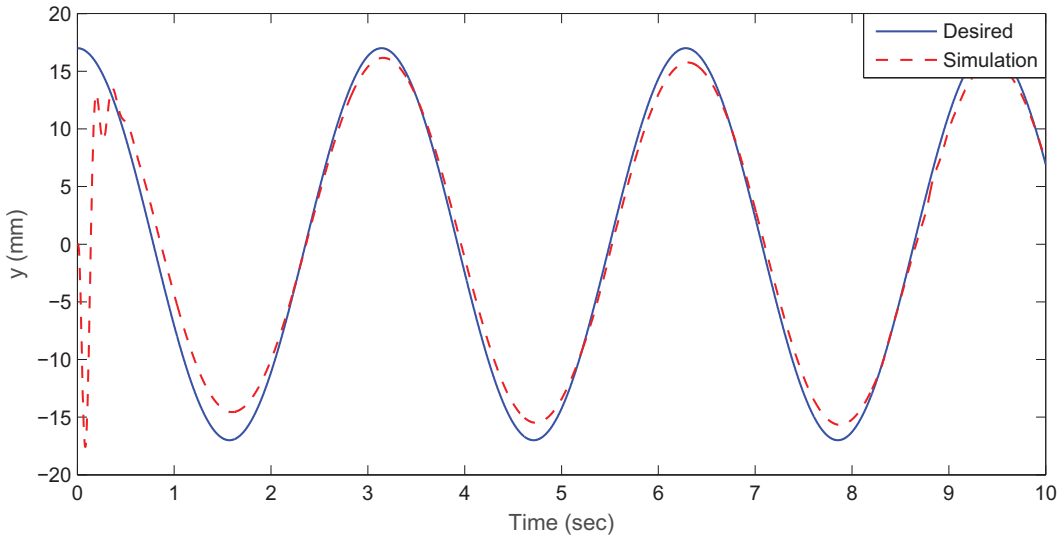

Figure 4.31: Cosinusoidal response for pose of EE along y axis

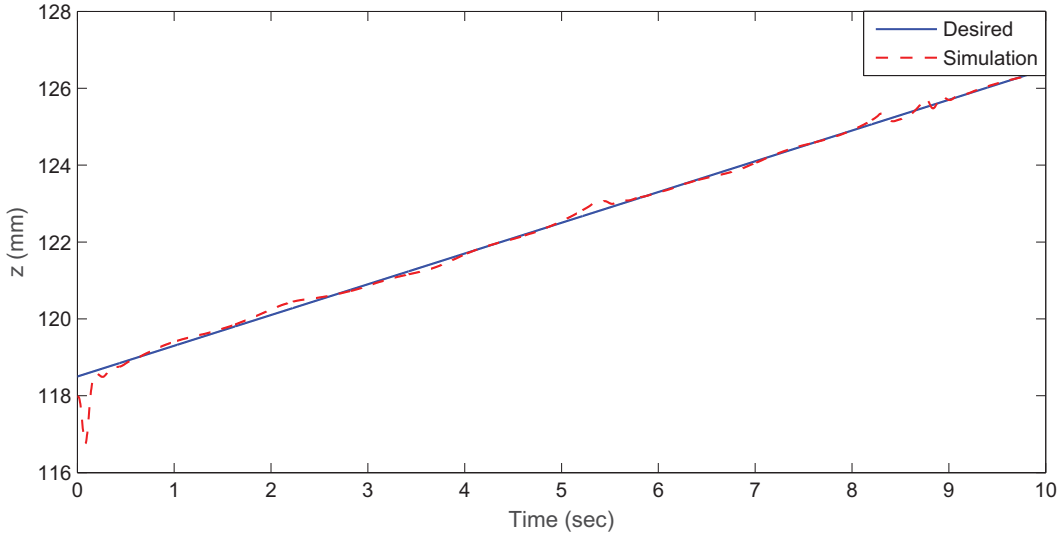

Figure 4.32: Ramp response for pose of EE along z axis

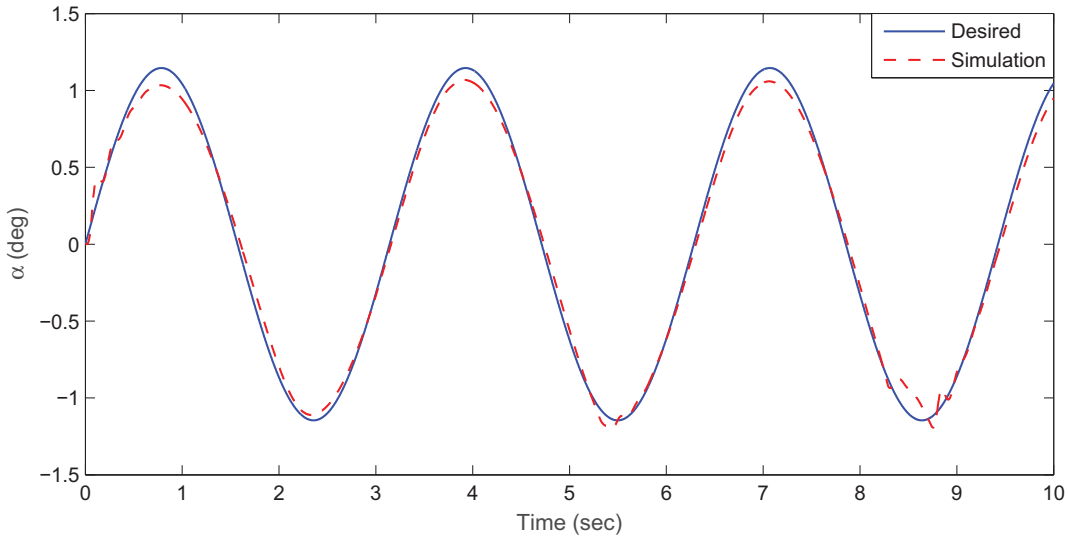

Figure 4.33: Sinusoidal response for pose of EE about x axis (α)

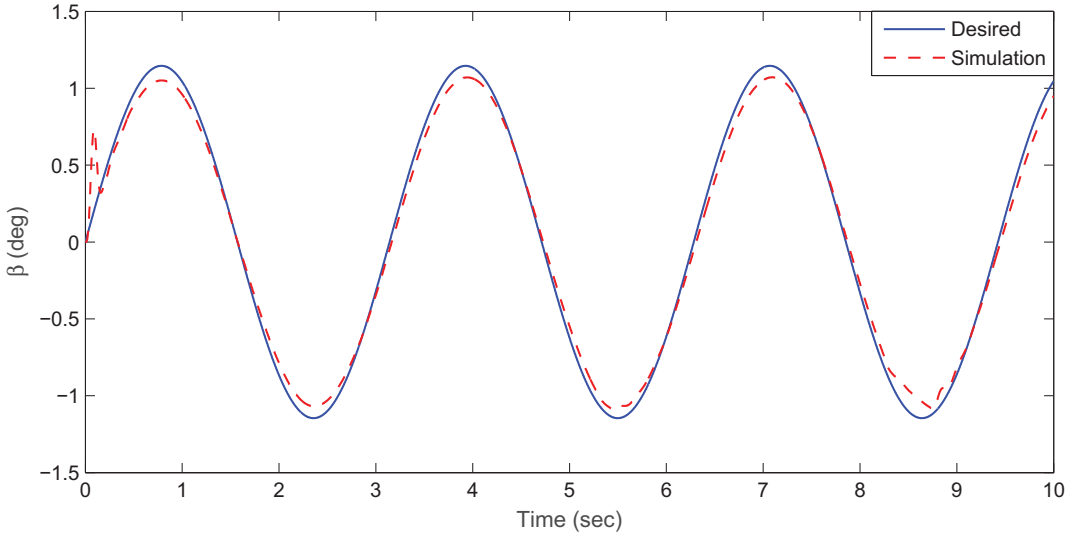

Figure 4.34: Sinusoidal response for pose of EE about y axis (β)

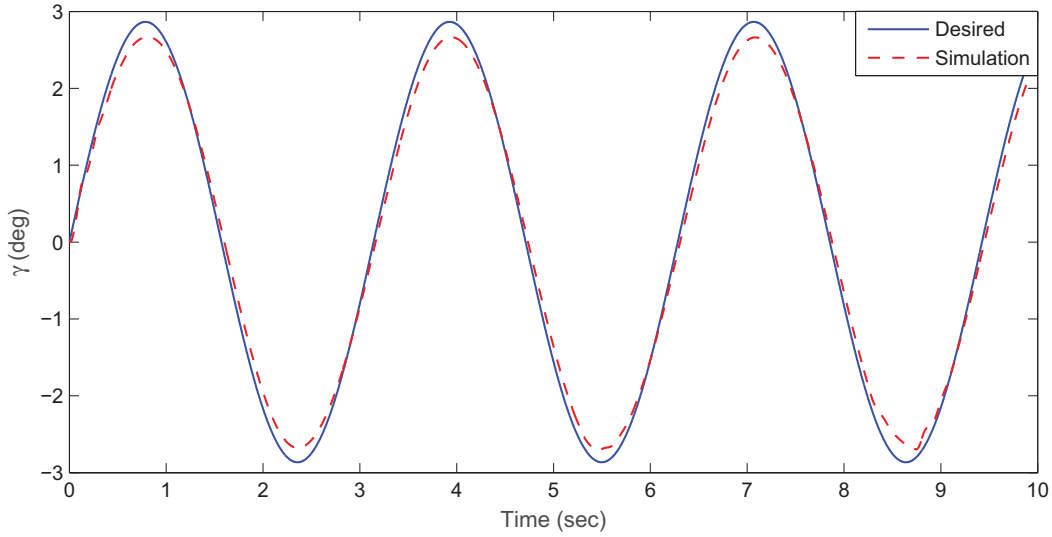

Figure 4.35: Sinusoidal response for pose of EE about z axis (γ)

4.3 Summary

In this chapter, PID controller for both linear and nonlinear actuators' models are introduced. By using PID controller, the pose of EE has been controlled when the 6-RSS robot worked with identified BLDC actuators' model. The simulation results show that the designed controller can

track different reference signals very well. Also, the robustness of the tuned controller is studied and it is shown the satisfactory performance of the tuned PID controller in the presence of both noise and disturbance.

Chapter 5

Experimental Results

To validate the desired pose control in the real time experiments, we need the accurate measurement of the parallel robot's pose. Thanks to the newly purchased photogrammetry sensor-C-track from Creaform Inc. The pose of EE can be measured. The closed-loop feedback pose control system can be built and the desired pose control can be tested for the pose tracking in real time.

5.1 C-track

In order to validate the kinematics equation C-track has been used. C-track is a system which tracks the pose of the target. Among many detecting tools, such as laser tracker or vision systems, C-track can provide accurate measurement at relative low cost. It consists of several part, including; two cameras which observe the position of robot and send the accurate pose of EE to computer, a controller, a cone, a calibration bar which used to calibrate the C-track, a handy probe, reflectors which are called targets.

Figs.5.1 and 5.2 show several parts of C-track.

(a) Reflector (b) Controller (c) Calibration

Figure 5.1: C-track parts

(d) Handy probe (e) C-track

Figure 5.2: C-track parts

In C-Track, two cameras obtain the positioning targets simultaneously, which enables the software to determine the position through triangulation.

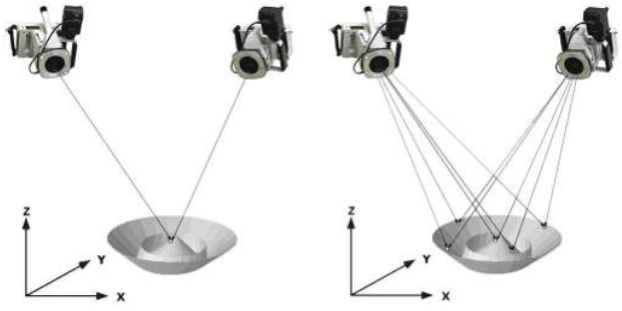

Figure 5.3: Capturing targets by two cameras simultaneously

The purpose of this section is to validate the theoretical inverse kinematic model that has been made in Simulink block. To do so, C-track is used to give the pose of EE. The desired pose is

given to the inverse kinematic block and applied to the system, and then the robot moves. The pose of robot is tracked by C-track and the data is sent to VXelements software. Comparing the pose of EE obtained by C-track with the desired pose input to inverse kinematics, we can validate the inverse kinematic model.

5.1.1 Hardware Difficulties

In this experimental work we faced with two challenges:

1. Through two computers: Using two quanser cards, the robot is controlled by the computer (called PC1) and the angle of each actuator could be obtained through Simulink block diagram. Unfortunately the computer that is used for C-track (PC2), differs from the computer which the parallel robot is connected to. Because C-track needs the high load of computation, implementing both the C-track data acquisition and control algorithm on one computer slows down the process and has negative effects on real-time performance of the system. Also, we have some hardware limitations:

    - The C-track license is only used for the PC2.
    - The computer that is used for the C-track can not support two Quanser cards.
    - The PC2 is also used to control the Fanuc robot which holds the fiber placement head in the project.

    In order to solve the problem, a following experimental setup is built,

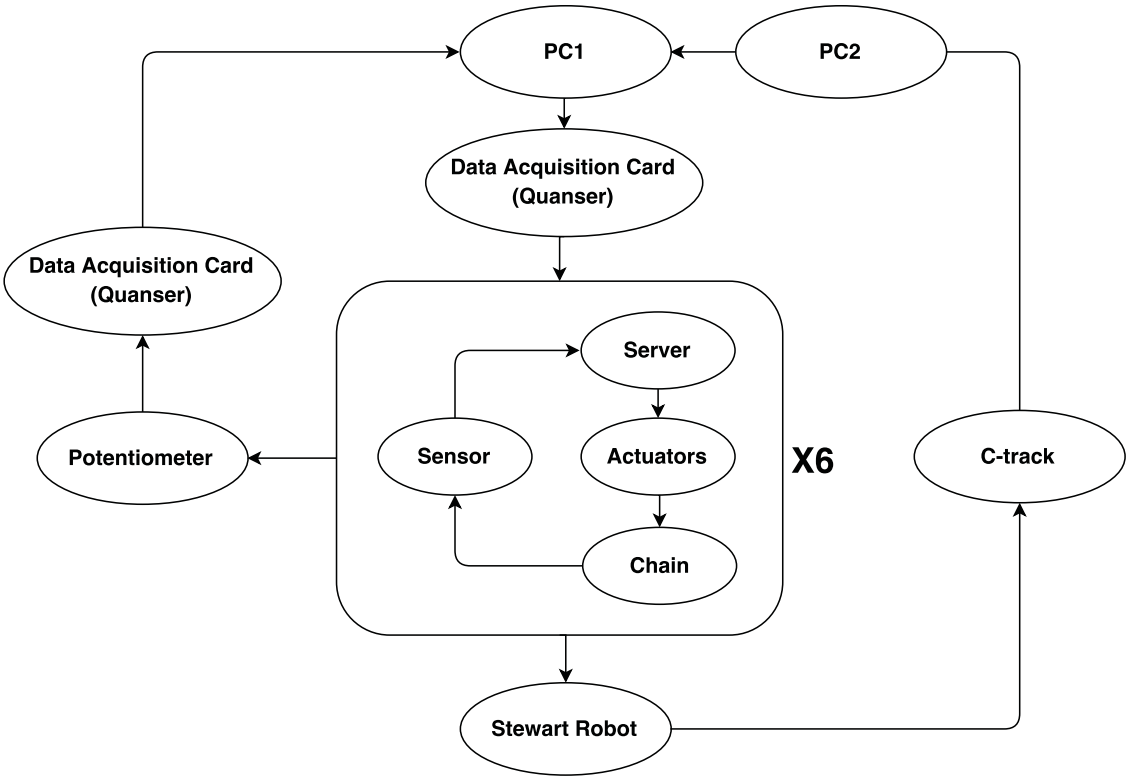

Figure 5.4: Experimental setup for parallel robot

To be able to use the pose measured by C-track for closed-loop controller, the data must be transferred between two PCs. A Simulink file has been made in which we give the voltage as an input and get the angles of each actuator as the output of the system. One of the Quanser card is used to send the applied voltage to six actuators. Each time we run the program, the power is applied to the actuators and drive both actuators and robot to move. Then, the potentiometer is used to measure the angle of each actuator. Using the second Quanser card, the measured data by potentiometer is sent to PC1.

Also, as it is shown, C-track is connected to PC2. The C-track detects the pose of EE and sends the data to PC2.

2. Using two softwares: The inverse equations code is written in $MATLAB$, while the captured data by C-track is sent to VXelements software. In order to form a real-time feedback system, we need to transfer data from VXelements software to $MATLAB$ or vice versa.

A code is written in Visual Basic (VB) programing language software in which we can connect

to VXelements software. It means that the data tracked by C-track can be seen, as an output of the VB code. The goal of using VB is to find a way to transfer the C-track data to $MATLAB$ software. It is necessary to solve the first mentioned problem. To do so, we use a double serial port in order to connect two computers. Furthermore, a code is written in VB which exports the data to serial port and a code is written in $MATLAB$ which imports the data from the serial port.

In order to measure the pose of EE, C-track should be calibrated. The following procedure illustrates how to calibrate the C-track:

- It should not be placed facing the sun or intense light, because intense light causes an optical noise in the C-Track field of vision.
- The environment's temperature should be in the range of was (+/- 2 C) during calibration.

In order to use the handy probe, it should be calibrated as well. To do so, the following sequences are followed:

1. We created a dynamic referential prior to calibration.
2. Enough positioning targets were distributed in volume. These targets were not placed symmetrically in order to increase the accuracy.
3. We placed the handy probe in the cone which has a distance about 2 m from the C-track. In order to reduce the error of calibration, the cone should not move during the process. So we locked the cone to the surface.
4. We clicked on the start bottom to start the calibration and followed the steps shown on the screen.

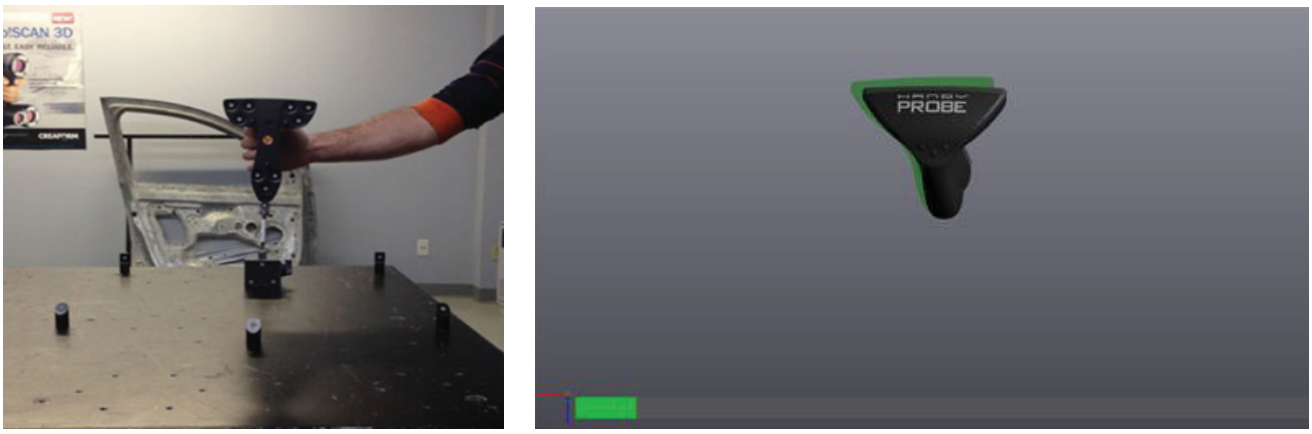

Figure 5.5: Probe calibration

The errors of calibration for both probe and C-track should be less than 0.04 mm. If the process takes too much time, the accuracy of probing might be influenced.

Firstly, the robot's EE should be cleaned in order to stick the target on it. The robot should not be greasy because the target should not move or fall during the measurement. We attached at least 4 targets on the parallel robot where C-track could see these targets. The more targets could be seen by C-track, the more accurate targets position can be measured. The targets are distributed in the volume and the positioning target is sticked asymmetrically to increase the accuracy of inspection. This distribution is affected by many conditions; such as,

- If we spread the targets in longer distances, C-track could measure data in a wider range.
- Covering 3 axis: The target covers 3 axes and gives the C-track adequate reference in all of these axes.

In this work we tried to consider all above conditions to increase the accuracy.

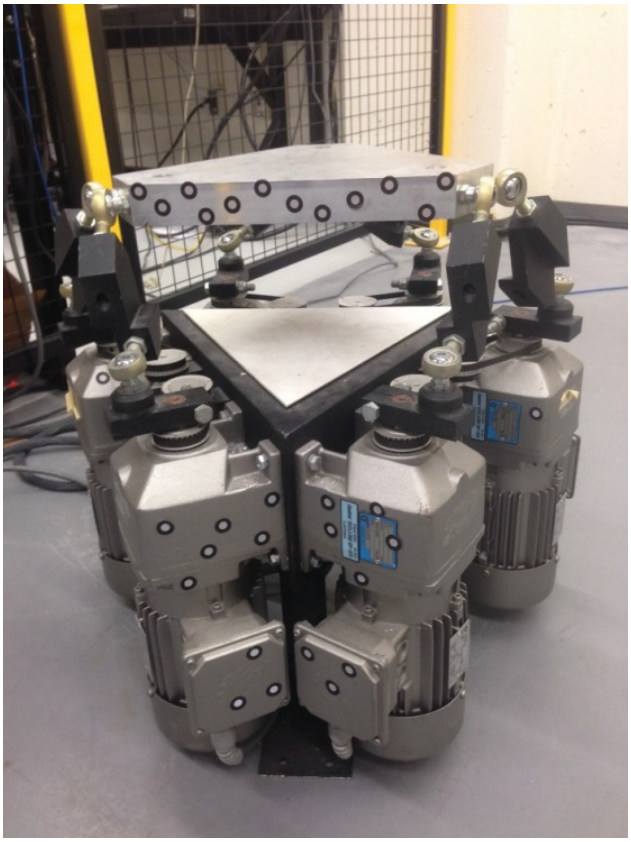

Figure 5.6: Parallel robot

In order to work with the software, we need to make a new session first. In our new session, C-track observed thirteen targets at the same time and these targets are saved as the positioning targets. As far as C-track could see at least four targets among the positioning targets, we can work in the VXelements software. C-track has four referencing modes: static, dynamic, sensor and automatic. Each mode has its own features:

- Sensor mode: In this mode, C-track and part cannot move during the work.
- Dynamic mode: When the environment of work has vibrations, it is suggested to use dynamic mode. In this mode the positioning targets need to remain in the place where they are detected at first time. Each time, a minimum of four positioning targets should be observed by C-track as well. The most important feature is that we can move the C-track during the experimental work.
- Static mode: In contrast to dynamic mode, when we use the static mode we are not allowed

to move the C-track and the part during the measurement. But the advantage of this mode is C-track does not need to see the targets each time we are measuring.

- Automatic mode: It is a combination of static and dynamic modes. In this kind of mode, a minimum of one positioning target must to be seen by C-track during the measurement all the time. If the visible positioning targets are less than four, the system switches to static mode automatically. Furthermore, the targets could not be obstructed more than five minutes.

In this experimental work, the dynamic referential mode is used because we need to move the C-tracks location during the measurement.

After creating new session, the first idea was to align a frame as our original (reference) frame of parallel robot on one of the six motors. Using this method, the pose of EE with respect to the location of motor (reference frame) could be determined. The main problem was: in the inverse kinematic equations we used the mid-point of lower platform as an original frame, so in order to validate the inverse kinematic equations with experimental results, we need to find the pose of EE with respect to the base frame defined in the inverse kinematics.

Hence, the idea of using actuator's position as a base frame is changed to find the middle point of the lower frame of parallel robot. If we attach the target in the middle of base plate, we have two problems: first the location of mid-point we choose is not accurate enough because it is based on the observation by eyes. Second, C-track could not see the target on the mid-point. To do so, we decided to find the mid-point of base frame based on the following sequences:

1. Creating four circles to find point B_i (motor positions):

   C-track could not see four motors among six ones at the same time. We were probing several points on each motors surface. Because we need to create a circle for each motor, we need to probe at least three points. In VXelements software we chose circle bottom in order to create the circle. In point selection bottom, we select four points or more on individual circle. The error of each circle should be less than 0.04 mm. If we select only three points, the software does give us the error of the created each circle. Then we did the same sequences for every other wanted circle.

2. Finding the center point of each circle (B_1, B_2, B_3 and B_4): After we made four circles, we

can find the mid-point of each circle. These obtained points are called B_1, B_2, B_3 and B_4 in our inverse kinematic equations, which are the location of four motors (revolute joints).

3. Creating the Circle based on 4 points (B_1, B_2, B_3, B_4): After we find the location of each motor, we click on circle bottom again and choose the point selection. We choose mid-points of each circle and create our main circle using B_1, B_2, B_3 and B_4. If the error is less than 0.04 mm, the created circle is acceptable. If not, we need to repeat our work from Step One.

4. Finding the center of the main circle (O): After creating the main circle, we can obtain the center point where we want to align the original frame of parallel robot on.

After finding the middle point of the circle, it is time to align the frame, that is according to the reference frame used in inverse kinematic equations. Aligning the direction of z axis is easy, but the question is how to align the direction of x axis according to inverse kinematics. In the inverse kinematic equations, the x-axis is coincidence to the line which passes from referential point to the middle between B_1 and B_6 or the x-direction is against of the direction of the line which passes from referential point to the middle point between B_3 and B_4 (because robots geometry is symmetry). Thus, we need to find the mid-point between two motors, and then we can create the line using the obtained mid-point and reference point. If we want to find the mid-point between B_1 and B_6, the problem is that C-track could not see the sixth motor. Accordingly, in order to solve this problem, we used third and forth motors (B_3 and B_4) to find the mid-point. Then, we created the line from reference point to the mentioned mid-point. Using this line, we aligned the x-direction exactly against the direction of the created line. Using right hand rule for aligning the frame, we can align the direction of y axis. Now we have our referential frame.

In the next crucial step, we want to align Upper Frame (UP) which shows the pose of EE. In order to do that, we have done following sequences:

1. Modeling the UP using handy probe: in this step we used handy probe to detect several points on the surface of UP using optical method. We cannot use touching method, because in this method, the target should be visible.

   Unfortunately, the sticker targets on the surface of the UP are not observed by C-track. So we used optical probing method. After finding a minimum of three points we created the plate which is called UP.

2. Creating plate A, plate B, plate C, and plate D: using handy probe we probed the points on the plane A to D, then we created those planes in the VXelements.

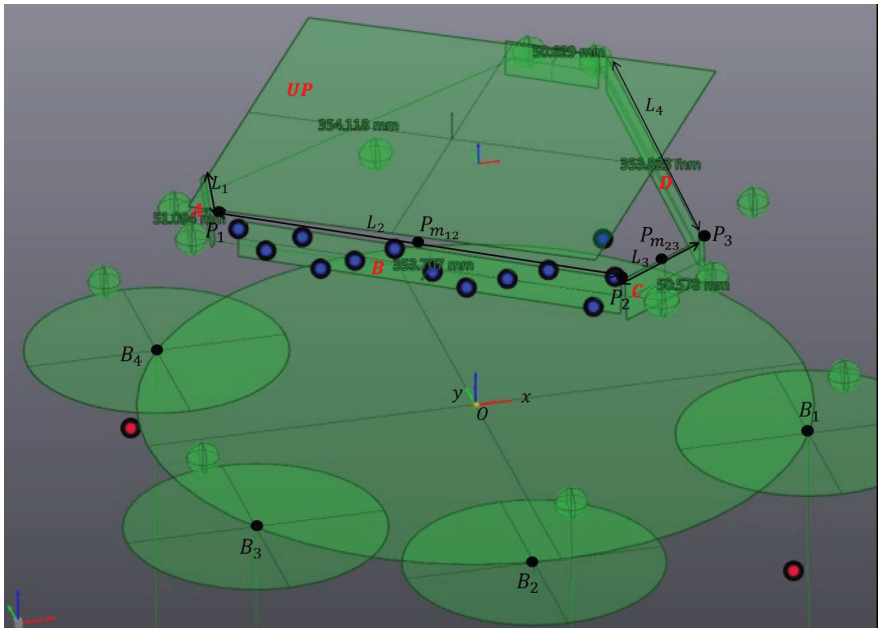

Figure 5.7: Parallel robot model in VXelements software

3. Finding the intersection line: The intersection of the two planes is a line. So we find the intersection line between the plane A and UP (L_1), the intersection line between plane B and UP (L_2), the intersection line between plane C and UP (L_3), and the intersection line between plane D and UP (L_4).

4. Finding the intersection points: the intersection of two lines is a point. Using four lines obtained in the previous step we could find the intersection point between two lines. The intersection point between L_1 and L_2 is called P_1, the intersection point between L_2 and L_3 is called P_2, and the intersection point between L_3 and L_4 is called P_3.

5. Finding the mid-point of both L_2 and L_3: using P_1 and P_2, we could find the mid-point of $L_2(P_{m_{12}})$. Also, we used the P_2 and P_3 in order to find the mid-point of $L_3(P_{m_{23}})$.

6. Finding the reference point: Based on our knowledge which proves $P_{m_{12}}$ is located on the plane B, we created the new line L_{m_1} which passed from $P_{m_{12}}$ and is normal to plane B. Also, we knew that $P_{m_{23}}$ is located on plane C, so we created the line L_{m_2} which is normal

to plane C and passed from$P_{m_{23}}$. Then we intersected these two lines. The intersection point is the reference point or the EE pose (O').

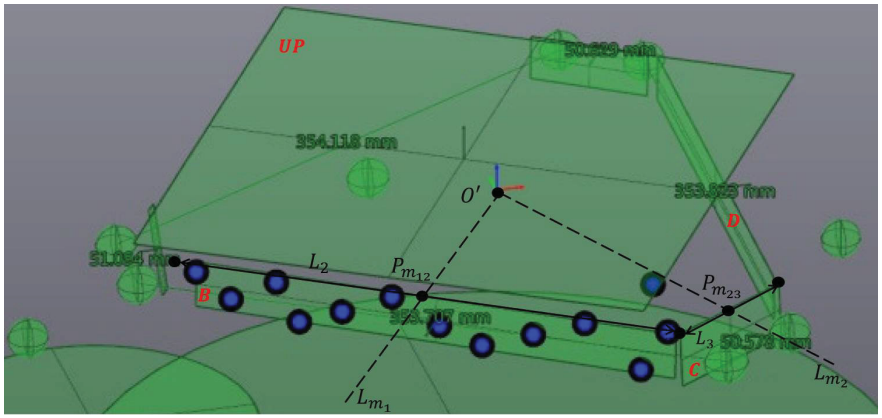

Figure 5.8: Finding EE pose

7. Aligning the Upper Frame $(O'x'y'z')$: In order to align the frame $(O'x'y'z')$ on the obtained reference point (O'), we need to create another line which is located in plane D. To do so, we probed plane F, the same as before, we found the intersection line between UP and plate F (L_5). Using L_4 and L_5 we found the intersection point (P_4). Then, we found the mid-point between P_3 and P_4 which is called $P_{m_{34}}$. we created the line from O' to the $P_{m_{34}}$. Using this line, we aligned the x'-direction exactly in the direction of the created line. Also, we aligned the z'-direction which is exactly normal to UP. Using right handle rule, the direction of the y' is obtained.

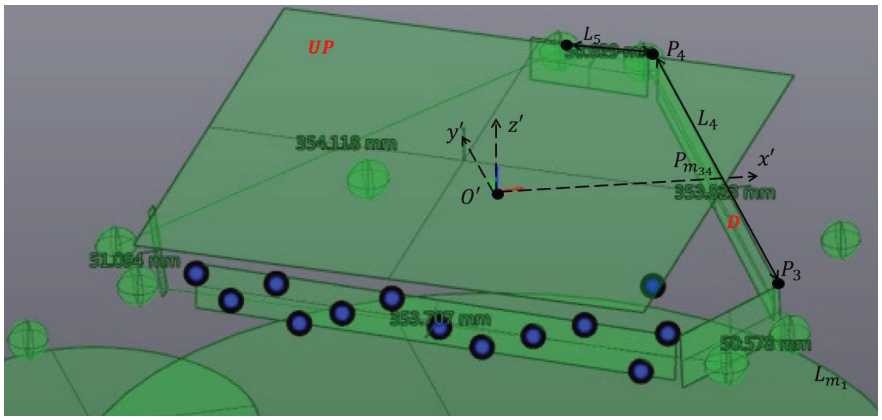

Figure 5.9: Aligning frame $O'x'y'z'$ pose

Now we have both Base Frame and UP, which means that the relationship between the pose of EE with respect to base frame could be detected by C-track. We fixed the Base Frame as the original frame, so we can track the pose of parallel robot with respect to the original frame. When we click on track bottom in the VXelements software, it gives us the pose of EE each 1/29 second. Then we export this data as a tracking sequence and then importing the tracking sequence in visual basic (VB) software. There is a written code in VB environment which we can used to see the results in VB environment. We should make sure that each time we connect the VB software to C-track in order to see the data, the VXelements software is closed. The reason we should close the VXelements software is that the C-track cannot connect with two softwares at the same time.

The sequences are shown as follows:

1. Open the code in VXelements.
2. Clicking on “start bottom”, a window shows up.
3. Clicking on “connect to VXelements”.
4. Clicking on open targets, give us the data positioning of original frame.
5. Importing the data (positioning targets) of upper frame and adding this data as a sequence.
6. Completing the previous sequences, the pose of EE with respect to the base frame is shown in Fig.5.10.

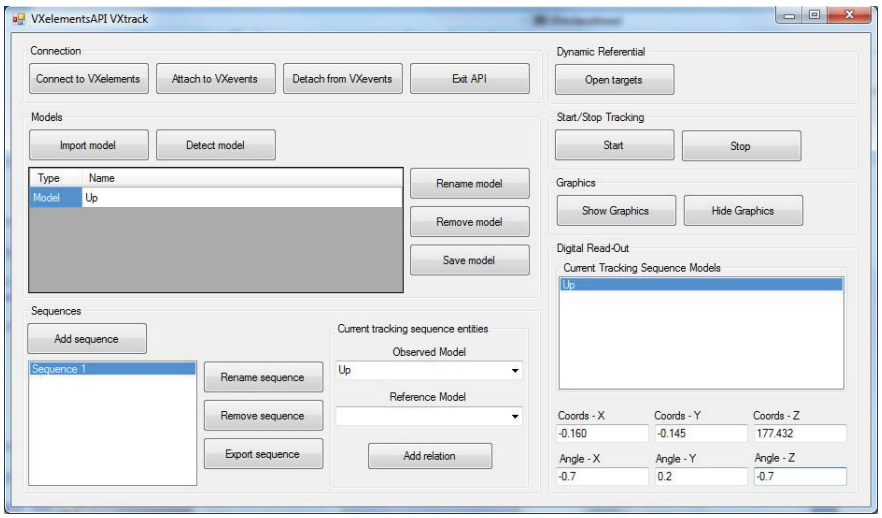

Figure 5.10: Visual basic model

Table 5.1: Measuring L_{AT_i} by C-track

L_{AT_i}	$i=1$	$i=2$	$i=3$	$i=4$	$i=5$	$i=6$	average
mm	166.861	162.066	165.651	163.263	165.105	159.396	163.7236

Comparing the results tracked by C-track with the desired pose has a huge error which means the inverse kinematic model is not accurate. All the lengths and angles we used for inverse kinematic equations were measured by the ruler, so they were not accurate enough and caused a considerable error. Another reason is due to neglecting the L_z in the initial inverse kinematics to simplify the equation.

In order to reduce the error, we have calibrated some parameters. The sequences are listed as follows:

1. Modifying L_{AT_i}: At first, we used the value of 165mm for L_{AT_i} in the inverse kinematics equation, which was measured by the ruler. Using the C-track, this value is reduced from 165 mm to 163.7236 mm which is the average of six L_{AT_i}. In order to measure the value of L_{AT_i} :

   - We probed the sphere A_i $(i = 1, 2, 6)$ and T_i $(i = 1, 2, 6)$.
   - Then, we created 6 lines $(AT_1, AT_2, , AT_6)$ and measured the length of line.
   - We took the average from line AT_1, to line AT_6; the final value is 163.7236 mm.

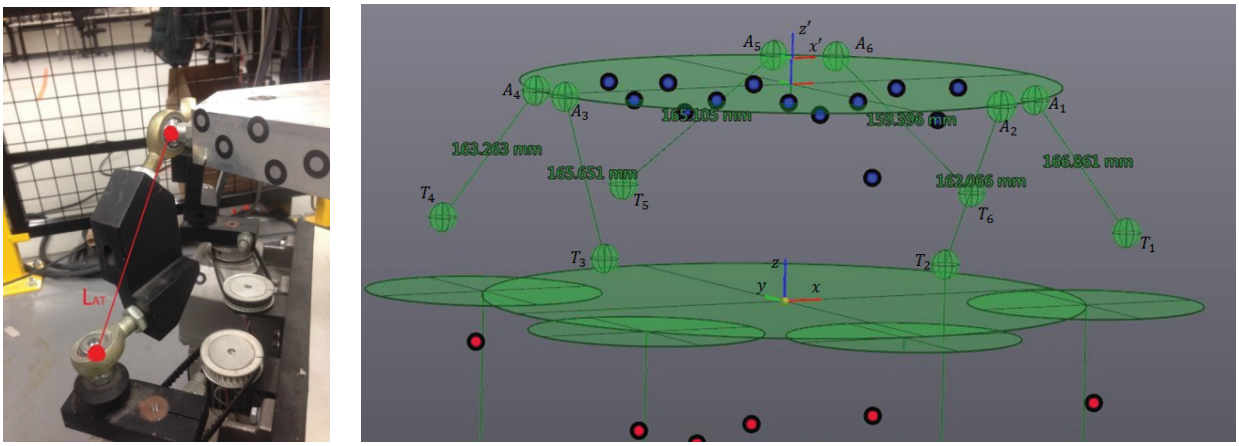

Figure 5.11: Lenght of AT_i

Table 5.2: Measuring L_{z_i} by C-track

L_{z_i}	$i=1$	$i=2$	$i=3$	$i=4$	$i=5$	average
mm	40.952	39.836	39.372	38.903	39.016	39.62

2. Adding L_z : first we neglected the L_z, while this length has a value of 39.6158 mm. To obtain the precise value of L_z :

   - Creating four planes: C-track could see only five actuators $(B_1, B_2, B_3, B_4, B_5)$. So we created five plates which passed from $B_i(i = 1, 2, 5)$ and paralleled to the base plate.
   - Creating four lines: Clicking on point to normal bottom, we created the normal line from sphere $T_1$to plate B_1 and so on $(L_{z_1}, L_{z_2}, L_{z_3}$ and $L_{z_4})$.
   - We took the average from line L_{z_1}, to line L_{z_5} the final value is 38.455 mm.

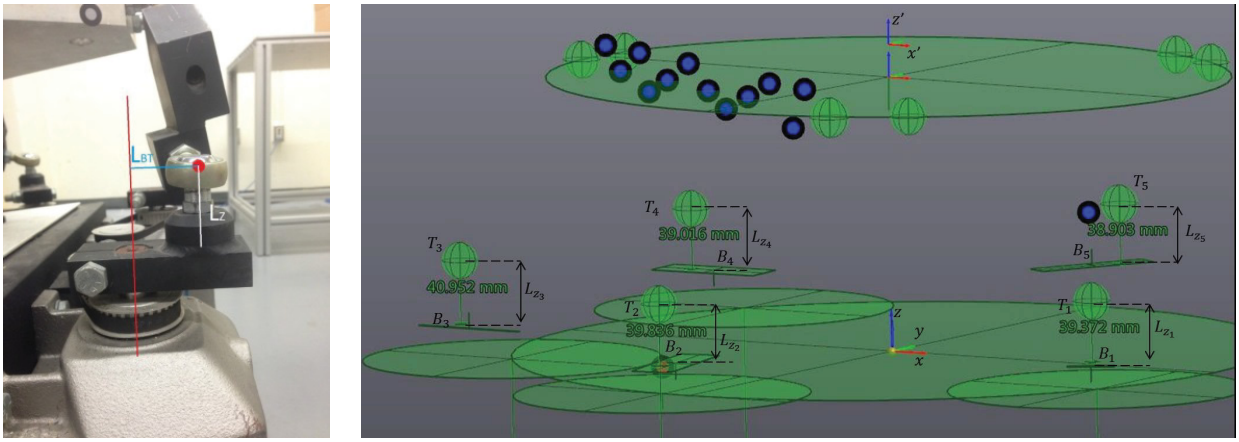

Figure 5.12: Lenght of L_z

3. ModifyingL_{A_i}: Using the C-track the values of $L_{A_{1-2}}$, $L_{A_{2-3}}$ $L_{A_{3-4}}$, $L_{A_{4-5}}$, $L_{A_{5-6}}$, $L_{A_{6-1}}$ have been changed.

Table 5.3: Measuring L_{A_i} by C-track

L_A	$L_{A_{12}}$	$L_{A_{34}}$	$L_{A_{56}}$	$L_{A_{23}}$	$L_{A_{45}}$	$L_{A_{61}}$
mm	50.578	51.094	50.629	353.707	354.118	353.823
Average	50.767			353.883		

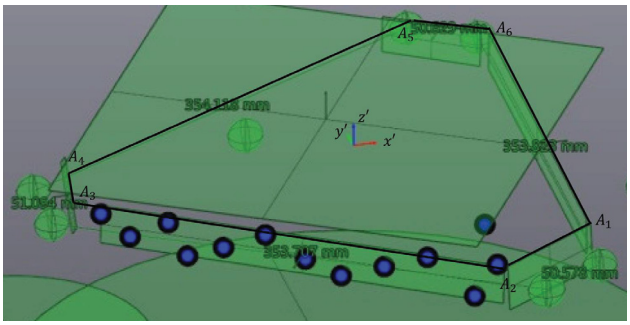

Figure 5.13: Modifying L_A

4. Modifying L_{BT}: The initial L_{BT} was considered as 40 mm. This value is measured by the ruler. To obtain the accurate value of L_{BT}, we have done following steps:

   - We created the line which is normal to plate B_1 and passed from point B_1. This line is called b_1. We created three other lines (b_1, b_2, b_3) like the first one.
   - We measured the distance between sphere $T_1$to b_1. We measured other three distances.
   - We took the average from four distances; the final value is 38.455 mm.

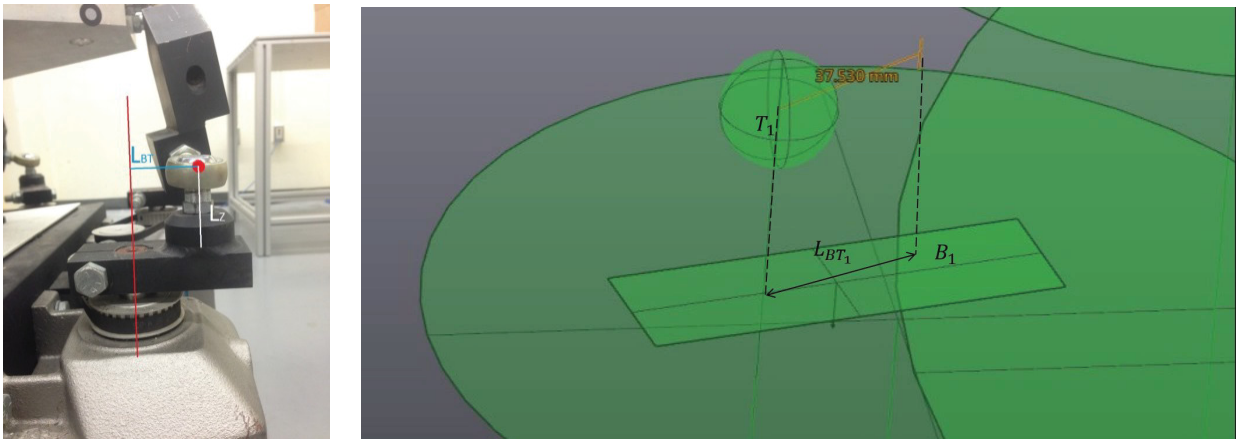

Figure 5.14: Length of BT_i

Table 5.4: Measuring L_{BT_i} by C-track

L_{BT_i}	$i=1$	$i=2$	$i=3$	$i=4$	average
mm	37.530	39.24	39.230	38.037	38.509

5. Adding the offset to upper frame: The inverse kinematic model considered the EE pose in the middle of the upper plates thickness, while we considered the EE pose on the surface of upper plate using C-track. This difference caused 20mm error in z-direction.

In order to reduce the error, we proposed two ways: Changing the inverse kinematics or changing the model we built. The easiest way is to change the model we have built in the software. So we created the plate which passed from sphere $A_i(i = 1, 2, 6)$ and is parallel to upper plate. Then we translated the upper frame to the center of new plate. We gave two sine inputs with the amplitudes of 10mm in x and y directions, a cosine input with an amplitude of 10 mm in z-direction as three positions. The following graph compares the results of C-track with desired pose:

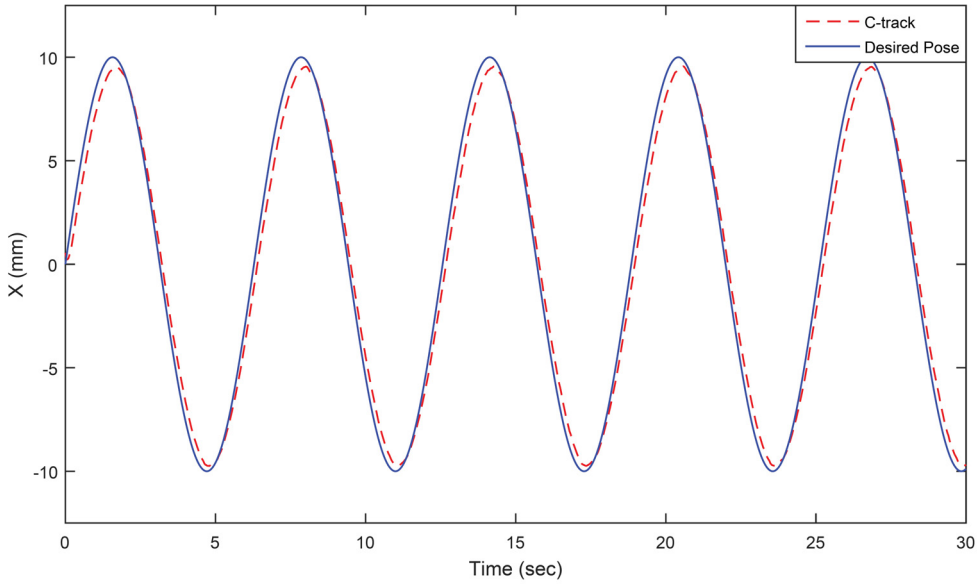

Figure 5.15: Sinusoidal response for pose of the EE along X direction

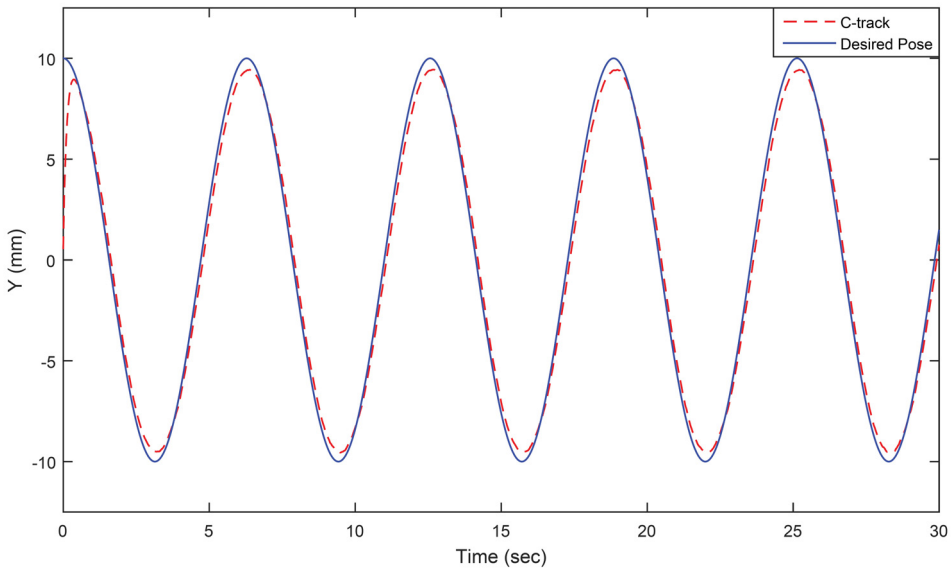

Figure 5.16: Cosinusoidal response for pose of the EE along Y direction

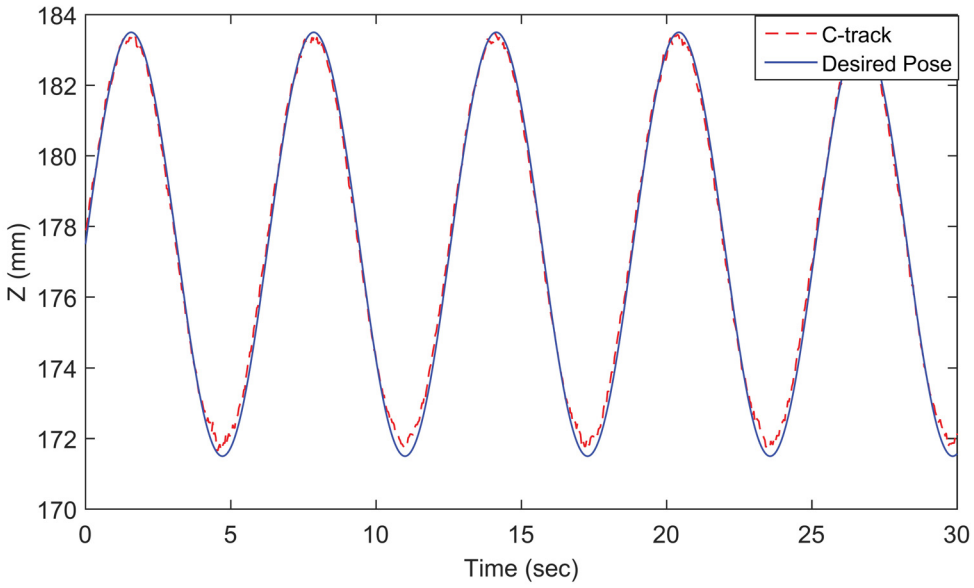

Figure 5.17: Sinusoidal response for pose of the EE along Z direction

Figs.5.18-5.20 show the errors in X, Y and Z directions are shown. These errors are shown in Table.5.5 as well.

Table 5.5: Inverse kinematic validation

Maximum Error in X axis (mm)	0.6
Maximum Error in Y axis (mm)	0.6
Maximum Error in Z axis (mm)	0.4

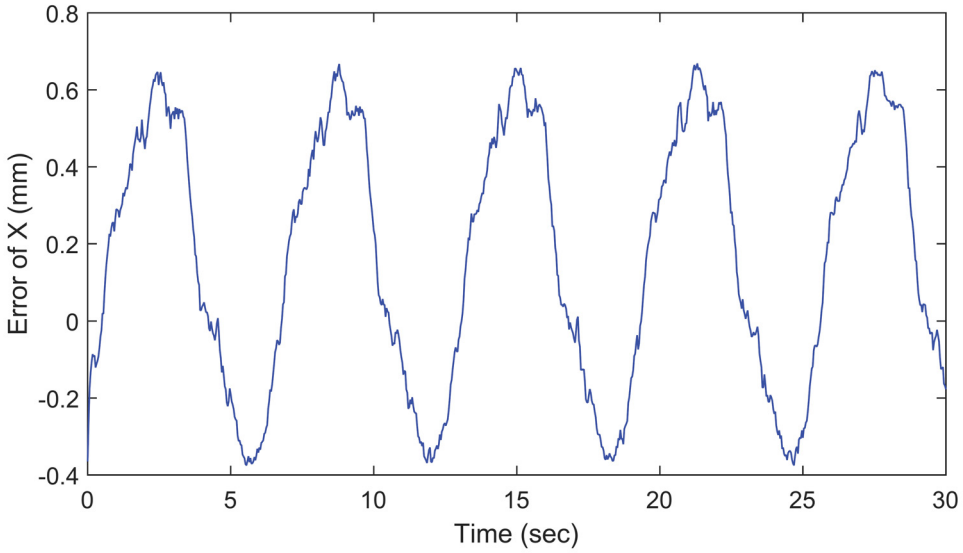

Figure 5.18: Error X

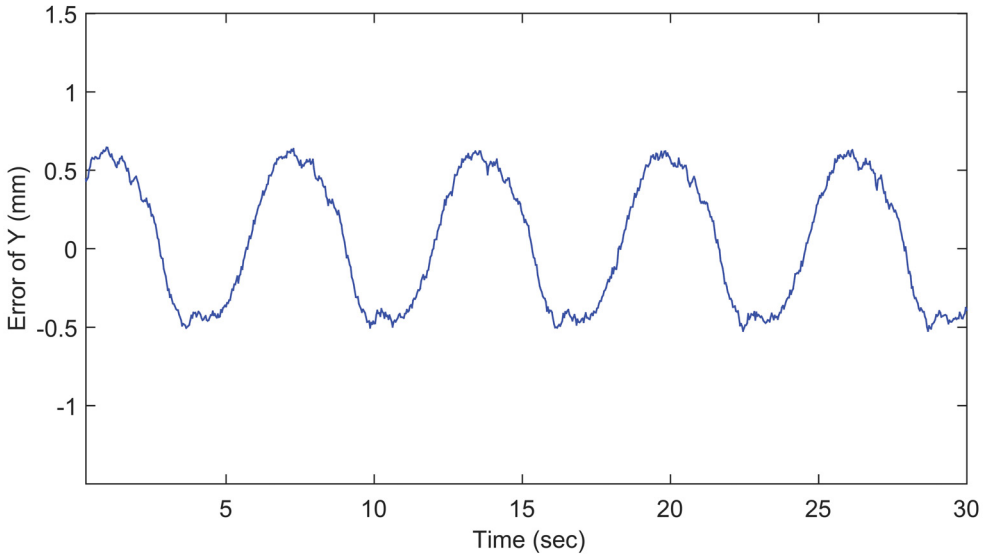

Figure 5.19: Error Y

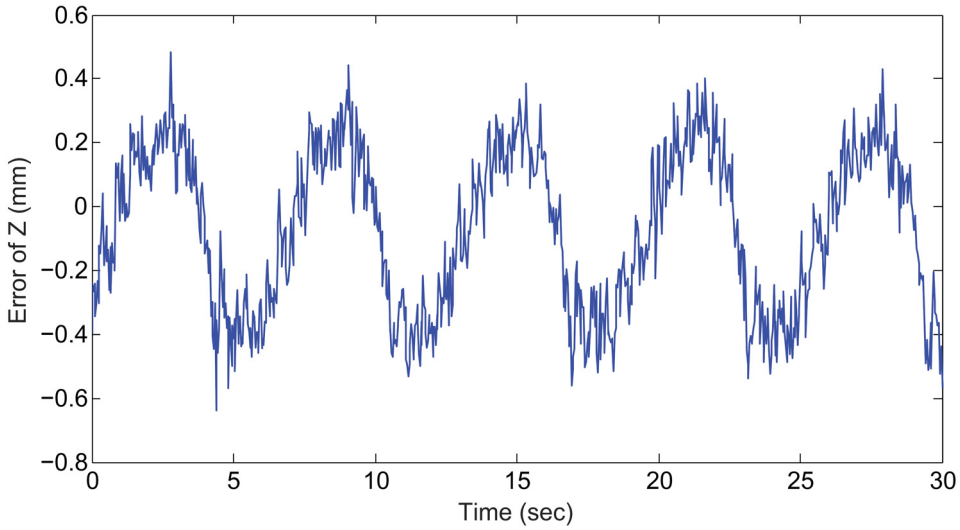

Figure 5.20: Error Z

As you can see, the error in x-direction is changing with respect to time with a sine curvature. The maximum error is about 0.6 mm. The error in y-direction follows a cosine curvature with respect to time. The maximum error in y direction is about 0.6 mm while this error in z axis reaches to 0.4mm. Although, the error of direction seems less than the others ones, the graph shows too much noise caused by C-track. In overall, although there are still errors in all directions, the results are satisfactory in practice.

5.2 Transferring Data

This section is devoted to solving communication problem between two computers. In order to control the pose of EE in real time, the desired pose and the real data must be available at the same time in one Simulink file so that the signals can be compared with each other for controlling the robot. As we discussed in previous section, the parallel robot is connected to PC1 and gets its movement instructions from it. In the same time, PC2 receives the movement data from C-track. So we need to transfer C-track data from PC2 to PC1. The precise and fast way for this communication is using serial port (Fig.5.21).

Figure 5.21: Using serial port for communication

To read the data via C-track, a VB application is written which stores EE pose in six variables and these variables are updated every 35 miliseconds. The code that specifies parallel robots movement pattern is written in $MATLAB$. PC1 is chosen as the master computer. As it was discussed this PC sends movement instructions to robot. To control the robot, it needs the other information that exists in PC2. So we added a code to the original C-Track code to send the data to PC1. The protocol that is chosen for data transfer between two computers is serial protocol.

In the first attempt, a $MATLAB$ code was written to receive the information which PC2 was sending through serial port. The mentioned $MATLAB$ code provided the desired information in the workspace of $MATLAB$. Although the written code could show the data in workspace, Simulink libraries did not support specific elements that were used in that code. So, it is not possible to use this $MATLAB$ file in Simulink in form of a $MATLAB$ function block. The solution that we came up with was to use COM1 Module which makes the connection between two computers possible after it is configured.

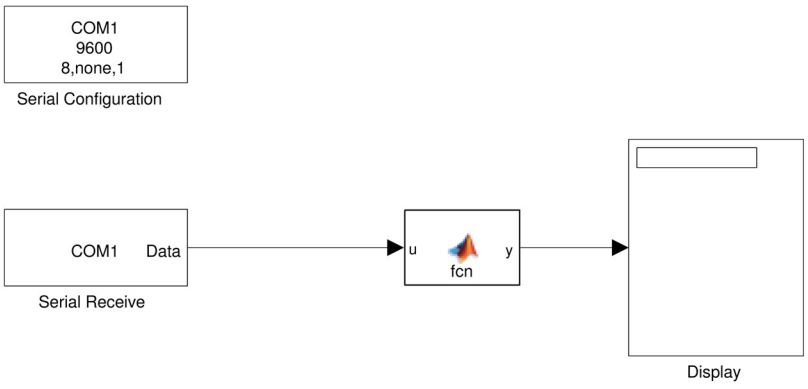

Figure 5.22: COM1 block

Fig.5.22 shows the COM1 Block in Simulink which receives the data from serial port in $MATLAB$ Simulink and the $MATLAB$ function which is responsible for de-serializing data. In serial protocol data is sent as ASCII numbers, hence COM1 receives stream of ASCII numbers. Each ASCII number represents a character as Fig.5.23. By using the Matlab function module code, the data received from COM1 is transformed from ASCII numbers to real numbers.

ASCII TABLE

Decimal	Hex	Char	Decimal	Hex	Char	Decimal	Hex	Char	Decimal	Hex	Char
0	0	[NULL]	32	20	[SPACE]	64	40	@	96	60	`
1	1	[START OF HEADING]	33	21	!	65	41	A	97	61	a
2	2	[START OF TEXT]	34	22	"	66	42	B	98	62	b
3	3	[END OF TEXT]	35	23	#	67	43	C	99	63	c
4	4	[END OF TRANSMISSION]	36	24	$	68	44	D	100	64	d
5	5	[ENQUIRY]	37	25	%	69	45	E	101	65	e
6	6	[ACKNOWLEDGE]	38	26	&	70	46	F	102	66	f
7	7	[BELL]	39	27	'	71	47	G	103	67	g
8	8	[BACKSPACE]	40	28	(	72	48	H	104	68	h
9	9	[HORIZONTAL TAB]	41	29	)	73	49	I	105	69	i
10	A	[LINE FEED]	42	2A	*	74	4A	J	106	6A	j
11	B	[VERTICAL TAB]	43	2B	+	75	4B	K	107	6B	k
12	C	[FORM FEED]	44	2C	,	76	4C	L	108	6C	l
13	D	[CARRIAGE RETURN]	45	2D	-	77	4D	M	109	6D	m
14	E	[SHIFT OUT]	46	2E	.	78	4E	N	110	6E	n
15	F	[SHIFT IN]	47	2F	/	79	4F	O	111	6F	o
16	10	[DATA LINK ESCAPE]	48	30	0	80	50	P	112	70	p
17	11	[DEVICE CONTROL 1]	49	31	1	81	51	Q	113	71	q
18	12	[DEVICE CONTROL 2]	50	32	2	82	52	R	114	72	r
19	13	[DEVICE CONTROL 3]	51	33	3	83	53	S	115	73	s
20	14	[DEVICE CONTROL 4]	52	34	4	84	54	T	116	74	t
21	15	[NEGATIVE ACKNOWLEDGE]	53	35	5	85	55	U	117	75	u
22	16	[SYNCHRONOUS IDLE]	54	36	6	86	56	V	118	76	v
23	17	[ENG OF TRANS. BLOCK]	55	37	7	87	57	W	119	77	w
24	18	[CANCEL]	56	38	8	88	58	X	120	78	x
25	19	[END OF MEDIUM]	57	39	9	89	59	Y	121	79	y
26	1A	[SUBSTITUTE]	58	3A	:	90	5A	Z	122	7A	z
27	1B	[ESCAPE]	59	3B	;	91	5B	[	123	7B	{
28	1C	[FILE SEPARATOR]	60	3C	<	92	5C	\	124	7C	|
29	1D	[GROUP SEPARATOR]	61	3D	=	93	5D	]	125	7D	}
30	1E	[RECORD SEPARATOR]	62	3E	>	94	5E	^	126	7E	~
31	1F	[UNIT SEPARATOR]	63	3F	?	95	5F	_	127	7F	[DEL]

Figure 5.23: Stream Client Receiver block

5.2.1 Problem Definition

Using COM1, received data from serial port is sent to $MATLAB$ Simulink. This Simulink only works in Normal mode because of presence of COM1 module(Fig.5.24)

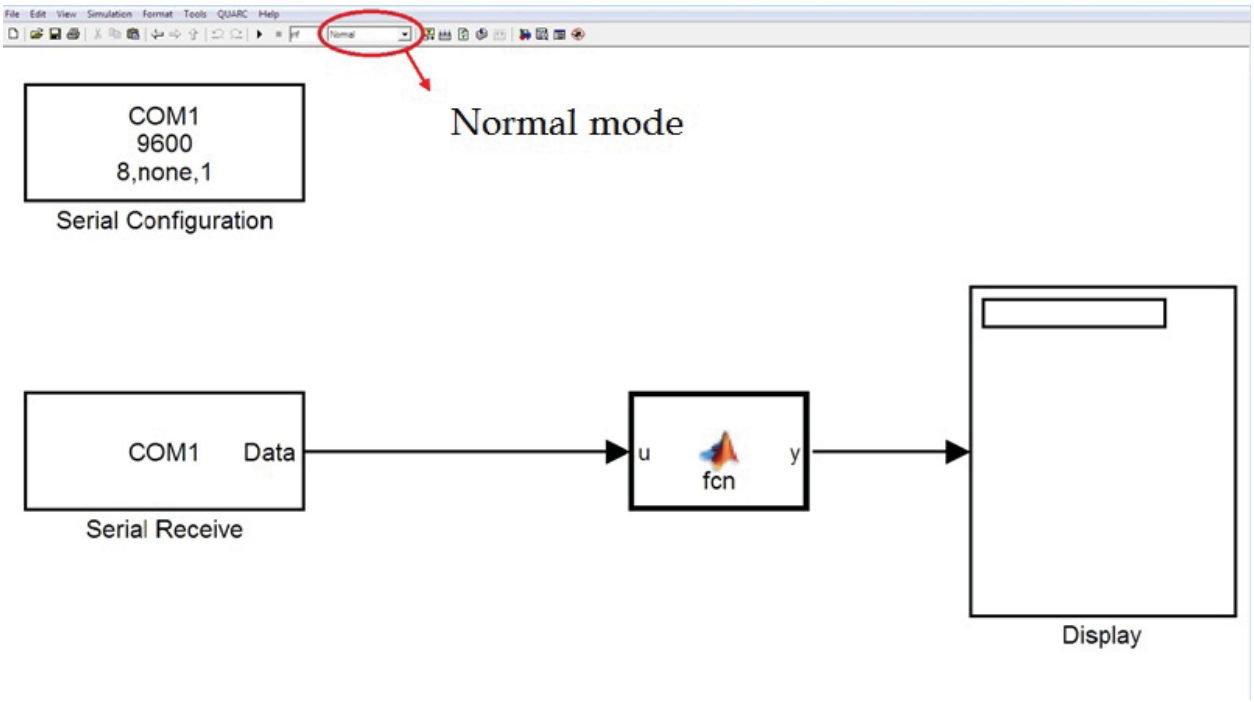

Figure 5.24: Normal mode

As it was explained before, two Quanser cards modules are used to make a connection between the robot and Simulink application. This Simulink only works in External mode (Fig.5.25).

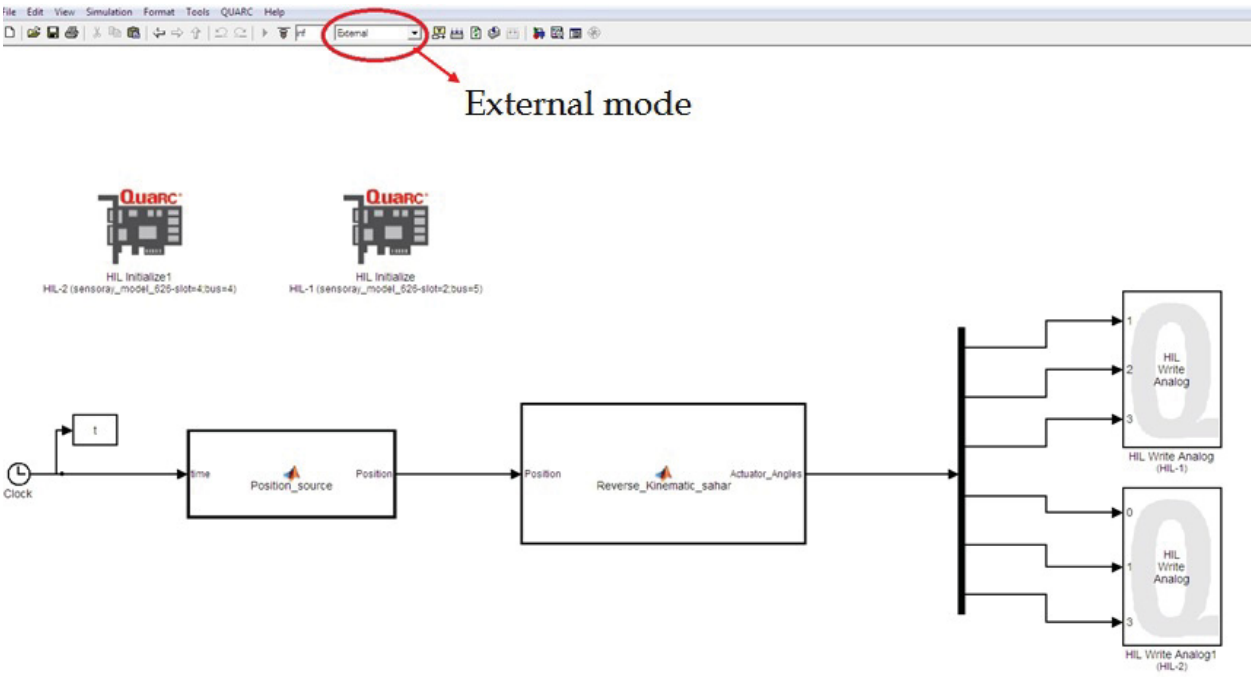

Figure 5.25: External mode

In order to control the parallel robot we need to have desired pose and C-track pose in one Simulink block diagram. It is not possible to run one $MATLAB$ Simulink block diagram in two different modes (Normal and External) at the same time.

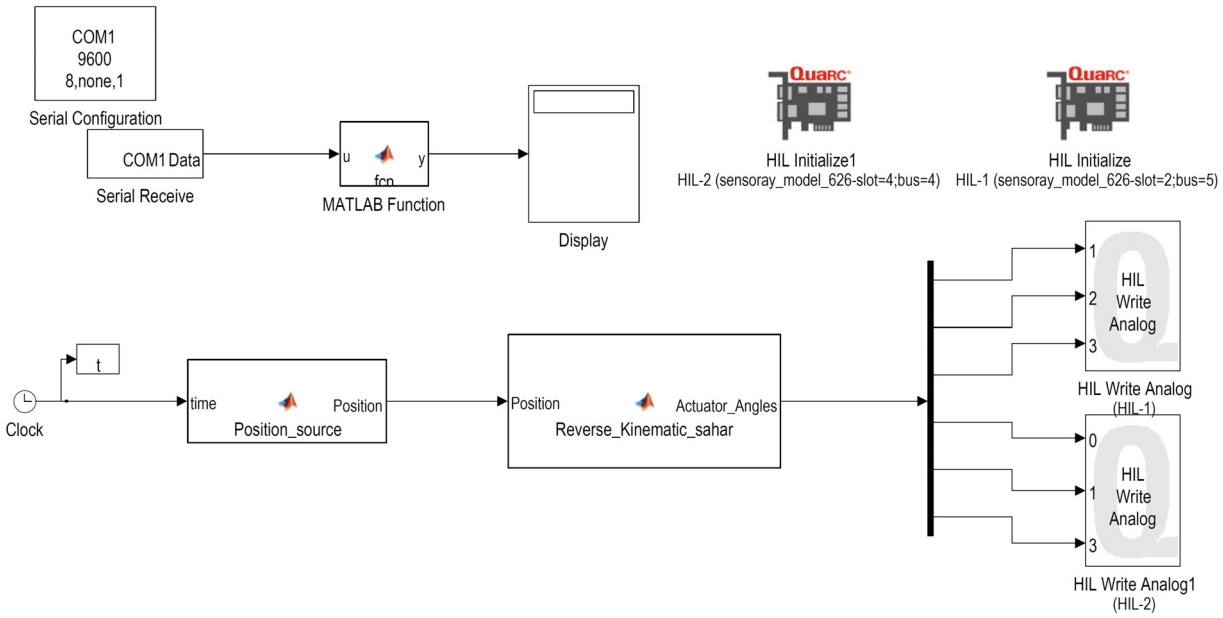

Figure 5.26: Normal and external modes

Fig.5.26 shows the Simulink block diagram which is proposed in order to see the C-track data and desired pose simultaneously. We must solve the problem which is to operate the robot while the serial port is only working in Normal mode.

5.2.2 Solution

Stream Client and Stream Server are the modules which work in both normal and external. Their purpose is to send and receive data by using specified protocol. To solve the problem two following steps were taken:

1. Opening two Matlab files simultaneously: Two Matlab Simulink block diagrams in two different Matlab compilers are opened. One of them works in normal mode (Simulink1) which receives the data from serial port. The other one works in External mode (Simulink2) which is connected to parallel robot.

2. Using Stream Client and Stream Blocks: In order to send the data from Normal mode to External mode, Stream Client blocks are used. While Simulink1 is running, the data can be sent through Stream Server to Simulink2 which receives the data by using Stream Client block.

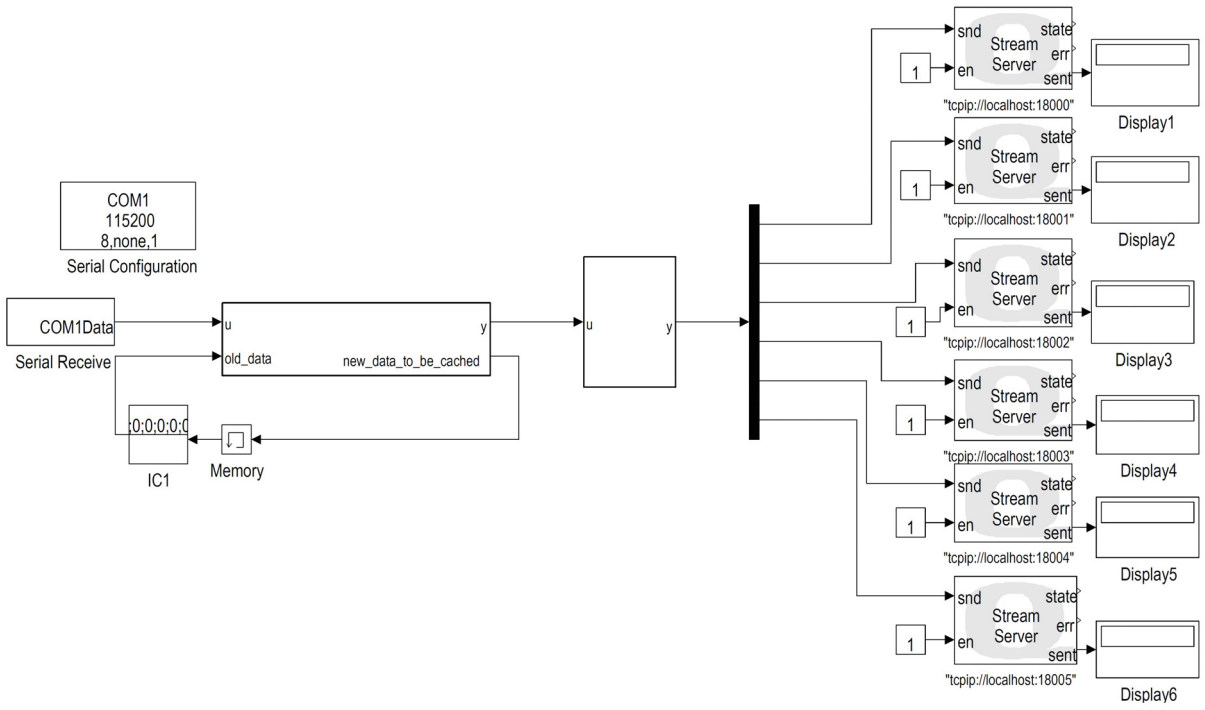

Figure 5.27: Stream Client Sender block

In Fig.5.27, COM1 receives the data from PC2 continuously. Since the serial port transfers all data together, a $MATLAB$ function is written to separate the pose data from each other. Also, COM1 receives all data as ASCII numbers. So, a code is written in which the groups of ASCII numbers are transformed into real numbers. In these codes, the serial receiver module receives 77 ASCII characters in each transaction. Each parameter (x, y, z, α, β and γ) is made of ten characters. After each set of ten characters, there is one newline character which means that a new parameter is started. The remaining 11 characters are ten zeros and one new line which specifies the start of each set of received data. After finding ten zeros and the newline character parameters x, y, z, α, β and γ are retrieved.

Fig.5.28 shows Simulink2 which receives all data from Simulink1. As a result, both C-track data and desired pose are available in one Simulink application and the feedback controller can be built to reduce the error between desired pose and C-track pose in real time.

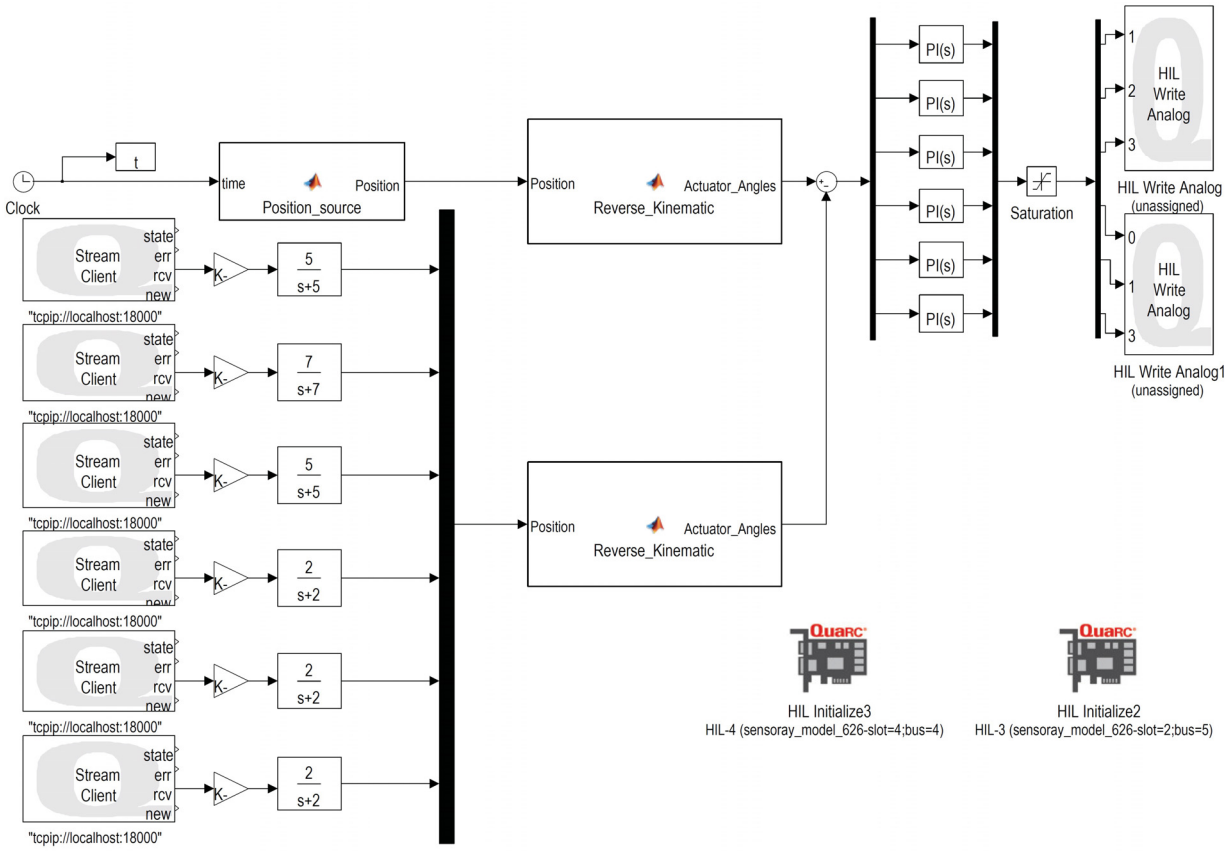

Figure 5.28: Stream Client Receiver block

5.3 Control the Pose of EE

In order to control the pose of end-effector, in the previous section, all the data which were obtained by C-track are transferred from PC2 to PC1. Then, two Matlab files were opened and two Simulink files were running simultaneously. Using the stream client block, all data were transferred from one Simulink file that worked in normal mode to another Simulink file that worked in external mode. In this section, the data transferred is used to control the pose of EE. As it is shown in Fig.5.29, a Simulink block diagram is built in which the desired pose is input to the inverse kinematic block to generate the desired angles for the actuators. Six Stream Client blocks give the pose of EE. Then actuators' angles are compared with real actuators' angles from experiment and six errors are given to PI controllers. PI controllers minimized the error. By using trial and error, different k_I terms and k_P terms are obtained for six PI controllers. Unfortunately, PID controller could not

be used for the system. Because each time k_d was added to the controller, the feedback system became unstable in experiment and it might ruin the actuators. Also, six different low pass filters are used to reduce the noise of system.

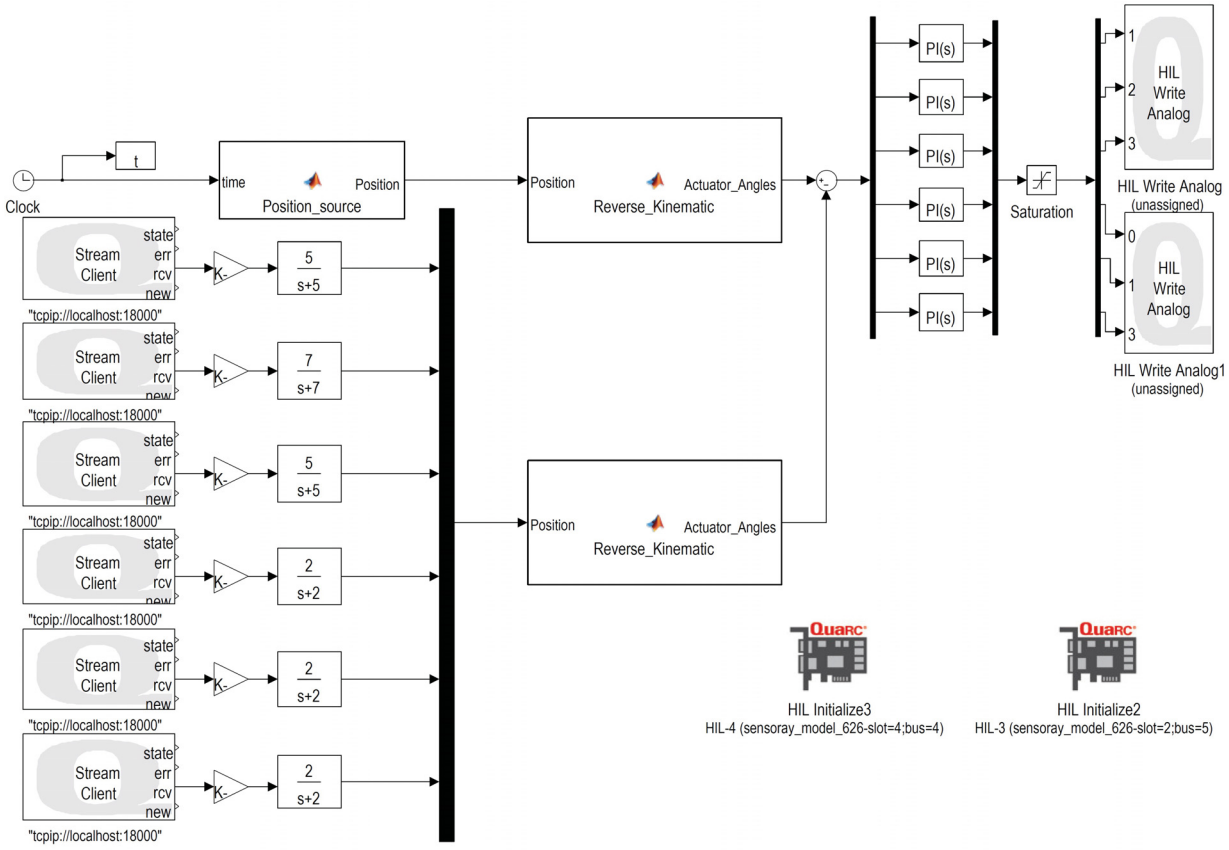

Figure 5.29: PID controller

In order to evaluate the performance of controller, a different desired trajectory is defined as follows:

$$x = 10sin(t) \tag{5.1}$$

$$y = 10cos(t) \tag{5.2}$$

$$z = 10sin(t) + 198.5 \tag{5.3}$$

$$\alpha = 0.0175sin(t) \tag{5.4}$$

$$\beta = 0.0175sin(t) \tag{5.5}$$

$$\gamma = 0.0175sin(t) \tag{5.6}$$

where, t is time (sec), x, y, z are the position of EE (mm) and α, β and γ are rotations about x, y, z axises (rad), respectively.

Fig.5.30-5.35 show the behavior of system without using any controller and low pass filter.

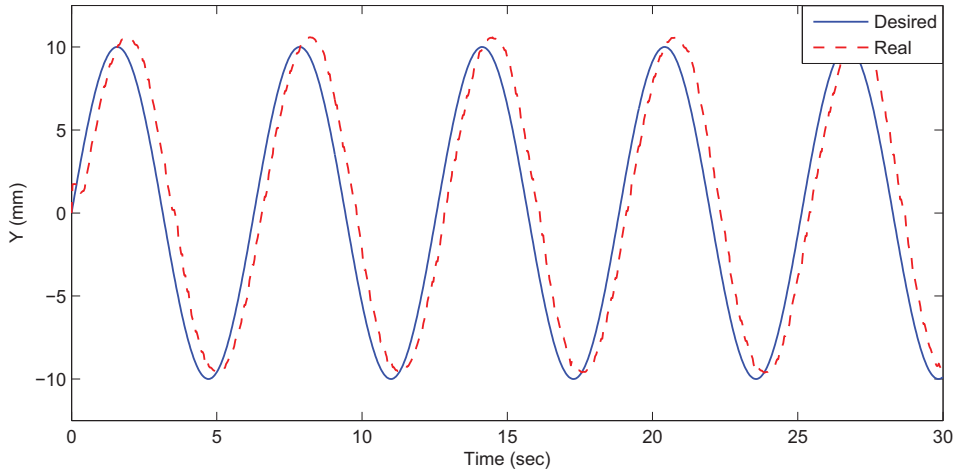

Figure 5.30: Sinusoidal response for pose of EE about X direction without controller

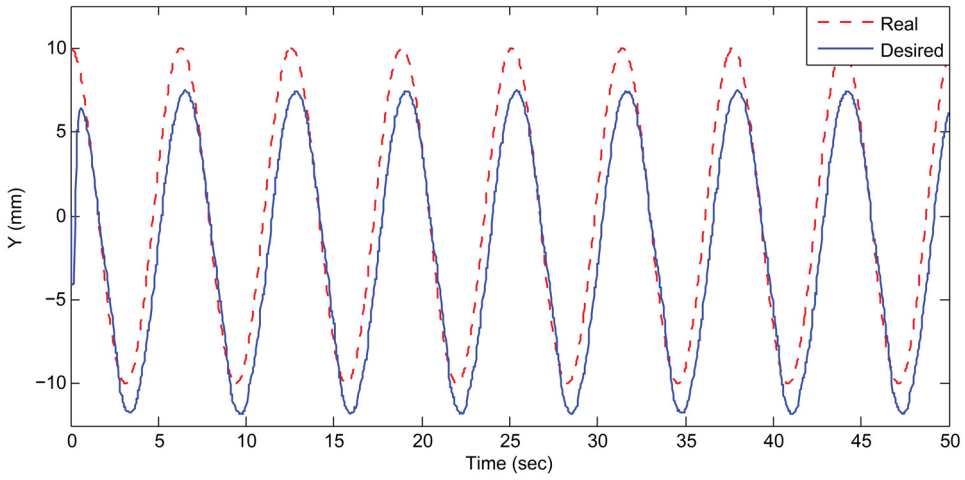

Figure 5.31: Cosinusoidal response for pose of EE along Y direction without controller

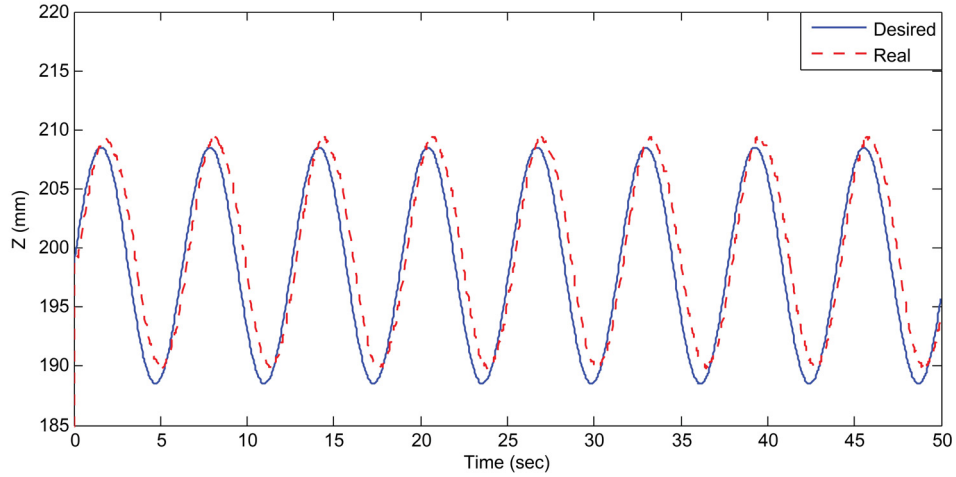

Figure 5.32: Sinusoidal response for pose of EE along Z direction without controller

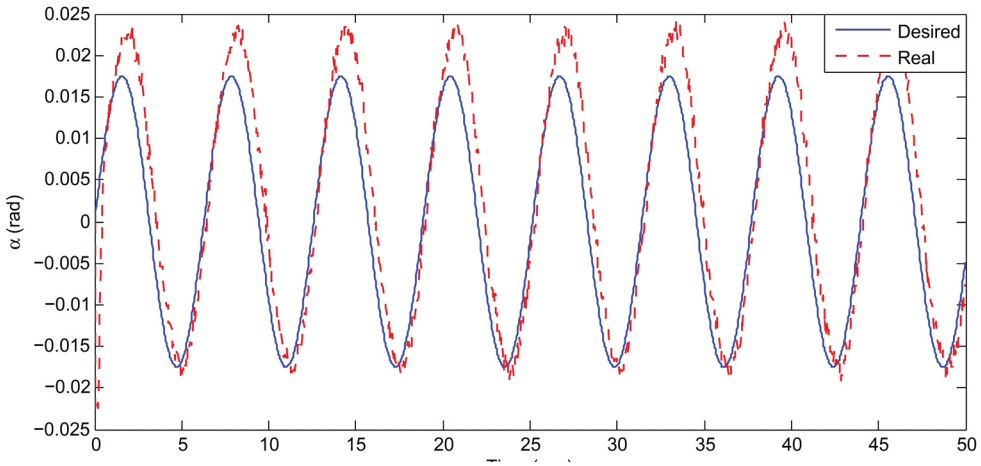

Figure 5.33: Sinusoidal response for pose of EE about X direction (α) without controller

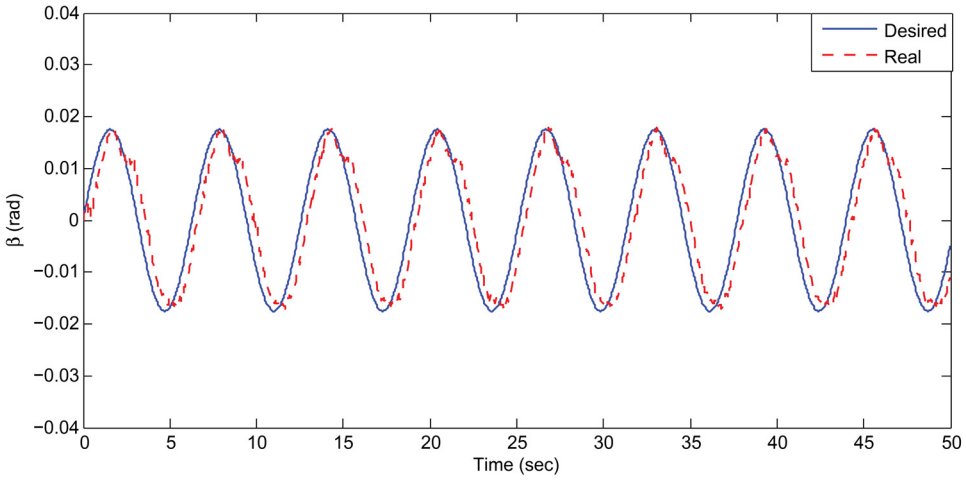

Figure 5.34: Sinusoidal response for pose of EE about Y direction (β) without controller

Table 5.6: PI tuned by trial and error

Actuators' NO.	K_p	K_i
One	0.8	3.75
Two	0.9	3.75
Three	1	3.75
Four	0.9	3.8
Five	1.1	3.9
Six	1	3.75

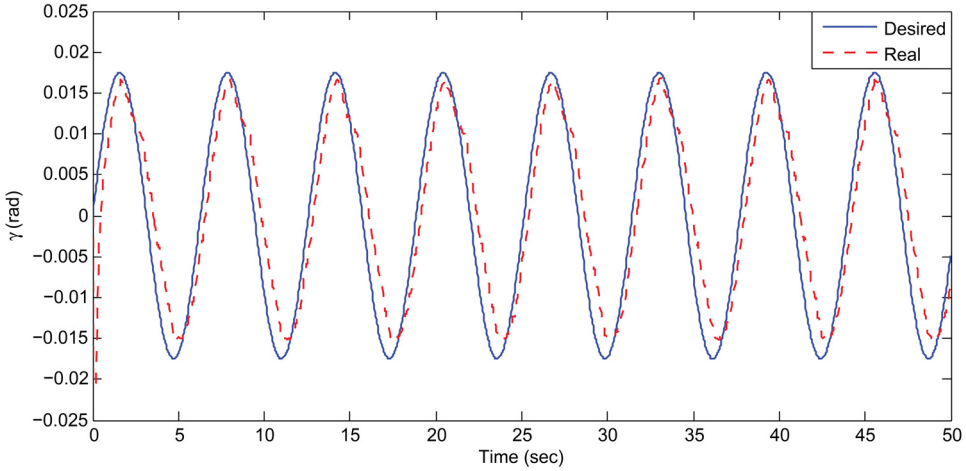

Figure 5.35: Sinusoidal response for pose of EE about Z direction (γ) without controller

As it is shown, the steady state error in x and z directions are 0.6 and 1.3 mm, respectively. However, this error in y is almost 2.5 mm which means that a feedback controller is necessary. Also, there is a 0.9 second time delay. To reduce this error and time delay, six PI controllers tuned by trial and error (Table.5.6) are applied. These controllers decrease the error of EE pose and increase the stability of system. Also in order to decrease the noise, low-pass filter is used and tuned by trial and error.

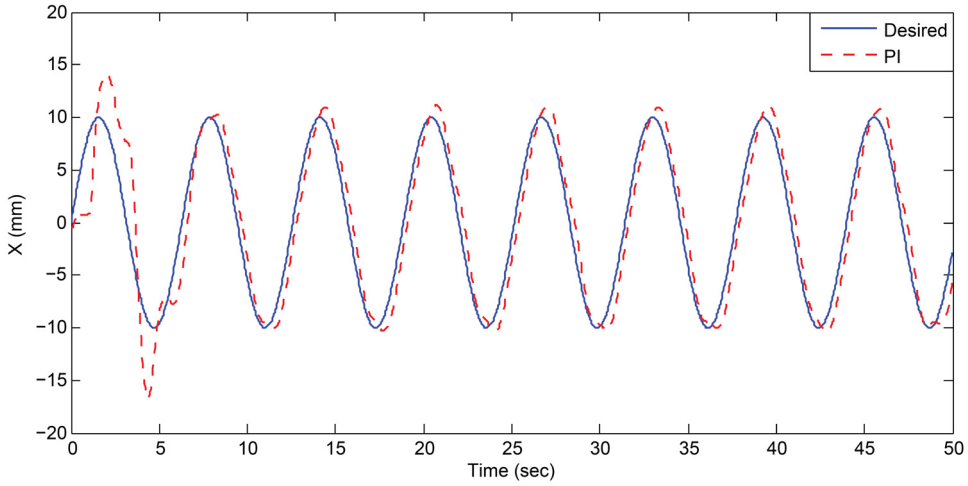

Figure 5.36: Sinusoidal response for pose of EE along X direction, using PI controller

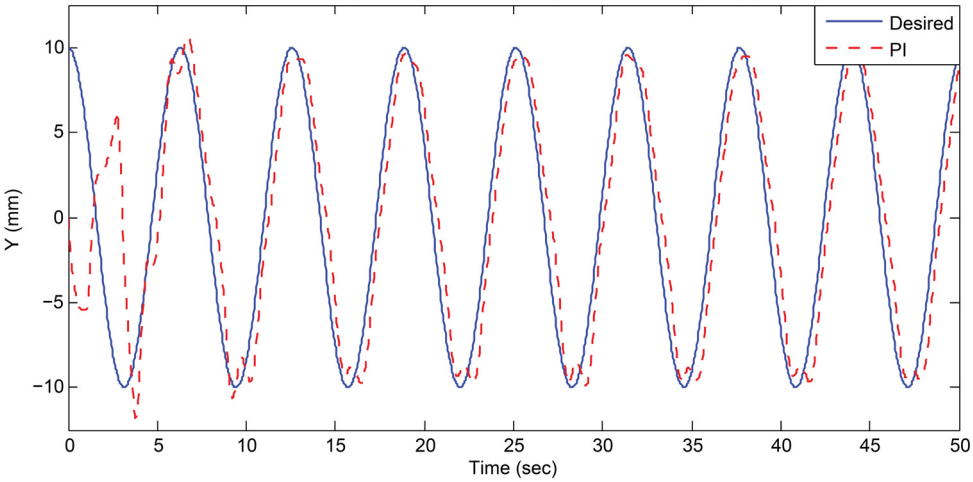

Figure 5.37: Cosinusoidal response for pose of EE along Y direction, using PI controller

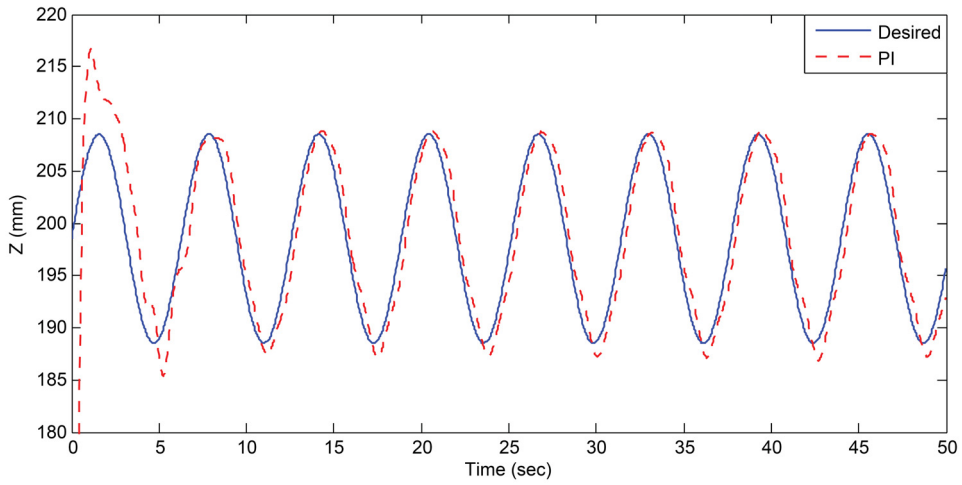

Figure 5.38: Sinusoidal response for pose of EE along Z direction, using PI controller

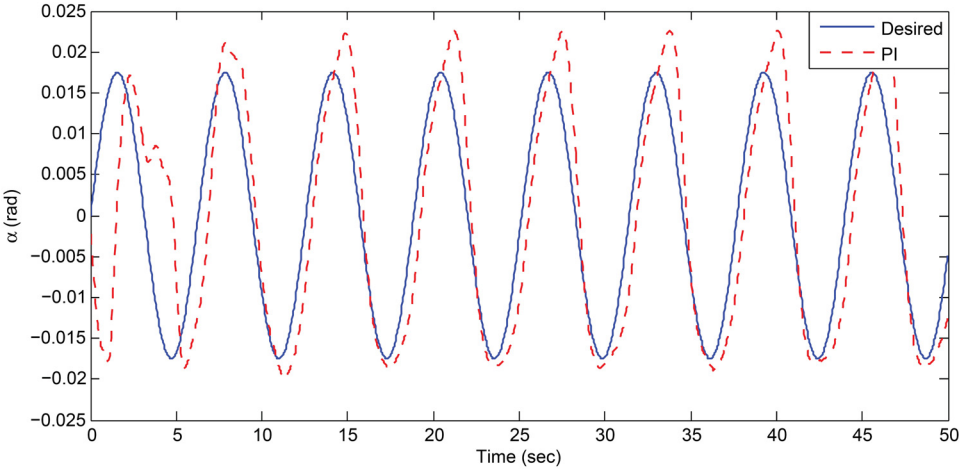

Figure 5.39: Sinusoidal response for pose of EE about X direction (α), using PI controller

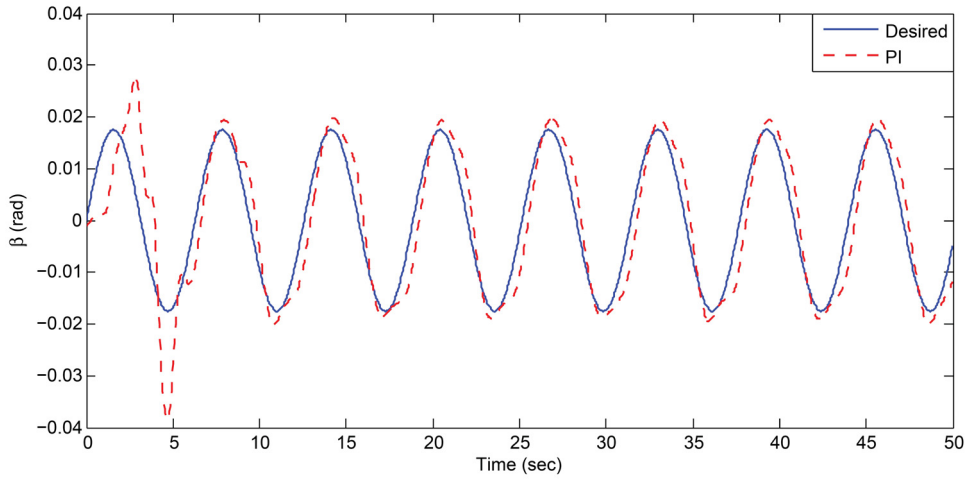

Figure 5.40: Sinusoidal response for pose of EE about Y direction (β), using PI controller

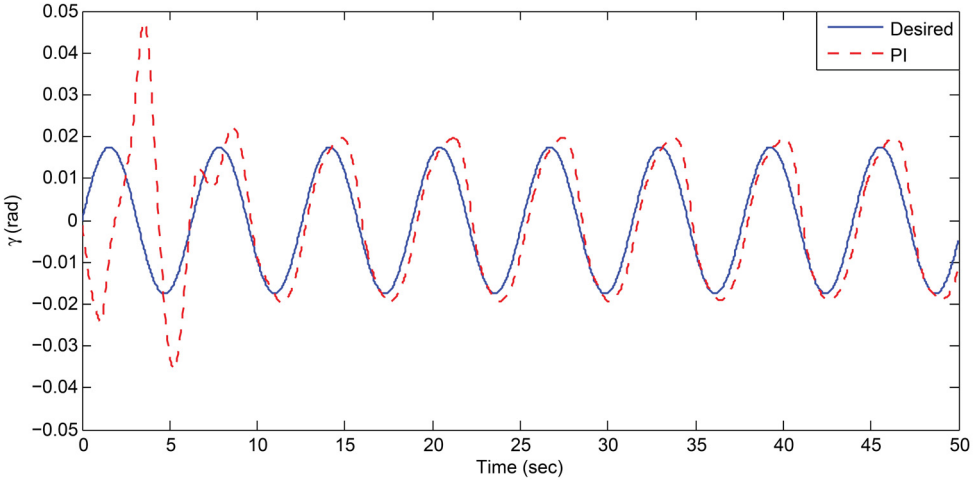

Figure 5.41: Sinusoidal response for pose of EE about Z direction (γ), using PI controller

Figs.5.36-5.41 show the behavior of system in presence of PI controller. As it is shown, tuning six different PI controllers, decreased the average of time delay from 0.9 to almost 0.3 sec. While the error of z does not have a significant change (from 1.3 to 1.1mm), the error in y direction has reduced 10 times, from 2.5 to 0.25 mm. It is not possible to use K_d, because it makes real system unstable. As a result, system has some overshoots in each direction. In Table.5.7, the steady state error of system with a controller is compared with a non-controller system in each direction. Also, Table.5.8 shows the Integral Time-weighted Absolute Error (ITAE) of the system with and without

Table 5.7: Comparing the pose' steady state error with and without PI controllers

	Without controller	With controller
X axis (mm)	0.7	0.75
Y axis (mm)	2.5	0.25
Z axis (mm)	1.3	1.1
α (rad) axis	0.0055	0.004
β axis (rad)	0.0015	0.00145
γ axis (rad)	0.0025	0.002

Table 5.8: Comparing the pose'ITAE with and without PI controllers

	Without controller $(mm.s^2)$	With controller $(mm.s^2)$
X axis (mm)	2669	2055.9
Y axis (mm)	2971.9	2390.7
Z axis (mm)	2824.4	2198.7
α (rad) axis	6.0267	5.2366
β axis (rad)	5.0559	4.5198
γ axis (rad)	5.3485	4.6625

the controller.

Although increasing k_I for each controller add some overshoots at the beginning of each graph, steady state error decreased significantly which means that applied PI controller is robust and has an acceptable pose tracking control.

5.4 Comparing the Simulation and Experimental Results

In order to compare the simulation results of pose control of EE with the experimental ones, we used normalized time instead of real time to calculate the Integral Time-weighted Absolute Error (ITAE) as follow,

$$ITAE = \int \bar{t}|\epsilon|d\bar{t} \tag{5.7}$$

where $\bar{t} = t/T$ is normalized time, T is total time, and ϵ is the error between the desired pose with the calculated pose (mm).

Table.5.9 compares the errors obtained from simulations with the errors from experiments (Table.5.10).

Table 5.9: Normalized ITAE of the EE's pose in simulations

	$X\ (mm)$	$Y\ (mm)$	$Z\ (mm)$
Without controller	0.5030	0.476	0.0436
With controller	0.0453	0.0464	0.0040
With controller, with noise	0.0596	0.0570	0.0407
With controller, with disturbance and noise	0.0599	0.0599	0.0358

Table 5.10: Normalized ITAE of the EE's pose in experiments

	Without controller (mm)	With controller (mm)
X axis (mm)	1.0676	0.8244
Y axis (mm)	1.1888	0.9563
Z axis (mm)	1.1298	0.8795
α (rad) axis	0.0024	0.0021
β axis (rad)	0.0020	0.0018
γ axis (rad)	0.0021	0.0019

As it is shown, the error of pose in simulations is less than that of experiments. There are several reasons that cause to have more error in experimental works, such as:

- There are always some uncertainties which cause some errors between the real parameters and measured ones, such as the length of links.
- Transferring the data between two computers causes time delay.
- We cannot use K_d gain for design the PI controller in experiments, because it caused to system become unstable.
- Like every other sensors, C-track cause the noise.

5.5 Summary

This chapter has described the experimental setup including the C-track, communication between two computers, 6-DOF Robot and controller, and also results for proposed PI controllers. In this chapter C-track is implemented to obtain the pose of EE. While the robot is connected to PC1, the achieved pose by C-track stores in PC2. Data has been transfered from PC2 to PC1 by using serial port. Two Simulink block diagrams are made to receives the data from serial port and move the robot simultaneously. In order to control the pose of EE, 6 different PI controllers is applied and

increase the robustness of the system. The results with and without the presence of controllers are compared and discussed.

Chapter 6

Conclusion

This chapter summarize the main conclusions and contributions of previous chapters. Meanwhile, some future works are presented.

6.1 Contribution and Research Conclusion

In order to obtain more dexterity to produce complex composite structures, a 6-RSS parallel robot is added to current Automated Fiber Placement (AFP) machines. The present research study is devoted to modeling and control of 6 RSS parallel platform. The main contributions and conclusions of this research work is listed as follows:

- The inverse and forward kinematics of 6-RSS parallel robot are analyzed.
- The dynamic models (linear and nonlinear) for parallel's actuators have been built. The parameters of linear dynamic models have been identified using Genetic Algorithm (GA). Also, the multi-objective optimization using GA was applied to find the parameters of the nonlinear DC actuators' dynamic model of the 6-RSS parallel robot in the lab.
- A PID controller is designed and optimized using GA to control the EEs pose of the 6-RSS parallel robot. The simulation results indicated that the optimized PID controller has a satisfactory pose tracking performance.
- A C-track was applied to obtain the precise values for position and orientation of EE.

- Then, inverse kinamtic model has been validated in experiment. Comparing the desired pose with the obtained pose by C-track proved that the inverse kinematic model is accurate enough.

- In the experimental work, two different PCs are used. One of them stored the obtained pose by C-track. The other one, moved the parallel robot. By transferring the data from First PC to second one and running two Simulink models at the same time, we are able to control the pose of EE and made it possible to have the feedback from pose of the system.

- Finally, six different PI controllers have been implemented to the robot to determine the control input for the six actuators. Using these control inputs, the pose of EE has been controlled. Experimental results showed the satisfactory pose tracking control performance.

6.2 Future Works

The future works of this thesis include the following:

- The model based controllers such as feedback linearizion will be implemented in the experimental setup which includes the pose measurement using C-track.

- The designed PI controllers will be fine tuned by using multi-objective optimization technique to deliver better tracking performance.

- The real-time pose controller will be integrated with the Fanuc robot to realize the cooperative fiber placement operation.

Bibliography

[1] Dan Zhang. *Parallel robotic machine tools*. Springer Science & Business Media, 2009.

[2] Doug Stewart. A platform with six degrees of freedom. *Proceedings of the institution of mechanical engineers*, 180(1):371–386, 1965.

[3] Shuang Cong, Guodong Li, and Xianyong Feng. Parameters identification of nonlinear dc motor model using compound evolution algorithms. In *Proceedings of the World Congress on Engineering*, volume 1, 2010.

[4] Feng Gao, Weimin Li, Xianchao Zhao, Zhenlin Jin, and Hui Zhao. New kinematic structures for 2-, 3-, 4-, and 5-dof parallel manipulator designs. *Mechanism and machine theory*, 37(11):1395–1411, 2002.

[5] Serdar Kucuk and Zafer Bingul. *Robot kinematics: forward and inverse kinematics*. INTECH Open Access Publisher, 2006.

[6] X Shi and RG Fenton. Solution to the forward instantaneous kinematics for a general 6-dof stewart platform. *Mechanism and machine theory*, 27(3):251–259, 1992.

[7] Meng-Shiun Tsai, Ting-Nung Shiau, Yi-Jeng Tsai, and Tsann-Huei Chang. Direct kinematic analysis of a 3-prs parallel mechanism. *Mechanism and Machine Theory*, 38(1):71–83, 2003.

[8] Xiguang Huang, Qizheng Liao, Shimin Wei, Xu Qiang, and Shuguang Huang. Forward kinematics of the 6-6 stewart platform with planar base and platform using algebraic elimination. In *Automation and Logistics, 2007 IEEE International Conference on*, pages 2655–2659. IEEE, 2007.

[9] Zheng Geng and L Haynes. Neural network solution for the forward kinematics problem of a stewart platform. In *Robotics and Automation, 1991. Proceedings., 1991 IEEE International Conference on*, pages 2650–2655. IEEE, 1991.

[10] Kevin Cleary and Thurston Brooks. Kinematic analysis of a novel 6-dof parallel manipulator. In *Robotics and Automation, 1993. Proceedings., 1993 IEEE International Conference on*, pages 708–713. IEEE, 1993.

[11] Kai Liu, John M Fitzgerald, and Frank L Lewis. Kinematic analysis of a stewart platform manipulator. *Industrial Electronics, IEEE Transactions on*, 40(2):282–293, 1993.

[12] PR McAree and RW Daniel. A fast, robust solution to the stewart platform forward kinematics. *Journal of robotic systems*, 13(7):407–427, 1996.

[13] Yunfeng Wang. An incremental method for forward kinematics of parallel manipulators. In *Robotics, Automation and Mechatronics, 2006 IEEE Conference on*, pages 1–5. IEEE, 2006.

[14] Choon seng Yee and Kah-bin Lim. Forward kinematics solution of stewart platform using neural networks. *Neurocomputing*, 16(4):333–349, 1997.

[15] Zongliang Mu and Kazem Kazerounian. A real parameter continuation method for complete solution of forward position analysis of the general stewart. *Journal of Mechanical Design*, 124(2):236–244, 2002.

[16] Pratik J Parikh and Sarah S Lam. Solving the forward kinematics problem in parallel manipulators using an iterative artificial neural network strategy. *The International Journal of Advanced Manufacturing Technology*, 40(5-6):595–606, 2009.

[17] Antonio Morell, Mahmoud Tarokh, and Leopoldo Acosta. Solving the forward kinematics problem in parallel robots using support vector regression. *Engineering Applications of Artificial Intelligence*, 26(7):1698–1706, 2013.

[18] CM Liaw, RY Shue, HC Chen, and SC Chen. Development of a linear brushless dc motor drive with robust position control. In *Electric Power Applications, IEE Proceedings-*, volume 148, pages 111–118. IET, 2001.

[19] Rolf Isermann and Marco Münchhof. Application examples. *Identification of Dynamic Systems*, pages 605–682, 2011.

[20] Tolgay Kara and Ilyas Eker. Nonlinear modeling and identification of a dc motor for bidirectional operation with real time experiments. *Energy Conversion and Management*, 45(7):1087–1106, 2004.

[21] Radojka Krneta, Sanja Antić, and Danilo Stojanović. Recursive least squares method in parameters identification of dc motors models. *Facta universitatis-series: Electronics and Energetics*, 18(3):467–478, 2005.

[22] Mehdi Nasri, Hossein Nezamabadi-Pour, and Malihe Maghfoori. A pso-based optimum design of pid controller for a linear brushless dc motor. *World Academy of Science, Engineering and Technology*, 26(40):211–215, 2007.

[23] G Mamani, J Becedas, V Feliu-Batlle, and H Sira-Ramirez. Open-loop algebraic identification method for a dc motor. In *Control Conference (ECC), 2007 European*, pages 3430–3436. IEEE, 2007.

[24] Jinzhu Peng and Rickey Dubay. Identification and adaptive neural network control of a dc motor system with dead-zone characteristics. *ISA transactions*, 50(4):588–598, 2011.

[25] Bharat Bhushan and Madhusudan Singh. Adaptive control of dc motor using bacterial foraging algorithm. *Applied Soft Computing*, 11(8):4913–4920, 2011.

[26] Wei Wu. Dc motor parameter identification using speed step responses. *Modelling and Simulation in Engineering*, 2012:30, 2012.

[27] Amro M Farid and S Masoud Barakati. Dc motor neuro-fuzzy controller using pso identification. In *Electrical Engineering (ICEE), 2014 22nd Iranian Conference on*, pages 1162–1167. IEEE, 2014.

[28] Chin-I Huang, Chih-Fu Chang, Ming-Yi Yu, and Li-Chen Fu. Sliding-mode tracking control of the stewart platform. In *Control Conference, 2004. 5th Asian*, volume 1, pages 562–569. IEEE, 2004.

[29] Chin-I Huang and Li-Chen Fu. Smooth sliding mode tracking control of the stewart platform. In *Control Applications, 2005. CCA 2005. Proceedings of 2005 IEEE Conference on*, pages 43–48. IEEE, 2005.

[30] Dong Sun, R Lu, James K Mills, and C Wang. Synchronous tracking control of parallel manipulators using cross-coupling approach. *The International Journal of Robotics Research*, 25(11):1137–1147, 2006.

[31] Xiaocong Zhu, Guoliang Tao, Bin Yao, and Jian Cao. Adaptive robust posture control of parallel manipulator driven by pneumatic muscles with redundancy. *Mechatronics, IEEE/ASME Transactions on*, 13(4):441–450, 2008.

[32] Dongya Zhao, Shaoyuan Li, and Feng Gao. Fully adaptive feedforward feedback synchronized tracking control for stewart platform systems. *International Journal of Control, Automation, and Systems*, 6(5):689–701, 2008.

[33] Yang Bo, Pei Zhongcai, and Tang Zhiyong. Fuzzy pid control of stewart platform. In *Fluid Power and Mechatronics (FPM), 2011 International Conference on*, pages 763–768. IEEE, 2011.

[34] Xue Jian, Tang Zhiyong, and Pei Zhongcai. Study on stewart platform control method based on model reference adaptive control. In *Cyber Technology in Automation, Control, and Intelligent Systems (CYBER), 2011 IEEE International Conference on*, pages 17–20. IEEE, 2011.

[35] S Srikanth and G Ramesh Chandra. Modeling and pid control of the brushless dc motor with the help of genetic algorithm. In *Advances in Engineering, Science and Management (ICAESM), 2012 International Conference on*, pages 639–644. IEEE, 2012.

[36] Sahar Alinia, Masoud Hemmatian, Wen Fang Xie, and Rui Zeng. Posture control of 3-dof parallel manipulator using feedback linearization and model reference adaptive control. In *Electrical and Computer Engineering (CCECE), 2015 IEEE 28th Canadian Conference on*, pages 1145–1150. IEEE, 2015.

[37] Lorenzo Sciavicco and Bruno Siciliano. *Modelling and control of robot manipulators*. Springer Science & Business Media, 2012.

[38] W.L.G.Pollard JR. Spray painting machine, August 27 1940. US Patent 2,213,108.

[39] Pollard Willard LV. Position-controlling apparatus, June 16 1942. US Patent 2,286,571.

[40] Oscar Reinoso, Rafael Aracil, and Roque Saltarén. *Using Parallel Platforms as Climbing Robots*. INTECH Open Access Publisher, 2006.

[41] Bashar S El-Khasawneh and Placid M Ferreira. Computation of stiffness and stiffness bounds for parallel link manipulators. *International Journal of Machine Tools and Manufacture*, 39(2):321–342, 1999.

[42] Vincent Nabat, Rodriguez de la O, O María, Olivier Company, Sébastien Krut, and François Pierrot. Par4: very high speed parallel robot for pick-and-place. In *Intelligent Robots and Systems, 2005.(IROS 2005). 2005 IEEE/RSJ International Conference on*, pages 553–558. IEEE, 2005.

[43] Jürgen Hesselbach, Jan Wrege, Annika Raatz, and Oliver Becker. Aspects on design of high precision parallel robots. *Assembly Automation*, 24(1):49–57, 2004.

[44] Tzung-Cheng Tsai and Yeh-Liang Hsu. Development of a parallel surgical robot with automatic bone drilling carriage for stereotactic neurosurgery. *Biomedical Engineering: Applications, Basis and Communications*, 19(04):269–277, 2007.

[45] Zhenhua Wang, Liguo Chen, and Lining Sun. An integrated parallel micromanipulator with flexure hinges for optical fiber alignment. In *Mechatronics and Automation, 2007. ICMA 2007. International Conference on*, pages 2530–2534. IEEE, 2007.

[46] Rui Zeng, Shuling Dai, Wenfang Xie, and Bhat Rama. Constraint conditions determination for singularity-free workspace of central symmetric parallel robots. *IFAC-PapersOnLine*, 48(3):1930–1935, 2015.

[47] Gwo-Ruey Yu and Rey-Chue Hwang. Optimal pid speed control of brush less dc motors using lqr approach. In *Systems, Man and Cybernetics, 2004 IEEE International Conference on*, volume 1, pages 473–478. IEEE, 2004.

[48] Sidney A Davis. Brushless dc motor, January 18 1977. US Patent 4,004,202.

[49] Thomas J Sokira and Wolfgang Jaffe. *Brushless dc motors: electronics commutation and controls*. Tab Books, 1990.

[50] Atef Saleh Othman Al-Mashakbeh. Proportional integral and derivative control of brushless dc motor. *European Journal of Scientific Research*, 35(2):198–203, 2009.

[51] Thomas M Jahns. Motion control with permanent-magnet ac machines. *Proceedings of the IEEE*, 82(8):1241–1252, 1994.

[52] Gui-Jia Su and John W McKeever. Low-cost sensorless control of brushless dc motors with improved speed range. *Power Electronics, IEEE Transactions on*, 19(2):296–302, 2004.

[53] Siri Weerasooriya and MA El-Sharkawi. Identification and control of a dc motor using back-propagation neural networks. *Energy Conversion, IEEE Transactions on*, 6(4):663–669, 1991.

[54] S Singer and J Appelbaum. Starting characteristics of direct current motors powered by solar cells. *Energy Conversion, IEEE Transactions on*, 8(1):47–53, 1993.

[55] NA Rahim, MN Taib, and MI Yusof. Nonlinear system identification for a dc motor using narmax approach. In *Sensors, 2003. AsiaSense 2003. Asian Conference on*, pages 305–311. IEEE, 2003.

[56] Amir Hajiloo and Wen-Fang Xie. Multi-objective optimal fuzzy fractional-order pid controller design. *Journal ref: Journal of Advanced Computational Intelligence and Intelligent Informatics*, 18(3):262–270, 2014.

[57] SN Sivanandam, Sai Sumathi, SN Deepa, et al. *Introduction to fuzzy logic using MATLAB*, volume 1. Springer, 2007.

[58] Melanie Mitchell. *An introduction to genetic algorithms*. MIT press, 1998.

[59] Zhixin Yang, Wui Ian Hoi, and Jianhua Zhong. Gearbox fault diagnosis based on artificial neural network and genetic algorithms. In *System Science and Engineering (ICSSE), 2011 International Conference on*, pages 37–42. IEEE, 2011.

[60] Darrell Whitley. A genetic algorithm tutorial. *Statistics and computing*, 4(2):65–85, 1994.

[61] Dymytro Skybyk. Polyphase brushless dc and ac synchronous machines, August 2 1994. US Patent 5,334,898.

[62] Shi-Zhong He, Shaohua Tan, Feng-Lan Xu, and Pei-Zhuang Wang. Fuzzy self-tuning of pid controllers. *Fuzzy sets and systems*, 56(1):37–46, 1993.

[63] Allan B Plunkett. Field orientation control of a permanent magnet motor, March 21 1989. US Patent 4,814,677.

[64] Kouhei Ohnishi, Masaaki Shibata, and Toshiyuki Murakami. Motion control for advanced mechatronics. *Mechatronics, IEEE/ASME Transactions on*, 1(1):56–67, 1996.